TÉCNICO LISBOA

Nanostructures for Solar Energy Harvesting

Mariana Sofia Santos

Thesis to obtain the Master of Science Degree in

Electrical and Computer Engineering

Supervisors: Prof. João Filipe Pereira Fernandes
Prof. João Paulo Neto Torres

Examination Committee

Chairperson: Prof. Célia Maria Santos Cardoso de Jesus
Supervisor: Prof. João Filipe Pereira Fernandes
Member of the Committee: Prof. Carlos Alberto Ferreira Fernandes

November 2022

To my mom who has always supported me.

I declare that this document is an original work of my own authorship and that it fulfills all the requirements of the Code of Conduct and Good Practices of the Universidade de Lisboa.

Declaro que o presente documento é um trabalho original da minha autoria e que cumpre todos os requisitos do Código de Conduta e Boas Práticas da Universidade de Lisboa.

Acknowledgments

Firstly, I would like to thank the professors that made this work possible, professor João Torres and professor João Fernandes, for the trust they placed in me. A very special thanks to Ricardo Lameirinhas, who took it upon himself to answer all of my restless questions, and rid me of self-doubt in my work. More than a mentor, a friend.

To my ride-or-die in IST, Catarina, which at first glance may be an unlikely friend, but has turned out to be a friend for life. Thank you for the support, and all the hour-long calls to talk about nothing and everything.

Thank you to my boyfriend for providing a safe space for me to blossom and be me, and making me laugh when all I wanted to do was cry.

I have to express my undying gratitude to my mom, all my family, and Susana, for being my rock, supporting me, and believing in me when I did not. Especially to my grandparents, aunts, and uncles.

Lastly, I would like to thank all the friends I have met through this five-year-long journey, especially ”Trio Marabilha” and ”Grupo Alegre e Unido”, you sure have made it an easier ride.

Abstract

Renewable energy sources are more and more essential to energy production as the society evolves towards a fossil fuel free world. Solar energy is one of the most abundant sources of green energy. Nanoantennas can be used to improve and enhance the absorption of light into a PV cell in order to generate more current. In this study different nanoantennas structures are analyzed in tandem with a Silicon solar cell, as an effort to improve its output. The nanoantennas studied are metallic aperture nanoantennas made up of either Silver, Aluminium, Gold or Copper. The three geometries compared were rectangular, circular and triangular. The maximum field enhancement obtained was for an Aluminium rectangular nanoantenna of 50 nm thickness. Despite this, the geometry with more improvements compared with a Silicon basic cell was the circle geometry with a 100 nm radius.

Keywords

Electric Field Concentration; Nanoantennas; Optoelectronic devices; Photovoltaic Technology; Solar Energy Harvesting; Surface Plasmon Polaritons

Resumo

As fontes de energia renováveis são cada vez mais cruciais para a produção de energia à medida que a sociedade evolui para um mundo livre de combustíveis fósseis. A energia solar é uma das mais abundantes fontes de energia verde. As nanoantenas podem ser utilizadas para melhorar e aumentar a absorção da luz para uma célula fotovoltaica, de modo a gerar maior corrente. Neste estudo, diferentes estruturas de nanoantenas são analisadas em conjunto com uma célula solar de Silício, como um esforço para melhorar a sua geração. As nanoantenas estudadas são nanoantenas de abertura metálica compostas por Prata, Alumínio, Ouro ou Cobre. As três geometrias comparadas foram rectangulares, circulares e triangulares. O melhoramento máximo obtido foi para uma nanoantena rectangular de Alumínio de 50 nm de espessura. Apesar disto, a geometria com mais melhorias em comparação com uma célula básica de Silício foi a geometria circular com um raio de 100 nm.

Palavras Chave

Concentração do Campo Elétrico; Nano-antenas; Dispositivos Optoeletrónicos; Tecnologia Fotovoltaica; Captação de Energia Solar; Plasmões polaritões superficiais

Contents

List of Figures

List of Tables

Acronyms

EM	Electromagnetic
EOT	Extraordinary Optical Transmission
GenI	First Generation
GenII	Second Generation
GenIII	Third Generation
KVL	Kirchhoff's Voltage Law
NP	Nanoparticle
NREL	National Renewable Energy Laboratory
1M5P	One diode five parameters model
PV	Photovoltaic
RF	Radio Frequency
SPP	Surface Plasmon Polariton
SPS	Surface Plasmons
SQ	Shockley-Queisser
STC	Standard Test Conditions

Nomenclature

α	Absorption coefficient
ω	Angular frequency
$\bar{\varepsilon}$	Complex dielectric function
$\bar{E}$	Complex electric field vector
$\bar{H}$	Complex magnetic field vector
$\int E$	Electric field line integral
k	Extinction factor (optical properties) or Wavevector norm (propagation)
$\mathfrak{Im}(\varepsilon)$	Imaginary part of the complex dielectric function
ω_p	Plasma angular frequency
$\mathfrak{Re}(\varepsilon)$	Real part of the complex dielectric function
$\hbar$	Reduced Planck's constant
n	Refractive index
c_0	Velocity of light in the vacuum
λ	Wavelength
$\bar{\boldsymbol{k}}$	Wavevector

1

Introduction

Contents

1.1 Motivation

According to the United Nations, the global population is estimated to reach 9.7 billion by 2050. With the growth of society comes the inherent increase of energy demand. The current production of energy relies heavily on fossil fuels which have an undesirable environmental impact. This aligned with the energy crisis, in which the prices of fossil fuels keep rising, for example, in September 2021 the price of natural gas was as high as 6.5 times the price of 2019.

Alternatively, photovoltaic cells convert solar power into DC electric power at a somewhat low price, and in a more environmental friendly way. In addition, PV cells require very little maintenance and are robust devices, which makes them attractive in the global energy market. In particular, the solar energy global market was valued at $52.5 billion in 2018 and is projected to reach $223.3 billion by 2026.

The solar radiation that reaches the earth in one day is enough to mitigate the earth's total energy needs for a year. However, in PV cells the efficiency is limited by the bandgap of the material. Each photon with energy above the bandgap produces an electron-hole pair independently of its energy. Photons that have an energy matched to the bandgap will produce the same energy delivered from high energy photons. This limits the efficiency to approximately 30% for single junction cells, and around 55% for multi-junction cells.

The idea of using nanoantennas as an alternative to solar cells was first proposed by Bailey in 1972. The use of nanoantennas in photovoltaics has gained a significant amount of interest in the last few years, considering they are expected to be more efficient and inexpensive. In addition, solar nano-rectennas are not only expected to exceed PV devices efficiency during the day, but also by their ability to function during the night, making them less susceptible to weather conditions.

In more recent studies there has been an effort to combine the conventional PV with nanoantennas. This has been done either by laying the nanoantenna on top of the PV cell or in between layers of the PV cell, as an effort to increase light trapping.

1.2 Objectives

The main aim of this work is to characterize the influence of different nanostructures for light trapping in energy-harvesting devices, increasing electrical conversion and cells' efficiency. This will be done by analysing different nanostructures for solar energy harvesting: aperture nanoantennas, bowtie nanoantennas, seebeck structures, among others. In addition, analysis of the parameters influence on optical spectra and I-V curves. Lastly, comparing the different nanostructures with other commercialized/tradicional solar cells. After the literature review, a numerical simulation using Finite Element Tool *COMSOL Multiphysics* will be conducted. The goal is to study parameters to optimize solar cells to reach electric field enhancement and light trapping for different incident radiation spectra.

1.3 Outline

This document is divided into five chapters. Chapter 1 is introductory, where the motivation, objectives, and overall structure of this document are provided. Chapter 2 is an overview of the photovoltaic cells' evolution through time, as well as the fundamental principles of operation, and models for solar cells. Thereafter, nanoantennas are introduced, and a literature review on the topic is conducted, focusing on the different types of nanoantennas. The aperture nanoantennas are discussed, consequently leading to a need to introduce diffraction theories and light-matter interaction models. In Chapter 3, the developed simulation model in *COMSOL Multiphysics* is described in detail. The results from conducted simulations are then presented and discussed in Chapter 4. Finally, in Chapter 5 the conclusions are drawn and some reflection on the future work is done.

2

State-of-the-Art

Contents

2.1 Traditional PV

The conventional PV technologies generate power through the photovoltaic effect. The photovoltaic effect is the conversion of incident light into electricity by a p-n or p-i-n semiconductor device. Photons with energy greater than the semiconductor's bandgap are absorbed, exciting the electrons from the valence band to the conduction band, creating an equal number of holes in the valence band. If the electrons-hole pairs are created within the depletion zone of the p-n junction or within a minority carrier diffusion length from the boundary of each depletion zone, the existing electric field in the depletion region separates the pairs and drives them through an external load [1].

2.1.1 Evolution of Technology

The diversity of photovoltaic materials used and studied is large and still growing, as illustrated by Figure 2.1, which shows the National Renewable Energy Laboratory (NREL) records since 1976.

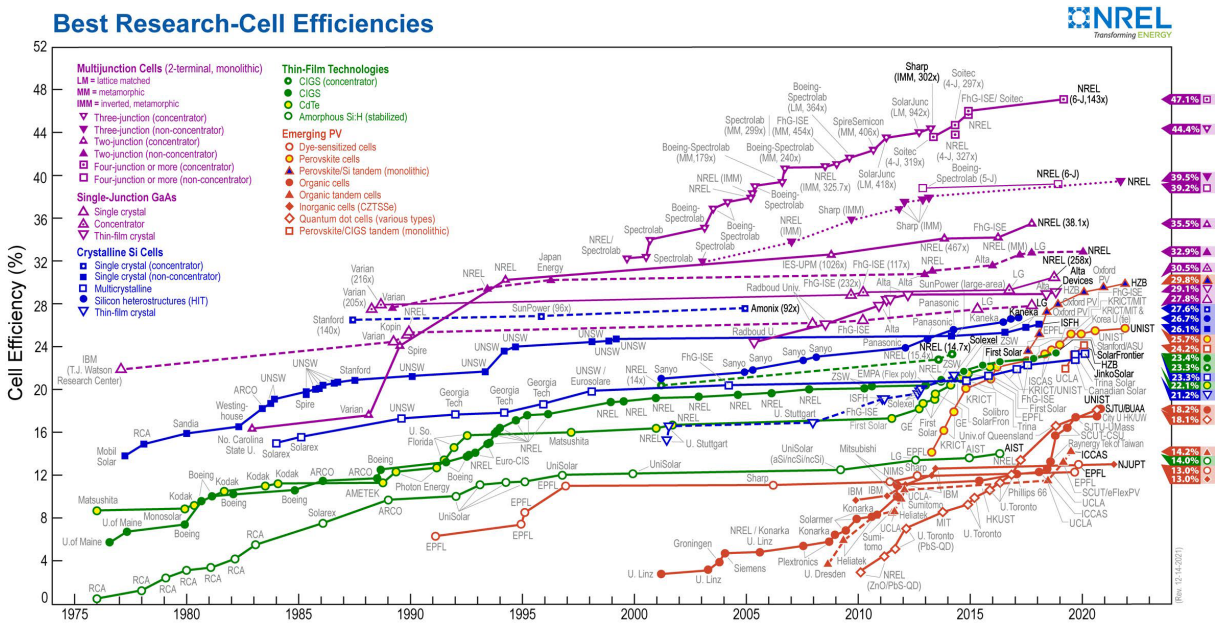

Figure 2.1: Best research-cell efficiency Chart.
(Adapted from: [2])

The First Generation (GenI) refers to wafer-based devices like mono-crystalline and poly-crystalline silicon and germanium p-n junctions, which make up the majority of the sales volume [1,3,4]. The doping impurities used in those solar cells are boron, phosphorus and a few other [4]. Additionally, as shown in Table 2.1 they exhibit efficiencies from 13% to 20%, they are quite efficient due to high carrier mobility and broad absorption. However, expensive manufacturing is the main drawback of GenI solar cells [4].

The Second Generation (GenII) emerged in an attempt to reduce the cost of solar cells. GenII

are conventional thin films devices that are made up of materials such as cadmium telluride (CdTe), copper-indium/gallium-diselenide/sulphide (CIGS), amorphous silicon (aSi), and microcrystalline silicon (μSi). This generation features relatively low efficiencies, 10 % for CdTe, 12% for CIGS, and 7% for a-Si (Table 2.1). Both GenI and GenII do not exceed the Shockley-Queisser (SQ) limit for single bandgap devices [3, 4].

The Third Generation (GenIII) solar cells are not made of conventional p-n junctions or thin films. It encompasses multi-layered solar cells consisting of gallium arsenide and amorphous silicon. This type of solar cells have a potential efficiency above the SQ limit [3]. It includes nanocrystal solar cells such as Quantum Dots.

Table 2.1: Comparison of different types of photovoltaic cells.
(Adapted from [5])

Sub-types	Mono-crystalline	Poly-crystalline	CdTe	CIGS	a-Si	Multi-junction
	Purity 99.99999%	Purity 99.99999%	low temperature sensitivity	captures large spectrum	Amourphous Silicon	GaAs/CIS a-Si/mc-Si
Description	Crystalline silicon wafers		Semiconductor deposited directly on glass			
Module Efficiency	High		Low			
Performance under heat	Performance degrades with higher temperatures		Up to 60% lower heat coefficient than crystalline silicon modules, great for hot climates			
Space per kWp	$>$ 8 m^2	9 m^2 - 30 m^2	20m^2			
Efficiency (production)	15-20 %	13-15%	10%	12%	7%	36%
Efficiency (Lab)	25%	21%	16%	20%	10%	40%

In recent research, the prospect of applying nanotechnology to a solar cell has been studied in attempts to increase the efficiency of the solar cell. The Figure 2.2 developed in [6] illustrates one possibility of nanoantenna incorporation in a solar cell.

Figure 2.2: Incorporation of a nanoantenna in a a-Si solar cell.
(Adapted from: [6])

2.1.2 P-N Junction

The p-n junction involves the contact between two semiconductor regions, one p-type and one n-type. Far from the contact between the n-type and p-type semiconductors, the electron density n_0, and the hole density p_0 are approximately the same as the donor impurity density N_d and the acceptor impurity density N_a, respectively. In the vicinity of the contact region, in the transition between the n region to the p region, the electron density varies in several orders of magnitude, i.e, an electron density gradient. A diffusion current is associated with the density gradient that is responsible for the flow of electrons from the n region to the p region, and the flow of holes from the p to n region. This movement of charge destroys the local electric neutrality and gives rise to an electric field that is responsible for the conduction current of electrons and holes in the opposite direction to the respective diffusion current. In thermodynamic equilibrium and for each type of carrier, the diffusion current density is balanced by the respective conduction current density so as to have a total current density of zero. The electric field is directed from region n to region p, and is at its maximum in the plane of contact between the two regions, and is zero outside the transition region. The existence of the electric field allows us to define a contact potential difference, V_{C0}, between the n-type and p-type neutral regions [7].

For the p-n junction in solar cells the incident light gives rise to an excess of carriers, relatively to the thermodynamic equilibrium values. The generated electron-hole pairs, under the influence of local fields, are separated and can accumulate in regions where there will no longer be electrical neutrality, resulting in a potential difference, positive from p to n [8].

2.1.3 Solar Cell Model and Parameters

Most PV panels datasheets provide information on certain specifications of the solar cell, such as the open-circuit voltage V_{oc}, the short circuit current I_{sc}, the maximum power point P_{MP} and respective V_{MP} and I_{MP} at Standard Test Conditions (STC). The STC consist of an irradiance G of 1000 W/m^2 and cell temperature of 25℃. Several models try to reproduce the I-V characteristic of PV cells in working conditions. Our focus is on the One diode five parameters model (1M5P). The PV cells characteristic I-V and P-V curves are shown in Figure 2.3.

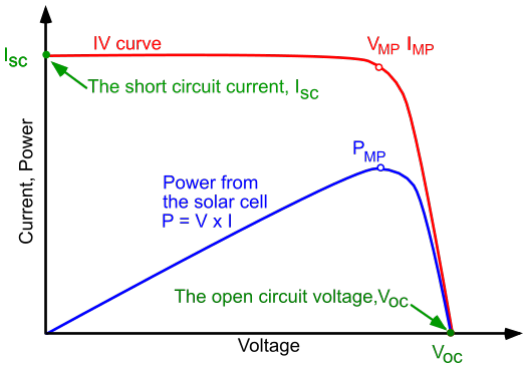

Figure 2.3: I-V characteristic curve (red); P-V characteristic curve (blue).
(Adapted from: [9])

Figure 2.4 shows the equivalent circuit for the 1M5P. The circuit consists of a photo-generated controlled current source I_{PH}, a diode, describing the p-n junction behavior of the solar cell, a shunt resistance R_{sh}, representing the current leakage losses, and a series resistance R_s, illustrating the ohmic losses [10, 11].

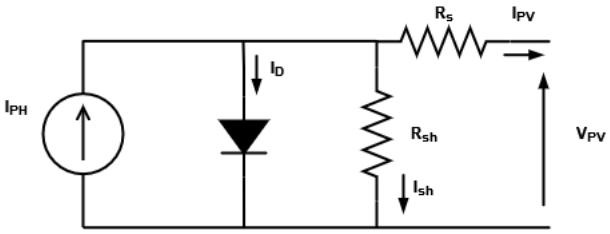

Figure 2.4: Equivalent circuit representing the five-parameter model of the solar cell.
(Adapted from: [10])

The Kirchhoff's Voltage Law (KVL) allows the direct deduction of the characteristic equation 2.1.

$$I_{PV} = I_{ph} - I_D - I_{sh} \tag{2.1}$$

The diode is described by the single exponential Shockley equation [11]. The Shockley equation 2.2 relates the diode current I_D, and the applied forward bias $V_{PV} + R_S I_{PV}$, in the PV cell case [11, 12].

$$I_D = I_O \left(\exp\left(\frac{V_{PV} + R_S I_{PV}}{a V_T} \right) - 1 \right) \tag{2.2}$$

Where I_O is the dark saturation current, a is the the ideality factor, and V_T the thermal voltage given by equation 2.3.

$$V_T = \frac{N_s k T}{q} \tag{2.3}$$

Where N_s is the number of cells in series, q is the electron charge module, k is the Boltzmann's constant, and T is the absolute temperature in Kelvin ($q = 1.602 \times 10^{-}9$ C; $k \approx 1.381 \times 10^{-23}$ J/K). The shunt current equation 2.4 appears by applying the KVL once more.

$$I_{sh} = \frac{V_{PV} + R_s I_{PV}}{R_{sh}} \tag{2.4}$$

Finally, replacing equations 2.2 and 2.4 in equation 2.1, the relationship between the PV cell output current and terminal voltage according to the 1M5P model is reached in equation 2.5.

$$I_{PV} = I_{PH} - I_O \left(\exp\left(\frac{V_{PV} + R_S I_{PV}}{a V_T} \right) - 1 \right) - \frac{V_{PV} + R_s I_{PV}}{R_{sh}} \tag{2.5}$$

With the previous equations it is possible to the determine the five unknown parameters of a PV panel I_0, I_{ph}, a, R_p and R_s through different estimation methods. The expression for the dark saturation current I_0 can be obtained from short circuit condition: $V_{pv} = 0;\ I_{pv} = I_{sc}$. In a similar way, the expression for I_{ph} can be obtained from the open circuit condition: $V_{pv} = V_{oc};\ I_{pv} = 0$.

According to [12], the 1M5P is validated with both experimental and datasheet values with a difference less than 5%.

Other relevant parameters that can be determined from the I-V and P-V curves of the solar cell are the Fill Factor FF and the efficiency η. The Fill Factor is the ratio between the obtainable power P_{MP} and the product of the open-circuit voltage and short-circuit current defined in equation 2.6.

$$FF = \frac{I_{MP} V_{MP}}{I_{SC} V_{OC}} \tag{2.6}$$

This parameter provides information about the quality of the cell, the typical values for a silicon solar cell are around 0.7 to 0.8. The closer FF is to 1, the more power can the cell supply.

The efficiency is defined by equation 2.7, where A_{cell} is the cell's effective area and G is the irradiance.

$$\eta = \frac{I_{MP} V_{MP}}{A_{cell} G} \tag{2.7}$$

2.1.4 Semiconductors

An appropriate way to evaluate a semiconductor may be by assessing its absorption coefficient since different semiconductor materials possess different absorption coefficients. The higher the absorption coefficient, the easier the semiconductor absorbs photons, resulting in the excitation of conduction band electrons.

Besides, the absorption coefficient expresses how deep light with a specific wavelength can penetrate before it is absorbed. This drives the absorption coefficient to not only depend on the material of choice but also the incident wavelength.

Consulting the online database [13] of the refractive index, n, and extinction coefficient, k, it is possible to obtain the figure 2.5 through equation 2.8 for the absorption coefficient, α, in cm^{-1}. The refractive index, n, determines the propagation speed of the Electromagnetic (EM) in the semiconductor, while the absorption coefficient, α, characterises the EM waves absorption.

$$\alpha = \frac{4\pi k}{\lambda} \tag{2.8}$$

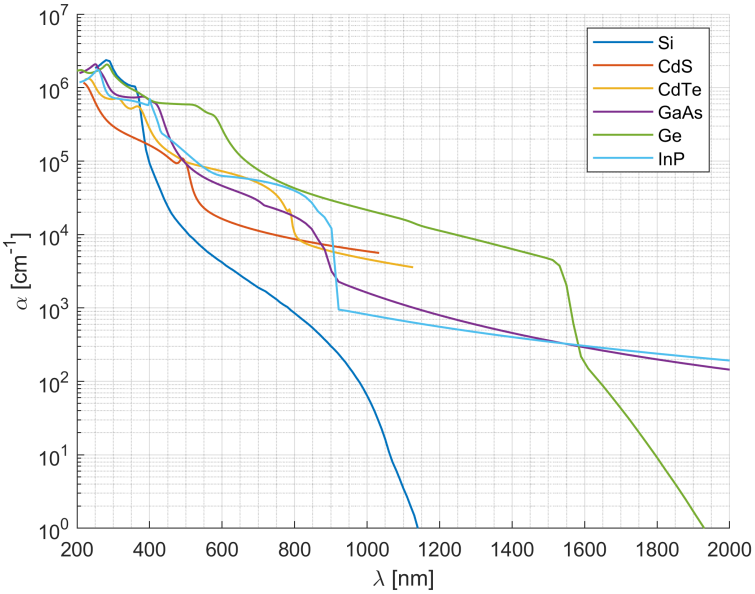

Figure 2.5: Different Semiconductor's Absorption.

In figure 2.5, it is noticeable a sharp, steep decrease in the absorption coefficient, this is due to the fact that light with energy bellow the bandgap does not contain enough energy to excite an electron from the valence band into the conduction band, preventing that light from being absorbed, and any radiation with less energy (greater wavelength).

2.2 Nanoantennas for Solar Energy Harvesting

An optical antenna, also called nanoantenna, can enhance photo-physical phenomenons, for example, photodetection, where a photon gives rise to an electron and a hole, that is the underlying phenomenon responsible for the functioning of Photovoltaic (PV) cells, thus nanoantennas can be used to enhance or improve the absorption of light into a given semiconductor.

Analogous to Radio Frequency (RF) antennas, nanoantennas capture the incident EM wave, either visible or infrared (IR), inducing an alternating current on the antenna surface that oscillates at the same frequency of the incident EM wave. For RF antennas, the resonance condition is achieved when the antenna size is an integer multiple of half wavelength, this is not the case for nanoantennas. At optical frequencies, metals are highly dispersive materials with finite conductivity. The displacement currents flowing along the metal have smaller wavelengths than free-space, due to field penetration in the metal, appearing as plasmonic effects [14]. Additionally, the eletron gas within metals can couple with light in the form of a surface wave called Surface Plasmon Polariton (SPP) [15].

Considering the fact that the goal of these devices is to supply an external load, the AC current has to be rectified by a properly sized diode [16–18]. A rectenna consists of a nanoantenna, filter circuits and a rectifying diode in order to convert free-propagating electromagnetic energy into DC power [18, 19].

In the following sections, metallic, dielectric, Seebeck, and aperture nanoantennas are presented, in order to select the best candidate to be employed in PV cells to enhance its performance.

2.2.1 Metallic Nanoantennas

This type of nantennas exploits the plasmonic properties of certain metals, like gold, silver, aluminum and copper, whose plasmonic properties are found in the optical range. A metallic nanoantenna consists of one or more metallic nanoparticles operating in a bandwidth near to plasmonic resonance of the used metal. This phenomenon happens when metallic nanoantennas capture the incident EM radiation at the resonant frequency. This induces a cyclic plasma movement of electrons and, consequently, the generation of an AC current, that flows onto the antenna feed point. Hence, a high electric field is concentrated at the center of the feed point [16]. Nanoantennas, like conventional antennas, can take on a multitude of shapes and designs, for instance monopole, dipole, bowtie and spiral.

The most basic type of nanoantenna is a monopole, represented in Figure 2.6, which consists of a single NP, that forms an electric field strengthening in its vicinity [16, 18, 20].

The dimer nanoantennas such as dipole and bowtie nanoantennas, concentrate the high electric field in the gap between two metallic Nanoparticle (NP)s. The intensification of the electric field in the gap between NPs greatly depends on the geometry of the NPs, the metal used, the gap width, the curvature of the NPs surface within the gap, and on properties of the environment as well [20].

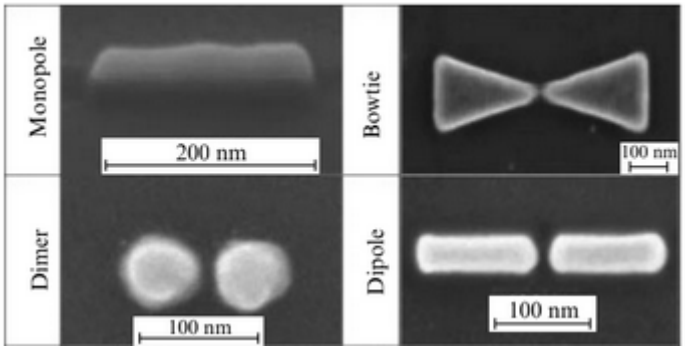

Figure 2.6: Main types of metal plasmonic nanoantenna.
(Adapted from: [20])

A dipole nanoantenna consists of two coupled nanorods or nanospheres. According to [20] and [16], the dipole nanoantenna's main advantages are the possibility of fine tuning of the operating mode (by introducing materials of different permittivities in the gap of the dipole), the simplicity of their fabrication, and the high confined electric field enhancement factor in the gap (much higher than in the monopole).

The bowtie nanoantenna which consists of two triangular shape NPs leveled along their axes with their apices facing each other, forming the feed gap. The performance of this design of nanoantenna depends on numerous geometrical parameters, such as the nanoantenna size, apex angle and gap size [17]. This type of nantenna presents a broad bandwidth, a high field confinement and enhancement in the gap region [16, 21]. An array can be assembled by coupling several bowtie elements by their feeding point and combining the electric field of the individual elements at the array feeding point [16,17].

Throughout the literature this structure has suffered transformations into more complex structures, like the rounded bowtie studied in [22], as well as cross configurations of the bowtie nanoantenna and rounded bowtie.

Furthermore, in [21] a new bowtie geometry is analysed, the arrow bowtie, represented in Figure 2.7, with a vertex angle of 50°, and 45° cut angle in its back side. The nanoantenna is sized in order to obtain a surface plasmonic resonance frequency of 350 THz (infrared range). The antenna has a length of 130 nm and a gap of 3 nm, it lays on a three-layer substrate, made up of 50 nm of silicon oxide, 250 nm of high conductivity silicon and 250 nm of aluminium. First, the authors of [21] optimized the substrate dimensions, which yielded optimum substrate dimensions of 700x800 nm. It showed that the directivity and field enhancement more than doubled when the substrate was properly tuned. The following step was to optimize the rear side vertex angle, by varying it between 45° and 50°. For a back side vertex angle of 50° the highest field enhancement was obtained, whereas for an angle of 45° there was more available power and a higher directivity.

Lastly, a comparison of an array of the classical bowtie with an arm length of 118.5 nm, 50° vertex angle and a 3 nm gap versus an array of the arrow bowtie designed. One can conclude that the new

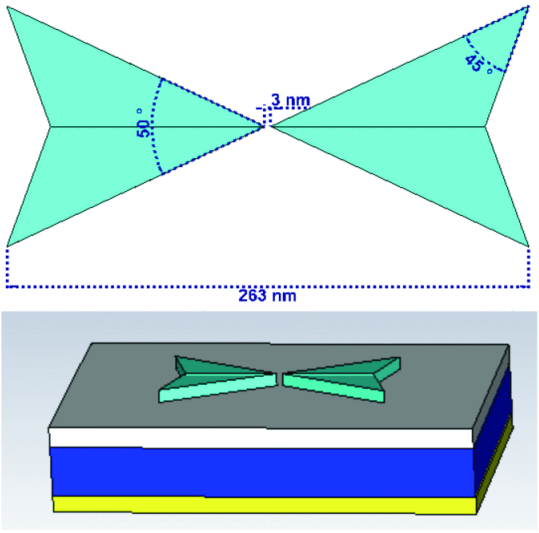

Figure 2.7: New bowtie design, arrow bowtie.
(Source: [21])

structure, arrow bowtie, has available power in the same order of magnitude, with significant improvements in terms of directivity and impedance.

In [22] a set of nanoantennas structures such as dipole, bowtie, rounded bowtie, cross bowtie, and rounded cross bowtie nanoantennas, made out of several different metals, i.e, silver, aluminum, gold, and copper, are studied. The highest Area Under the Curve (calculated by integrating the electrical field enhancement curve over the wavelengths of 800 nm to 1200 nm) is obtained by the cross bowtie antenna consisting of aluminum. Additionally, for each type of structure, aluminum was the material that yielded a higher AUC.

The square spiral nanoantenna, which is represented in Figure 2.8 concentrate the electric field in the feed point between two metallic arms [23]. This type of antenna presents a planar structure and circular polarization. The main advantage of the spiral nanoantenna is that it is a frequency-independent antenna, meaning its impedance, radiation pattern and polarization remain the same throughout a wide frequency range [16, 17, 23]. The bandwidth in which the antenna is frequency-independent is determined by the antenna size [23]. Additionally, spiral nanoantennas have a wide angle of incidence exposure and a high directivity, making it attractive for solar harvesting applications.

In the literature [23], a four element square spiral array showed a resonant frequency of 24.8 THz, which resulted in a maximum output current of 3.8 μA.

In [16], the following nanoantennas of interest are analysed, the dipole and bowtie, and finds that for the analysed geometries the dipole yielded the highest power density.

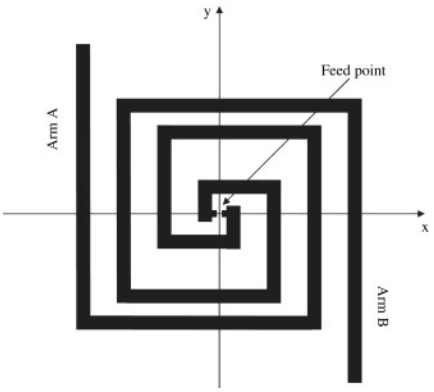

Figure 2.8: Square spiral nanoantenna.
(Source: [23])

2.2.2 Dielectric Nanoantennas

Metallic nanoantennas have a reduced range of working frequencies, since the metal utilized has large dissipative losses and result in low radiation frequency [16]. On the other hand, dielectric and many semiconductor materials display remarkably low dissipative losses in the optical range. Additionally, there is a wavelength range in which a dielectric particle of silicon, a material with high permittivity, can exhibit both electric and magnetic resonances. Their resonance response is associated to the formation of an effective resonator inside the particle [16, 20, 24]. The dielectric nanoantennas also contain the nanoantennas consisting of semiconducting particles, since this materials are considered transparent in the visible frequency range [16, 20].

2.2.3 Seebeck Nanoantennas

A Seebeck nanoantenna is a device that takes advantage of the thermoelectric properties of metal, in addition to the nanoantenna ability to confine optical energy [25]. The resonant currents in the structure cause a temperature gradient, which generates a DC voltage by Seebeck effect at the open ends of the structure. The Seebeck effect is a phenomenon in which a temperature difference between two dissimilar metals produces a potential difference between the two substances. When heat is applied to the metals, heated electrons flow toward the cooler metal. If the pair is connected through an electrical circuit, direct current (DC) flows through that circuit. The open circuit voltage of the Seebeck nanoantenna can be expressed as [25, 26]

$$V_{OC} = (S_A - S_B)\,\Delta T, \tag{2.9}$$

where ΔT is the difference in temperature between the center, where the hot spot occurs, and the open ends of the nanoantenna, where the cold spots occur, where the minimum temperature is located. Lastly, S_A and S_B are the Seebeck coefficients of the metals used.

The authors of paper [25] propose two Seebeck nanoantennas as seen in Figure 2.9, and chose titanium and nickel as the building materials, due to a considerable difference in their Seebeck coefficients (S_{Ni} = 19.5 μV/K and S_{Ti} = 7.19 μV/K) and their considerably low thermal conductivities to reach sufficient temperature gradients along the structures. The nanoantennas lie on top of a silicon-oxide layer, that acts like a thermal insulator, in order to achieve stronger temperature gradients. In this publication, for an incident light 10.6 μm the Ti-Ni junction reaches temperature differences of $\Delta T \approx 215\ mK$ and $2340\ mK$ that generates a low-voltage signals of $5.74\ \mu V$ and $9.08\ \mu V$ for the square and Archimedean spirals, correspondingly.

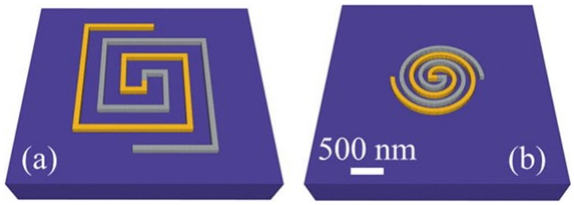

Figure 2.9: Example of Seebeck nanoantennas.
(Source: [25])

In [26] three structures are analyzed, such as dipole, bowtie, and spiral Seebeck nanoantennas. Results show that the square antenna has the broadest bandwidth and highest induced current of the analyzed structures, around 520 nA. Additionally, these types of devices can exhibit a voltage responsivity as high as 36 $\mu V/W$ for titanium-nickel dipoles resonant at far-infrared wavelengths.

2.2.4 Aperture Nanoantennas

Bethe was the first to theorize about the diffraction of a light wave passing through a slit much smaller than the light wavelength in a thin metal sheet. Bethe's theory expected that the power transmitted by the slit would decrease as the slit decreased, compared to the electromagnetic radiation wavelength. In 1998, Ebbesen demonstrated Bethe's theory to be wrong upon finding evidence of the Extraordinary Optical Transmission (EOT) phenomenon. The EOT is a phenomenon that occurs when a structure that exhibits subwavelength periodic apertures transmits more light than initially expected [15, 18].

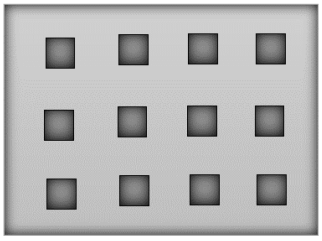

Figure 2.10: Aperture nanoantenna of 200 nm diameter arrays aperture with 1 μm period.
(Source: [18])

In other words, applying a light beam in a thick metallic film that contains a subwavelength slit array, resulting in an increase of incident light transmission, i.e., the subwavelength hole array transmits more light than a larger hole with the same area as the sum of all subwavelength slits [15, 18].

According to Wegner [27], there are three main type of aperture optical antennas,i.e., single aperture, single aperture surrounded by surface corrugations and an aperture array.

Due to its subwavelength dimension, a single aperture antenna does not exhibit significant control over the light emitted from the aperture, since directivity tends to zero with the decrease of aperture diameter [15, 27]. Directivity of an aperture antenna can be described as $D = 4\pi A/\lambda^2$, where A is the effective aperture area and λ is the radiation wavelength, which shows that the directivity tends to zero for a subwavelength aperture [27].

In reference [18] a nanoantenna with an array of air apertures is placed on top of a silicon PIN junction, in order to analyse the performance of the PIN junction with and without the nanoantenna. Several types of materials were tested for the antennas, such as aluminum, gold, and platinum. Other important parameters tested were the dimensions of the air slits, their spacing, and the metal thickness, which were all considered to have subwavelength dimensions. Additionally, the aluminum nanoantenna on top of a Silicon PIN junction displayed the highest value for the maximum absolute value of the normalized electric field along the intrinsic region, as compared with the other nanoantenna material types. The three slit array showed a strong EOT phenomenon, the normalized electric field along the intrinsic region yielded values as high as 10 times the incident electric field.

2.3 Diffraction Theories

Diffraction refers to several phenomena that occur when a wave encounters an obstacle or opening. In this section several diffraction theories will be studied, in order to understand the way the apertures influence the incident EM waves.

2.3.1 Huygens-Fresnel Principle and Young's Experiment

The Huygens principle establishes that each point of a primary wavefront serves as a continuous emitter of new waves, which he called secondary wavelets. These wavelets combine each other into a spherical wave, in the direction of propagation, that has the same frequency and speed as the original wave, represented by Figure 2.11 [6, 28]. Yet, if this assumption were correct, each secondary wavelet would emit uniformly in all directions. That is, in addition to the forward propagating wave-front, there would be a backward propagating wave-front, this is not the case [29].

In the case of a plane wave normal incident on an array of slits, each slit would be the equivalent of a source emitter. Thus, forming as many waves as the number of slits in the array. However, the principle

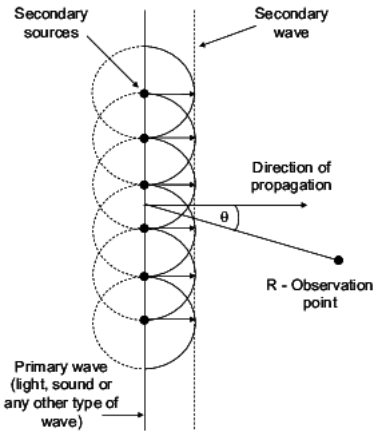

Figure 2.11: Schematic representation of Huygens principle.
(Adapted from: [29])

does not account for the distortions from the rectilinear propagation that arise when light encounters edges or apertures, known as diffraction effects. Later, Fresnel reviewed Huygens' principle for a curve wave-front, since near slits or apertures the wave is not plane. The Huygens principle joint with Fresnel's review is known as the Huygens-Fresnel Principle. It is the foundation of diffraction theories that can be used for several problems regarding wave propagation, diffraction, and reflection.

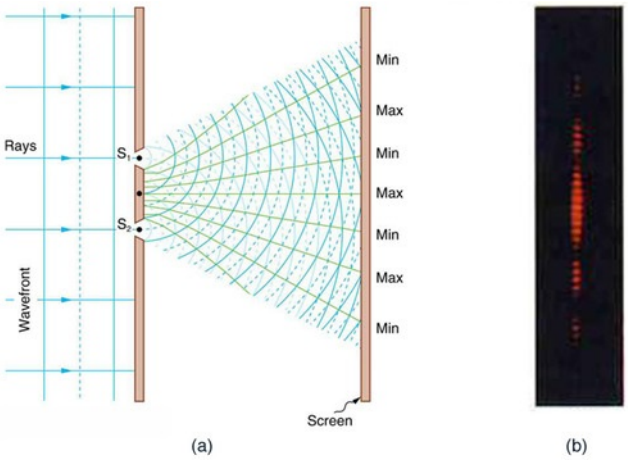

Figure 2.12: (a) Young's experiment geometry; (b) Double-slit pattern.
(Adapted from: [30])

The scientific community did not accept the theory that light was a wave until 1801, when English physicist Thomas Young performed his double-slit experiment, illustrated in Figure 2.12 [30]. Young was the first to confirm the Huygens-Fresnel Principle, by demonstrating the interference of the light waves with the double-slit experiment. The experiment consisted of light incident on a perfect conductive plane, a metal sheet with two slits, and a target, the screen, is placed in parallel to the plane. When the light passes through the slits, the waves spread out and interact with each other. The light diffracts from each

slit because the slits are narrow. These waves overlap and interfere constructively, seen as bright lines, and destructively, seen as dark regions, in Figure 2.12 (b) the interference pattern is illustrated.

2.3.2 Fraunhofer Diffraction Theory

To analyse the diffraction of light through an aperture, an important parameter to study is the irradiance $I(\theta)$ in W/m^2. The irradiance relates to the electric field by $I(\theta) \propto \langle E^2 \rangle$, allowing the comparison between theory and simulation results. According to Fraunhofer, the irradiance on the y' axis is characterized by equation 2.10, if a monochromatic plane wave goes through a slit with normal incidence, in a metal presumed to be a perfect conductor [6, 15], illustrated in Figure 2.13.

$$I(\theta) = I(0) \left(\frac{\sin(\beta)}{\beta} \right)^2 \tag{2.10}$$

Where $\beta = \frac{kb}{2} \sin\theta$, b size of the slit, $k = \frac{2\pi}{\lambda_0}$ is the wave vector and λ_0 is the wavelength of the incident plane wave [15].

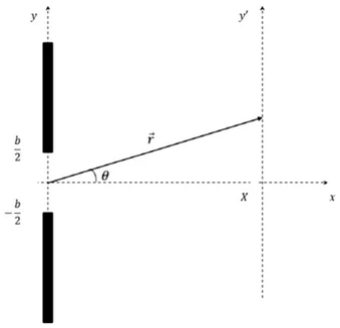

Figure 2.13: Representation of a perfectly conductive metal with a single slit.
(Adapted from: [15])

For $\theta = 0$, $\frac{\sin\beta}{\beta} = 1$ and $I(\theta) = I(0)$, it represents the main lobe of the diffraction pattern, in a perpendicular direction to the slit orientation, particularly the x direction, in this case.

When the metal sheet has multiple slits, the diffraction pattern does not match to the sum of the diffraction patterns of each slit, instead it must take into account the interference terms [6]. The Fraunhofer approximation can be generalized by equation 2.11.

$$I(\theta) = I_0 \left(\frac{\sin(\beta)}{\beta} \right)^2 \left(\frac{\sin(N\alpha)}{\sin\alpha} \right)^2 \tag{2.11}$$

Where $\alpha = \frac{kd}{2} \sin(\theta)$, d is the distance between slits, and N is the number of slits [28].

2.3.3 Kirchhoff Diffraction Theory

The Kirchhoff diffraction formula is a good approximation of experimental measurements for calculated intensities in the region directly in front of the slit for small wavelengths of incident waves compared to slit size. However, when the wavelength is large compared to the opening size, the Kirchhoff formula proves to be inaccurate [31].

Nevertheless, the Huygens-Fresnel diffraction results can be derived from the Kirchhoff theory, when applied to a scalar wave function, present in equation 2.12.

$$\nabla^2\psi + k_0^2\psi = 0 \tag{2.12}$$

Through the application of the Green theorem to equation 2.12, comes equation 2.13.

$$\boldsymbol{\psi}(r) = \frac{1}{4\pi}\int\left[\frac{\partial\overline{\psi}}{\partial\boldsymbol{n}}\frac{e^{ik_0r}}{r} - \overline{\psi}\frac{\partial}{\partial\boldsymbol{n}}\frac{e^{ik_0r}}{r}\right]dS \tag{2.13}$$

Where S represents the entire surface that extends from $-\infty$ to $+\infty$, in the x and y directions,as represented in Figure 2.11 [15]. where $\psi = 0$ and $\dfrac{\partial\overline{\psi}}{\partial n} = 0$ on the right side of the surface, and that $\psi = \psi_0$ in the slit region, where ψ_0 is the field intensity of the incident wave without any disturbances.

However, boundary conditions are not full-filled at the metal surface on Kirchhoff's theory, considering he assumed an opaque and finite plane. Since the incident and reflected waves do not exist over the surface, these conditions are not satisfied, specially on surfaces near the slits. For subwavelength structures and for near-field regime, this cannot be neglected [28].

2.3.4 Bethe-Bouwkamp Diffraction Theory

In 1994, Bethe proposed a new diffraction theory through a circular aperture in a perfect conductive metal surface to tackle Kirchhoff's diffraction theory limitations. Bethe determined an analytical solution for the electromagnetic field near a subwavelength circular aperture, in a perfect conductive metal surface, polarized along the x direction and propagating along z.

Bethe's theory relays on three essential assumptions. The first assumption is that the incident and reflected waves occur over the surface. The second assumption is considering the conductivity is infinite, thus the incident electromagnetic wave does not penetrate the surface. Lastly, it assumes that the electric field component, $\overline{E}$, is tangential to the surface, and the magnetic field component, $\overline{H}$, is perpendicular to the surface [6, 15].

In rectangular coordinates, if the origin is at the center of the circular aperture , and the z axis is perpendicular to the aperture plane, the aperture region is defined by $x^2 + y^2 \leq a$, where a is the aperture's radius, which is smaller than the wavelength.

The equations that describe the electromagnetic fields are given by the set of equations 2.14 and 2.15 in oblate-spheroidal coordinates.

$$\begin{cases} \overline{E}_x = jkz - \dfrac{2}{\pi} jkx \left(\arctan(v) + \dfrac{v}{1+v^2} \right) \\ \overline{E}_z = 2jkz - \dfrac{4}{\pi} jkau \left(1 + v \arctan(v)\right) \end{cases} \tag{2.14}$$

$$\begin{cases} \overline{H}_x = -\dfrac{4xyu}{\pi a^2 \left(u^2+v^2\right)\left(1+v^2\right)} \\ \overline{H}_y = 1 - \dfrac{2}{\pi}\left[\arctan(v) + \dfrac{v}{u+v^2} \right] + \dfrac{2\left(x^2-y^2\right)v}{\pi a^2 \left(u^2+v^2\right)\left(1+v^2\right)^2} \\ \overline{H}_z = -\dfrac{4ayu}{\pi a^2 \left(u^2+v^2\right)\left(1+v^2\right)} \end{cases} \tag{2.15}$$

$$\begin{cases} x = a\sqrt{(1-u^2)(1+v^2)}\cos\varphi \\ y = a\sqrt{(1-u^2)(1+v^2)}\sin\varphi \\ z = auv \end{cases}$$

Where a is the radius of the slit, and the rectangular coordenates x, y, and z are given by expression 2.3.4, with $0 \leq u \leq 1$, $-\infty < v < +\infty$, and $0 \leq \varphi \leq 2\pi$.

Later, Bouwkamp reviews the theory of Bethe and concludes that in the near field region Bethe's results were faulty, due to discontinuities in the considered boundary conditions. Consequently, Bouwkamp adjusted Bethe's boundary conditions and recalculated the fields. The magnetic field expression was unchanged, but the electric field expression was rectified for equation 2.16.

$$\begin{cases} \overline{E}_x = \dfrac{4jk}{3\pi} \dfrac{2a^2 - x^2 - 2y^2}{\sqrt{a^2 - x^2 - y^2}} \\ \overline{E}_y = -\dfrac{4jk}{3\pi} \dfrac{xy}{\sqrt{a^2 - x^2 - y^2}} \\ \overline{E}_z = 0 \end{cases} \tag{2.16}$$

The expressions considered by Bethe, for the far field region, were confirmed by Bouwkamp.

In conclusion, when light goes through a slit in a metal surface, it drives surface current and concentrates charge at the edges of the slit. The accumulated charge results in an intensification of the electric field inside the slit, therefore enhancing the far field diffracted light. Consequently, a metallic aperture can focus and transmit electromagnetic waves with increased efficiency, performing as an antenna.

However, classic diffraction theories do not describe the EOT phenomena, either the generation

and propagation of SPPs, that are such crucial optical properties that are linked with nanoantennas operation. Thus, there need to be additional mechanisms to diffraction theories in order to describe these phenomena. In the following sections, wave propagation theories regarding light-matter interactions will be discussed, in an effort to provide better insight into the nanoantennas' behavior.

2.3.5 Radiation Zones

Through the evolution of Diffraction theories explored in the prior subsections, it is possible to conclude that the perceptible fields in the target screen depend not only on the aperture design but also on its distance from the target. Additionally, the shape of the EM field is affected as well as its intensity. By taking this into account, radiation zones are defined, in which determined Diffraction theory applies based on the behaviour of the field at that distance from the aperture, as seen in figures 2.14 and 2.15.

As previously stated, when a plane wave goes through a slit, it takes up a spherical nature instead, resulting in interactions between the emitted waves. Due to these interactions, regions with distinct field characteristics arise, represented in figure 2.14. Additionally, an array of slits behaves like an antenna, commonly known as an aperture antenna. Assuming that the antenna is smaller than twice the wavelength it emits, the short antenna approximation describes the fields present in figure 2.15.

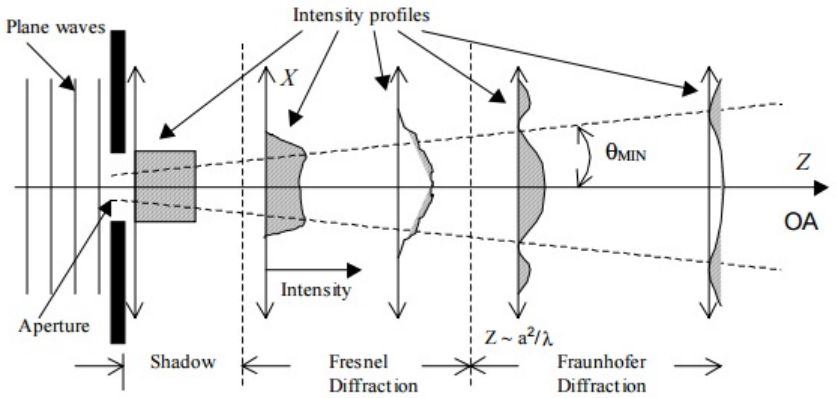

Figure 2.14: Diffraction of plane wave at aperture.

Defining d as the distance between the source(slit) and the target, the Far-Field region is for distances greater than twice the wavelength, $d > 2\lambda$. This region is also known as the Fraunhofer region since the EM field and radiation pattern follow the Fraunhofer Diffraction Theory. In this region, the pattern shape is independent of the distance the target distance, i.e., the pattern maintains its shape if the target moves. However, the greater the distance from the source, the smaller the peaks are. Furthermore, when the distance tends to infinity, the pattern is uniform, meaning a constant step, due to the intensities being so diminished that they are all the same.

For the Near-Field, there are two distinct regions a radiative one, and a reactive one. The radiative

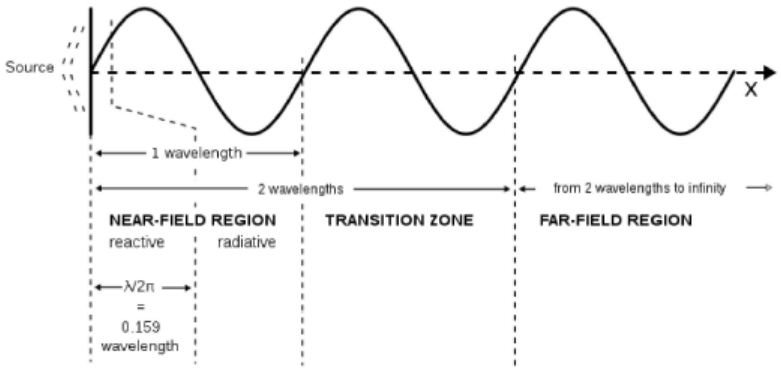

Figure 2.15: Radiation zones for a short antenna.

region is known as the Fresnel region, where the distance to the target is given by $\frac{\lambda}{2\pi} < d < \lambda$. In contrast with the Fraunhofer region, the Fresnel region radiation pattern shape varies with the target distance to the source. In this region, the EM field is described by the Fresnel-Kirchhoff Diffraction theory, which consists of a near-field approximation of the Kirchhoff Diffraction theory.

Lastly, the reactive region lies in $0 < d < \frac{\lambda}{2\pi}$, and the array's material influences the pattern shape. If the array consists of perfect conductor material, it is opaque, i.e., EM fields cannot penetrate it, resulting in all the radiation coming from the slit. In turn, the pattern shape mimics the array shape perfectly. On the other hand, if the material is not a perfect conductor, another EM contributions should be considered. For instance, the propagation of evanescent waves on the material can pass through it and interact with the shape pattern.

2.4 Light-matter interactions

In this work, we want to incorporate subwavelength aperture optical antennas in solar cells in an effort to improve the overall efficiency of the solar cell, through exploiting the light trapping characteristics of the aperture optical antennas. In the following sections the behavior of metals at optical frequencies will be studied, which is essential to understand and characterize the operation of optical antennas.

2.4.1 Optical Properties of Metals

It is particularly important to characterize the metals' optical behaviour since optical antennas rely on the resonance and plasmonic characteristics of the metals as a way to enhance radiation. The dielectric permittivity is the physical quantity that describes the metal's behaviour under an external electric field.

The Drude-Lorentz model describes the metals' properties at optical wavelengths by a complex dielectric function. In 1900, Paul Drude depicted the behaviour of the metals' electrons as those of an ideal gas, hence the Drude model, also known as the free-electron model. Later, this model proved incomplete as it only describes the intraband electron transitions or the free-electron effects, conveying metals' behaviour at infrared wavelengths and higher, presented on equation 2.17 [15, 32, 33].

$$\overline{\varepsilon}_{Drude}(\omega) = 1 - \frac{\Omega_p^2}{\omega(\omega + j\Gamma_0)} \tag{2.17}$$

Subsequently, to characterize the interband electron transitions(or bound-electron effects), an equivalent to the Lorentz insulators' model is added to the complex dielectric function, represented by equation 2.18.

$$\overline{\varepsilon}_{bound}(\omega) = \sum_{n=1}^{N} \frac{f_n \omega_p^2}{(\omega_n^2 - \omega^2) - j\omega\Gamma_n} \tag{2.18}$$

Thus, expanding the model to near-infrared and visible wavelength region. The Drude-Lorentz model describes the frequency dependence of the metal's permittivity, relating the dielectric function with the incident wave wavelength through equation 2.19. In this equation, ω_p is the metal's plasma frequency, N is the number of resonances with resonance frequency ω_n, with a certain oscillator's strength f_n and damping coefficient Γ_n. The Ω_p is the plasma frequency related with intraband transitions given by $\Omega_p = \sqrt{f_0}\omega_p$, with oscillator strength f_0 and damping coefficient Γ_0 [15, 32, 33].

$$\overline{\varepsilon}_{DL}(\omega) = 1 - \frac{\Omega_p^2}{\omega(\omega + j\Gamma_0)} + \sum_{n=1}^{N} \frac{f_n \omega_p^2}{(\omega_n^2 - \omega^2) - j\omega\Gamma_n} \tag{2.19}$$

In 1998, Rakic et al. conducted a fitting of the Drude Lorentz model parameters for several metals. However, this study focuses on four metals, silver (Ag), aluminium (Al), gold (Au) and copper (Cu), for which table 2.2 contains the parameters previously mentioned [34].

Table 2.2: Drude-Lorentz parameters.

Parameters	Ag	Al	Au	Cu	
$\hbar\omega_p$	9.01	14.98	9.03	10.83	eV
f_0	0.845	0.523	0.760	0.575	
Γ_0	0.048	0.047	0.053	0.03	eV
f_1	0.065	0.227	0.024	0.061	
Γ_1	3.886	0.330	0.241	0.378	eV
ω_1	0.816	0.162	0.415	0.291	eV
f_2	0.124	0.050	0.010	0.104	
Γ_2	0.452	0.312	0.345	1.056	eV
ω_2	4.481	1.544	0.830	2.957	eV
f_3	0.011	0.166	0.071	0.723	
Γ_3	0.065	1.351	0.870	3.213	eV
ω_3	8.185	1.808	2.969	5.3	eV
f_4	0.840	0.030	0.601	0.638	
Γ_4	0.916	3.382	2.494	4.305	eV
ω_4	9.083	3.473	4.304	11.18	eV
f_5	5.646	-	4.384	-	
Γ_5	2.419	-	2.214	-	eV
ω_5	20.29	-	13.32	-	eV

Through equation 2.19, it was possible to obtain the following curves for the studied metals' complex dielectric function.

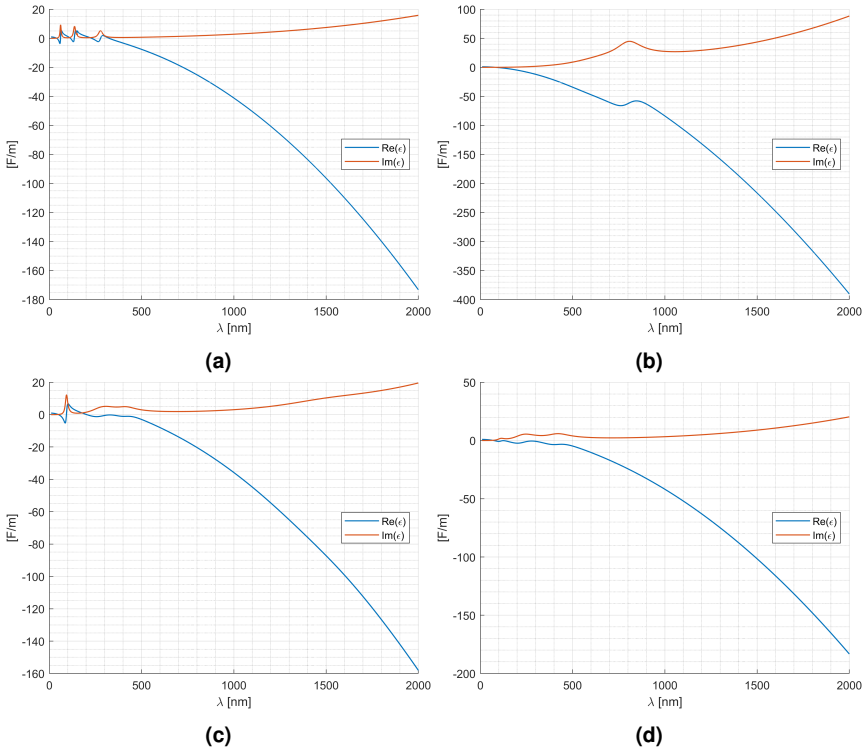

Figure 2.16: Complex Dielectric Function: (a) Silver; (b) Aluminium; (c) Gold; (d) Copper.

In figure 2.16, it is evident the analyzed metals permittivity real part, $\mathfrak{Re}(\varepsilon)$, is predominantly negative and decreases for the longer wavelengths. This property is essential for the emergence of SPPs and their subsequent propagation.

2.4.2 Extraordinary Optical Transmission (EOT)

The EOT was first observed by Ebbesen in 1998 [35]. It was determined that the normalized to hole area transmission was several orders of magnitude larger than what was estimated by Bethe's theory, reaching even a value greater than one [36]. In other words, EOT is an optical phenomenon where a structure, featuring subwavelength apertures in an opaque screen, transmits more light than would be expected. When in EOT, the nanoantenna has a transmission efficiency a several orders of magnitude greater than the predicted by classical aperture theory [6]. The optical properties are a result of plasmons coupling with light on the surface of the metal film, hence creating SPPs.

2.4.3 Surface Plasmon Polaritons

A plasmon oscillation can be defined as the joint movement of conduction band electrons relative to fixed positive ions in a metal that is subjected to the incident light electric field [37]. These oscillations are propagating waves with a distinct frequency and wave vector. When these types of oscillations are present at the interface between a conductor and a dielectric, i.e., a dielectric-metal interface, they are labeled Surface Plasmons (SPS) [6, 15]. Surface plasmons can couple the light in the form of a surface wave originating SPPs. The SPPs are surface EM waves that propagate along the dielectric-metal interface plane. As a result, the fields are strongly confined between the metal and the dielectric.

In order for SPPs to take place, a few conditions must be met, the metal must present electric permittivity with negative real part, at the incident light frequency. As well as, the wave vector component of the incident light that is parallel to the dielectric-metal interface must be matched with the wave number of the SPP. For optical frequencies, few metal can satisfy the first condition, for instance Gold, Silver, Copper and Aluminium. Additionally, due to boundary conditions imposed by Maxwell's equations, the SPP cannot be excited by TE waves, it can only be excited by TM waves [15].

As previously mentioned, an SPP can only be excited by a TM-polarized wave. One says the light is Transverse Magnetic polarized when the magnetic field is perpendicular to the plane of incidence. In isotropic materials, such as metal, the electric field is perpendicular to the magnetic field for TM waves.

In figure 2.17, an incident TM wave is portrayed at a dielectric-metal interface. Where the first medium is a dielectric with complex permittivity $\overline{\varepsilon}_d$, and the second medium is a metal with complex permittivity $\overline{\varepsilon}_m$. Both mediums are presumed to extend throughout the z-axis and are non-magnetic. The incident TM wave wave-vector is expressed by $\overline{\boldsymbol{k}} = [\overline{k}_x, 0, \overline{k}_z]$, while the electromagnetic field follows equation

2.20, in which ω is the incident light angular frequency, and p is d or m for dielectric or metal, respectively.

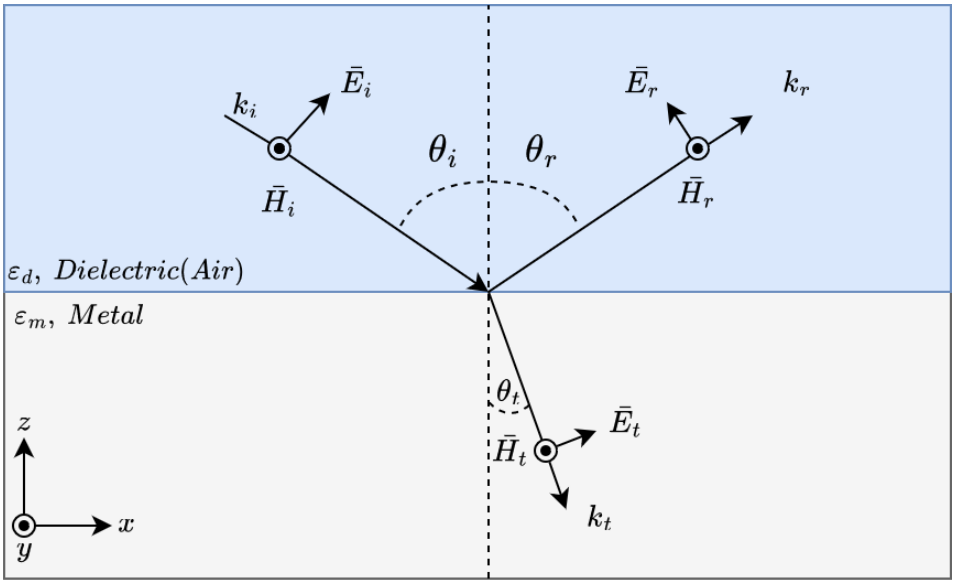

Figure 2.17: Propagation of a TM wave in a dielectric-metal interface.

$$\begin{cases} \overline{E}_{x,p}(x,y,z,t) = E_0 e^{j\left(\overline{k}_x x + \overline{k}_{z,p}|z| - \omega t\right)} \\ \overline{E}_{z,p}(x,y,z,t) = \pm\frac{\overline{k}_x}{\overline{k}_{z,p}} E_0 e^{j\left(\overline{k}_x x + \overline{k}_{z,p}|z| - \omega t\right)} \\ \overline{H}_{y,p}(x,y,z,t) = H_0 e^{j\left(\overline{k}_x x + \overline{k}_{z,p}|z| - \omega t\right)} \end{cases} \tag{2.20}$$

Due to the lack of surface charges, the boundary conditions imply that the tangential components of the electromagnetic field should be continuous along the interface, resulting in the following conditions $\overline{E}_{x,d} = \overline{E}_{x,m}$ and $\overline{H}_{y,d} = \overline{H}_{y,m}$.

In that case, it is possible to extrapolate from Maxwell's equations the deduction present in equation 2.21 and equation 2.22, which in turn allows obtaining the SPP dispersion relation, i.e, $\mathfrak{Re}(\overline{k}_x)$, where k_0 is the incident wave-vector expressed trough $k_0 = \omega/c_0$, for which c_0 is the light speed in the vacuum. Additionally, a perpendicular wavevector component $\overline{k}_{z,p} = \left(\overline{\varepsilon}_p k_0^2 - \overline{k}_x^2\right)^{\frac{1}{2}}$, which will not be taken into account.

$$\nabla \times \overline{H} = \overline{\varepsilon}\frac{\partial \overline{E}}{\partial t} \Rightarrow \begin{cases} \frac{E_0}{H_0} = -\frac{\overline{k}_{z,m} c_0}{\overline{\varepsilon}_m \omega} \\ \frac{E_0}{H_0} = \frac{\overline{k}_{z,d} c_0}{\overline{\varepsilon}_d \omega} \\ \overline{k}^2 = \overline{k}_x^2 + \overline{k}_z^2 \end{cases} \Rightarrow \begin{cases} \frac{\overline{k}_{z,m} c_0}{\overline{\varepsilon}_m \omega} + \frac{\overline{k}_{z,d} c_0}{\overline{\varepsilon}_d \omega} \\ \overline{k}_x^2 + \overline{k}_{z,p}^2 = \overline{\varepsilon}_p \left(\frac{\omega}{c_0}\right)^2 \end{cases} \tag{2.21}$$

$$\overline{k}_x = k_0 \sqrt{\frac{\overline{\varepsilon}_m(\omega)\overline{\varepsilon}_d(\omega)}{\overline{\varepsilon}_m(\omega) + \overline{\varepsilon}_d(\omega)}} \tag{2.22}$$

The SPP dispersion relation curves allow us to identify resonance frequencies that appear when the SPP

dispersion curve is on the right of the light curve, given by equation 2.23, n being the dielectric refractive index. In this case, the dielectric medium is air, and it is assumed that $\overline{\varepsilon}_d = 1$(real and with no losses). Since SPPs propagate when the dispersion curve is on the right of the light curve, they present a smaller wavelength than the radiation in free space, therefore presenting an evanescent decay, implying that the fields exponentially decay away from the surface.

$$\omega = c_0 \frac{\mathfrak{Re}(\overline{k}_x)}{n\sqrt{\overline{\varepsilon}_d(\omega)}} \tag{2.23}$$

The SPPs dispersion curves are obtained through the application of equation 2.22 for the metals previously described by the Drude-Lorentz model, yielding the curves present in figure 2.18 for the real part of the wavevector, where the black dashed line represents the light curve, and the curves present in figure 2.19 for the imaginary part of the wavevector.

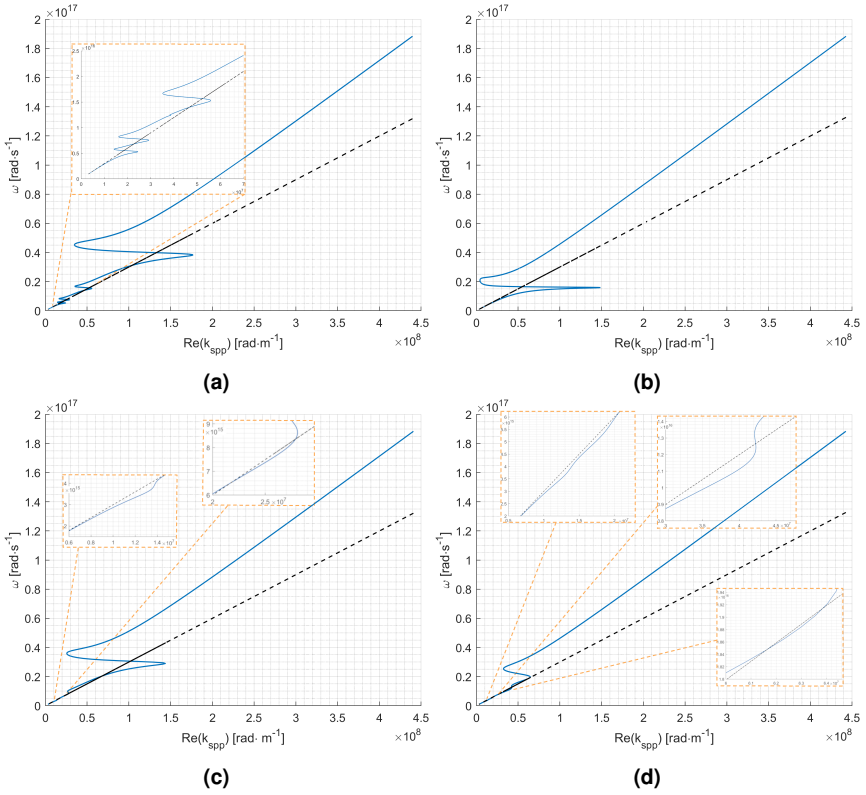

Figure 2.18: Real SPP dispersion relation curves: (a) Silver; (b) Aluminium; (c) Gold; (d) Copper.

For $\mathfrak{Re}(\overline{\varepsilon}_m) > 0$ the x and z components of the wavector are purely real, therefore resulting in radiative or unbound modes. This happens to the left of the light curve for angular frequencies higher than the plasma frequency, $\omega > \omega_p$.

On the other hand, when the metal's dielectric permittivity is between minus the dielectric's permittivity and zero, $-\varepsilon_d < \mathfrak{Re}(\overline{\varepsilon}_m) < 0$, the imaginary par of $\overline{k}_x$ is far greater than the real part,

$\mathfrak{Im}(\overline{k}_x) \gg \mathfrak{Re}(\overline{k}_x)$, leading to quasi-bound propagation modes. In terms of angular frequency these modes take place for frequencies between $\frac{\omega_p}{\sqrt{1+\varepsilon_d}}$ and ω_p, meaning $\frac{\omega_p}{\sqrt{1+\varepsilon_d}} < \omega < \omega_p$. The fact that $\mathfrak{Im}(\overline{k}_x)$ exhibits high values grants the waves an evanescent decay. These waves decay exponentially with distance from the interface at which they are formed, the dielectric-metal interface.

Lastly, at metal's permittivity values bellow minus the dielectric's permittivity, $\mathfrak{Re}(\overline{\varepsilon}_m) < -\varepsilon_d >$, $\overline{k}_x$ is mostly real while $\overline{k}_z$ is predominantly imaginary resulting in bound modes of propagation. This behaviour takes place at frequencies bellow $\frac{\omega_p}{\sqrt{1+\varepsilon_d}}$, for $\omega < \frac{\omega_p}{\sqrt{1+\varepsilon_d}}$.

Resonance frequencies located in the range of radiative or bound modes, the metal transmission is very high, behaving like a transparent material. The real part of the wave-vector $\overline{k}_x$ approaches asymptotically the limit that separates quasi-bound from bound modes, which is given by $\frac{\omega_p}{\sqrt{1+\varepsilon_d}}$.

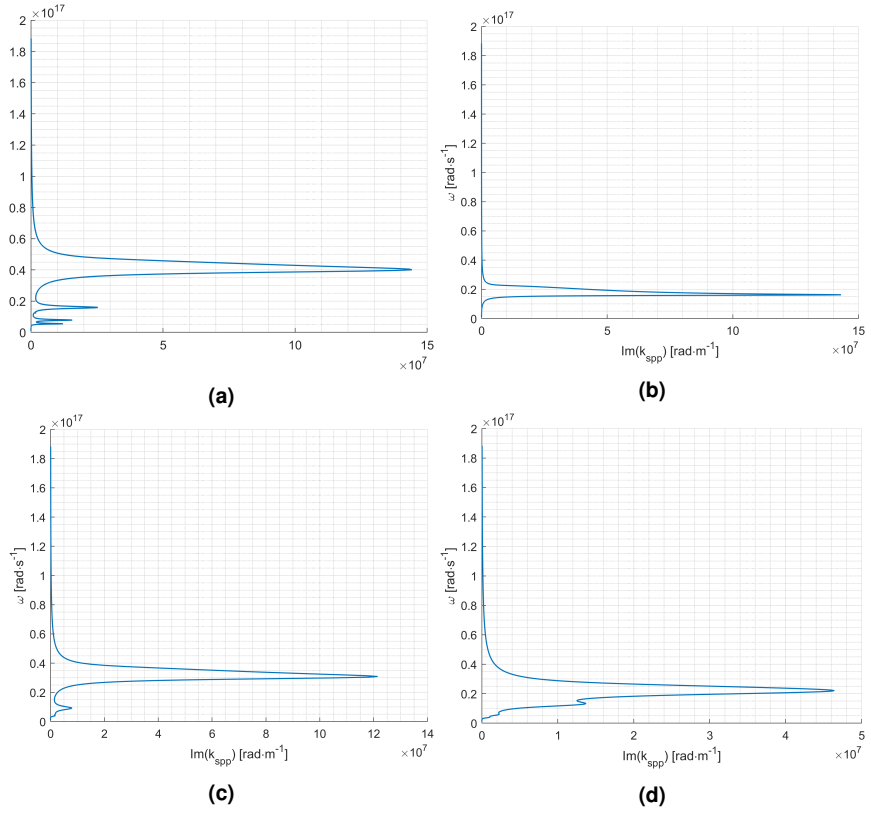

Figure 2.19: Imaginary SPP dispersion relation curves: (a) Silver; (b) Aluminium; (c) Gold; (d) Copper.

Through analysis of figure 2.18 it is attainable the resonance wavelengths for the several air-metal interfaces for the studied metals, by retrieving the frequencies corresponding to peak values of $\mathfrak{Re}(\overline{k}_x)$ to the right of the light curve. In table 2.3, the mentioned resonance wavelengths are illustrated.

Silver presents four resonance wavelengths, three in the UV at 49, 123, and 249 nm and one in the Visible spectra at 355 nm. On the other hand, for Aluminium, there is a single resonance wavelength in the UV spectra at 119 nm. For gold, there are three resonance frequencies, two of which are in

the UV, at 64 and 238 nm, and one in the Visible at 536 nm. Lastly, Copper presents four resonance wavelengths, two in the UV at 100 and 158 nm, and two in the Visible at 360 and 526 nm.

Table 2.3: Obtained resonance wavelengths.

	Aluminum	Gold	Silver	Copper
λ nm	119	64 238 536	49 123 249 355	100 158 360 526

3

Developed Model

Contents

This chapter contains the description in detail of the model developed and numerical simulation using Finite Element Software COMSOL Multiphysics®.

3.1 Physics and Models

COMSOL Multiphysics is a Finite Element Analysis software, a numerical method used in mathematics and engineering to determine approximate solutions for differential equations. The software *COMSOL Multiphysics* allows for several types of physics interfaces. The physics interfaces employed are the Radio Frequency interfaces which compute the electric and magnetic fields in high-frequency systems. This interface possesses other subinterfaces, such as the Electromagnetic Waves, Frequency Domain interface that solves for time-harmonic electromagnetic field distributions. A Frequency Domain type of study is applied for source driven simulations for a single frequency or a sequence of frequencies.

Consequently, this physics interface solves the time-harmonic wave equation for the electric field described by equation 3.1, which presents solutions in the form of equation 3.2.

$$\nabla \times (\nabla \times \boldsymbol{E}) - k_0^2 \varepsilon_r \boldsymbol{E} = 0 \tag{3.1}$$

$$\boldsymbol{E}(x, y, z) = \overline{\boldsymbol{E}}(x, y)\, e^{-ik_z z} \tag{3.2}$$

The materials' models used are included in the *COMSOL* software. For metals, the 1998 Rakic fitting is used, which is found under the Inorganic Materials in the Optical section of the Materials. Therefore, the metals' permittivity follow the curves already studied in figure 2.16. The employed dielectric is air which is characterized by a constant, and real permittivity equal to unity. Lastly, the semiconductor chosen is Silicon (Si), which is characterized by the Aspnes and Studna fitting from 1983.

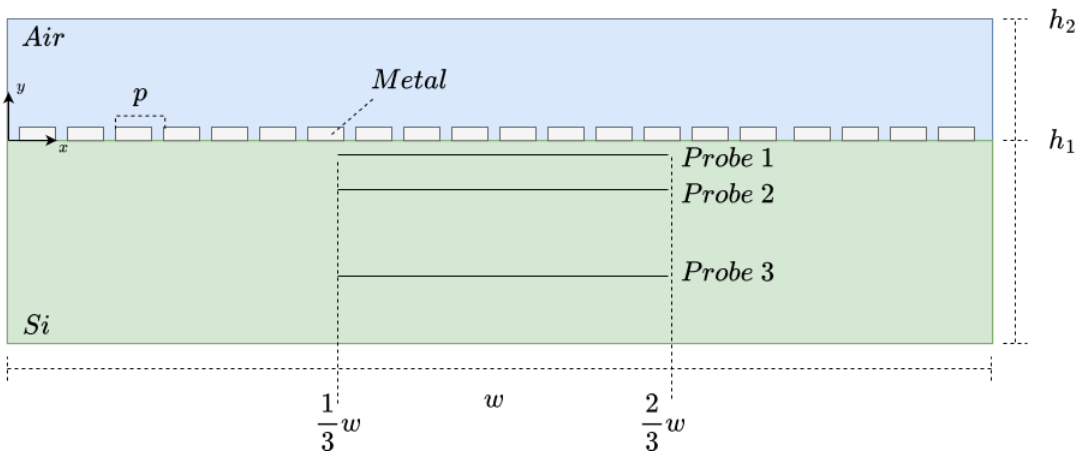

Figure 3.1: Illustrative representation of the model.

In terms of structure, the design follows the representation in figure 3.1, where the width of the structure , w, is 9.05 μm. The design is composed by a dielectric layer (air), where an array of metal nanoantennas is contained, and a semiconductor layer. The developed model is bidimensional (2D) in order to reduce computation time. This approximation represents a transversal cut of a tridimensional structure, and this may be valid due to the fact that the transversal section is representative of the tridimensional device. Any two transversal planes drawn will be the same. The semiconductor layer has a height, h_1, of 2.2 μm, and the dielectric layer has a height, h_2, of $\frac{1}{3}h_1$. The metal nanoantenna's height depends on the geometry in analysis since different geometries are studied. However, the period, p, remains constant with a value of 450 nm. Similarly, the number of elements in the array is constant at 20 elements.

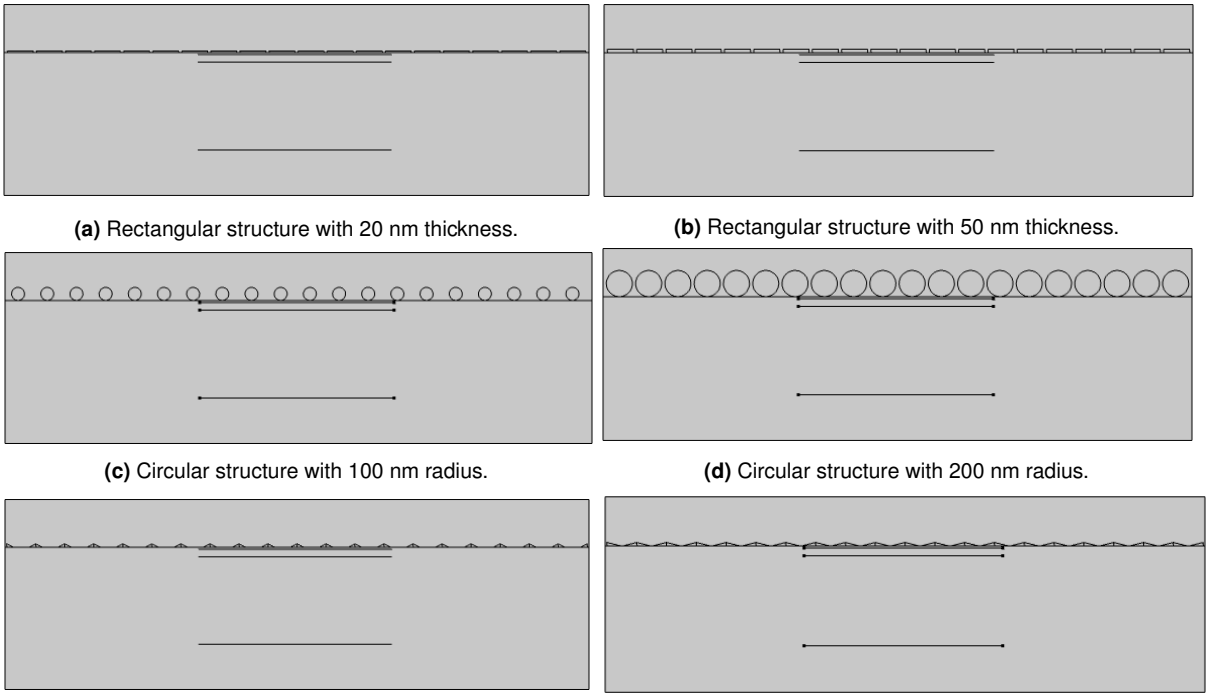

(a) Rectangular structure with 20 nm thickness.

(b) Rectangular structure with 50 nm thickness.

(c) Circular structure with 100 nm radius.

(d) Circular structure with 200 nm radius.

(e) Triangular structure with 100 nm base and 50 nm height.

(f) Triangular structure with 200 nm base and 50 nm height.

Figure 3.2: The different structure designs.

Additionally, the coordinate plane origin defined as the dielectric-metal interface left corner. This implies that for y higher than zero, it is in the dielectric medium, and for y bellow zero, it is in the semiconductor medium.

In the Frequency Domain study, it is necessary to define several Scattering Boundary Conditions. The initial values of the electric field are all set to zero. The incident electric field originates at $y = h_2$ and only has the x component different from zero, with an amplitude of 1 V/m.

3.1.1 Scattering Boundary Conditions

The Scattering Boundary Condition defines a boundary transparent for a scattered wave. The boundary is only perfectly transparent for scattered (outgoing) waves of the selected type at normal incidence to the boundary. That is, a plane wave at oblique incidence is partially reflected and so is a cylindrical wave or spherical wave unless the wavefronts are parallel to the boundary. That is, at the boundary the wave is decomposed into two components, perpendicular and parallel. The perpendicular component is absorbed at the boundary. Meanwhile, the parallel component keeps propagating. This condition is applied for $x = 0$, $x = w$, and $y = -h_1$ giving rise to well-defined boundaries.

3.1.2 Probe Placement

A crucial step in the model design is the definition of three probes present in figure 3.1. The distance from the dielectric-semiconductor interface is defined following the radiation zones established in subsection 2.3.5, where each probe corresponds to the limit of the zones. Hence, the minimum wavelength considered for the delimitation of the radiation zones was 200 nm, even though some of the studies include shorter wavelengths that would yield distances too close to the interface for the overall range of frequencies studied. Moreover, the maximum wavelength studied is 700 nm, the upper limit of the visible spectrum. Consequently, at $d_1 = -\frac{200}{2\pi}$ nm is defined probe 1, at $d_2 = -200$ nm is located probe 2, and lastly, probe 3 is at $d_3 = -1500$ nm, since it is larger than twice 700 nm. As for the length of the probes, they are all $\frac{1}{3}w$ long, spanning from 3 μm to 6μm, in order to avoid the waves that might be reflected from the boundaries previously defined. That is, if the probe spanned throughout the entire semiconductor layer, from boundary to boundary, the electric field maxima would've probably been in the boundary points due to the interaction between the reflected waves at the boundary.

3.1.3 Frequency Ranges

As formerly mentioned, the Frequency Domain study is applied to the simulation for a sequence of frequencies. The frequency ranges were all obtained similarly. In figure 2.5, it can be observed that Si has an absorption coefficient maximum at 200 nm. Furthermore, the Visible Spectrum ranges from 400 nm to 700nm, noting with special importance that the Sun's radiation peak intensity is at a wavelength of approximately 500 nm. Consequently, a linearly spaced vector starting from 200 nm to 700 nm, with a spacing of 50 nm is created as a start. To this vector are then added the metal resonances obtained in table 2.3, depending on which metal is present in the structure. The resulting vector is then converted to THz and the simulation frequency ranges are defined.

3.1.4 Nanoantenna Geometry

The study focuses on three aperture metal nanoantenna geometries rectangular, circular and triangular. In the rectangular geometry, the simulations are conducted for a metal thickness of 20 nm, present in figure 3.2a, and 50 nm, as seen in figure 3.2b, with a width of 400 nm. On the other hand, in the circular geometry, the circle is tangent to the dielectric-semiconductor interface, and it was tested for a radius of 100 nm (figure 3.2c) and 200 nm (figure 3.2d). Lastly, the triangular geometry, where the array consists of two triangles with base b side by side, with a base of 100 nm and 200 nm, as illustrated in figures 3.2e and 3.2f, respectively.

3.1.5 Mesh

The Mesh defines the discretization of the geometry, which divides the geometry into small units of simple shapes (mesh elements), allowing the computation of approximate solutions over each mesh element rather than the entire geometry. The type of mesh element is triangular, with a maximum element size of 6.767E-7 m, a minimum element size of 2.03E-8 m, and a maximum element growth rate of 1.5.

4

Results

Contents

4.1 Si Cell Without Nanoantennas

To set a comparative base, the case without any nanoantenna is simulated, yielding the results in figure 4.1, for the first probe. The analyzed values are the electric field and the integral of the field along the probe (line integral). For solar technology, it is essential to study these values because a larger field translates into a higher concentration, which in turn can lead to the possibility of reducing the area of the cell to produce the same amount of energy.

On the other hand, the field integral, which represents the sum of the electric field at the probe (and which is proportional to the total intensity on it), allows us to conclude the absorption in the silicon, that is, if we compare two probes, for example, 1 and 2, and the value of the field integral decreases from probe 1 to probe 2, then it is assumed the Silicon absorbs the field, neglecting the field that travels out from the probe's plane. From the simulation it is possible to extract the value of the electric field along the probes. Subsequently, the value of the the field integral is obtained along the probe, this value allows to study how quickly the electric field is absorbed in the semiconductor.

Analysing figure 4.1, it is possible to extrapolate the maximum electric field value for the standalone Si cell, at a wavelength of 700 nm, results $|E_{max}| = 4.22E-01$ V/m and $\int E = 1.250E-06$.

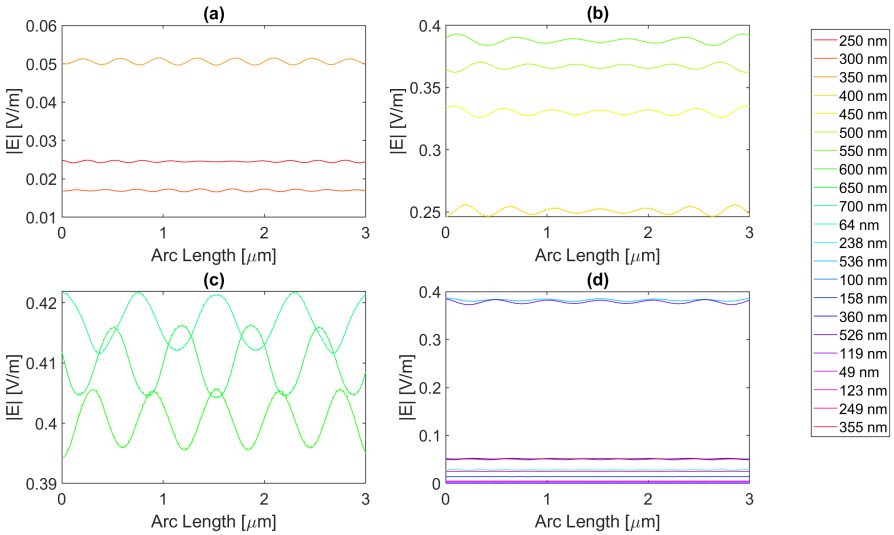

Figure 4.1: Electric field at probe 1 for the stand-alone Si cell.

Figure 4.1 represents the electric field along the length of the probe for the different wavelengths studied. The subfigures divide the wavelength range to distinguish the electric field curves, where (a) corresponds to the wavelengths in the UV spectrum, (b) and (c) represent the Visible spectrum, and (d) corresponds to the resonance wavelengths of the metal present in this structure. The sorting will be the same for the upcoming electric field curves.

The subsequent table results are organized in such a way that for each structure the maximum

electric field and electric field integral are highlighted in bold, and the values that are greater than the stand-alone Si cell values are highlighted in green, for the probe 1 tables.

4.2 Rectangular Nanostructure

In this section are the results for the rectangular structures. Firstly, structures consisting of only one metal were studied, and later with two metals. The figures' shaded areas match the coordinates of the metallic nanoantennas relative to the probes. Thus, the apertures correspond to the unshaded areas.

4.2.1 One-Metal Nanostructure

For rectangular one-metal structures, studies have been carried out for the 20 nm thickness design, shown in figure 3.2a, and the 50 nm thickness design, shown in figure 3.2b, for Silver, Aluminum, Gold and Copper.

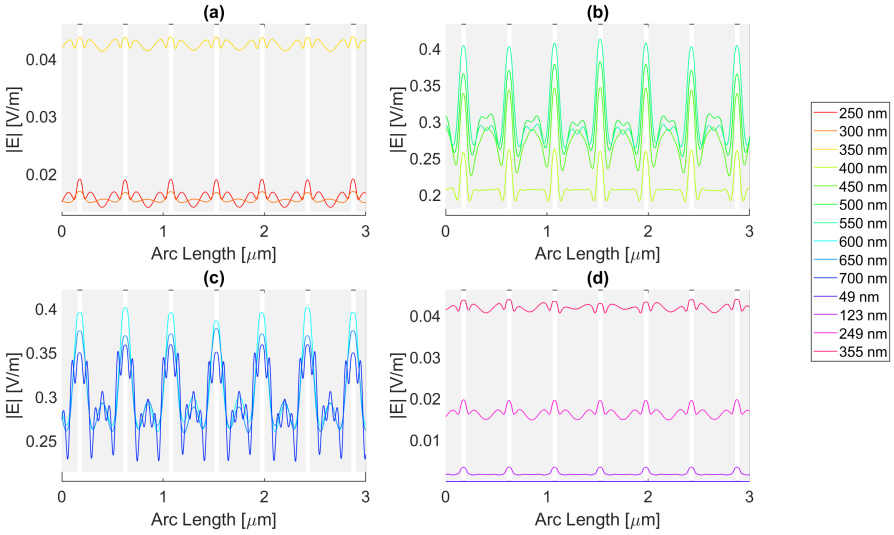

Figure 4.2: Electric Field for Silver 20 nm thick rectangular nanostructure - Probe 1.

For a rectangular nanoantenna with a 20 nm thickness, it is possible to observe that there is field confinement and concentration in the slits, since the incident electric field on the sides of the nanoantenna is reflected into the slit area, thus causing field concentration and confinement effect in this area. Therefore, in probe 1, most curves are a perfect replica of the slit, i.e., the field peaks on the slit and decreases considerably at the end of the slit. However, at certain wavelengths, the metallic antenna does not fully reflect the electric field and may even transmit it. This phenomenon occurs near the resonance wavelengths, giving rise to electric field peaks, in probe 1, where one would expect to have continuously decreasing values, as seen in figures 4.2, 4.3, 4.4, and 4.5.

For Silver, represented in the figure 4.2, the largest peaks are reached for wavelengths between 500 and 650 nm, the largest peak is being reached for a wavelength of 550 nm with a field value of 4.13E-01 V/m. It is therefore still lower than the field obtained for Silicon. Additionally, it should be noted that for an incident field of 700 nm, the electric field presents peaks near the slit boundaries, a pattern that is unique for the frequencies studied, present in figure 4.2 (c), repeating the pattern in the nanoantenna, with smaller values. As for the field integral, at a wavelengths of 600 nm it reaches its maximum equal to 9.29E-07. The results for all frequencies studied can be found in table 4.1 for probe 1, table 4.2 for the second probe, and table 4.3 for probe 3. Comparing the values relative to probe 1, probe 2, and probe 3, the electric field and field integral have all progressively decreased as the distance from the antennas grows, most likely meaning the electric field has been absorbed by the semiconductor.

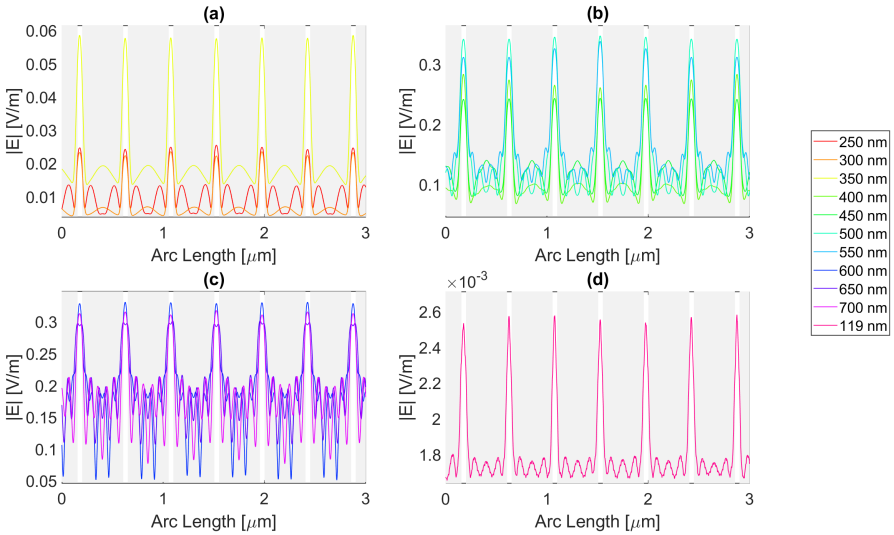

Figure 4.3: Electric Field for Aluminium 20 nm thick rectangular nanostructure - Probe 1.

Aluminium, on the other hand, present in figure 4.3, has its only resonance frequency in the UV spectrum, at 119 nm, and although at this wavelength the absorbed field is small, it is still possible to observe transmission through the antenna. Interestingly, for the larger wavelengths, the electric field norm pattern maintains the maximum values practically constant at the slit, in contrast with the antenna area, which experiences a greater number of peaks, where the maximums are greater and the minimums are lower, i.e., the electric field norm showcases a greater oscillation in values. For this structure, with a thickness of 20 nm, the maximum electric field norm value is 3.47E-01 V/m for a 500 nm incident wavelength, and the maximum integral is 5.97E-07 for a 650 nm wavelength. The results for all frequencies studied can be found in tables 4.4, 4.5, and 4.6 for probe 1, 2, and 3, respectively. From the values in these tables, it is possible to conclude that for a rectangular geometry with 20 nm thickness for the aluminum antenna, the electric field and its integral decrease from the first probe to the second and from the second to the third, conveying the absorption of the electric field by Silicon.

On the other hand, the Gold antenna reaches a maximum electric field of 4.00E-01 V/m and 9.87E-07 of field integral at a 600 nm wavelength, being the design of 20 nm thickness that has a maximum at the largest wavelength, represented in figure 4.4 (c). In figure 4.4 (b), for wavelengths near the resonance wavelength 536 nm, from 450 nm to 700 nm, that the field on the antenna area is transmitted due to Extraordinary Optical Transmission (EOT). The results for all frequencies studied can be found in table 4.7 for probe 1, table 4.8 for probe 2, and table 4.9 for probe 3. As the distance from the slit grows, the electric field and its integral decrease for this Gold nanoantenna, implying the absorption by the semiconductor of the electric field.

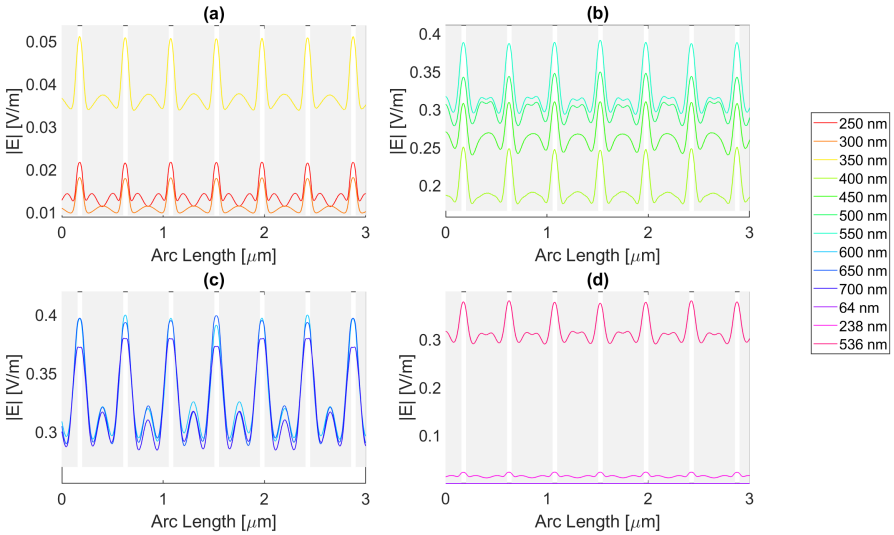

Figure 4.4: Electric Field for Gold 20 nm thick rectangular nanostructure - Probe 1.

Lastly, in the figure 4.5 for the wavelengths between 450 and 700 nm, it can be seen that transmission through the metal occurred and that this increased as the wavelength approaches the resonance at 526 nm. Reaching a maximum field norm of 3.97E-01 at 550 nm, and maximum field integral of 9.33E-07 at 600 nm. It is therefore still lower than the field obtained for Silicon. The results for all frequencies studied can be found in tables 4.10, 4.11, and 4.12 for probe 1, 2, and 3, respectively. Comparing the values relative to probe 1, probe 2, and probe 3, the electric field and field integral have all progressively decreased as the distance from the antennas increases, most likely meaning the electric field has been absorbed by the semiconductor.

Compared with the original considered Silicon cell, for a rectangular nanoantenna with a thickness of 20 nm, there were no improvements in terms of electric field enhancement.

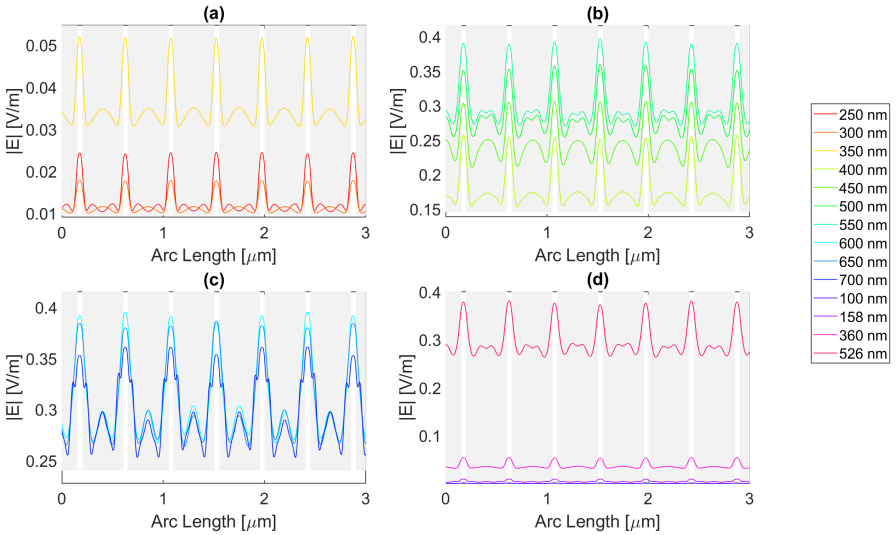

Figure 4.5: Electric Field for Copper 20 nm thick rectangular nanostructure - Probe 1.

Thereafter, for a nanoantenna of 50 nm thickness, the same metals were simulated, yielding figures 4.6,4.7, 4.8, and 4.9. In this case, for Ag and Al the electric field maximum maintained the same wavelength, in contrast with Au and Cu. The generic shape of the radiation pattern remains somewhat similar. The biggest difference is the new maximum values are all greater than the 20 nm values and superior to the original Silicon cell field obtained.

In such circumstances, Ag reaches a maximum electric field, $|E_{max}|$, of 7.22E-01 V/m for a wavelength, λ, of 550 nm, greater than the stand-alone Silicon cell electric field maximum value, $|E_{max}|^{Si}$. However, the integral of the electric field along the probe, $\int E$, 8.16E-07 is smaller than that of the stand-alone Silicon cell, $\int E^{Si}$.

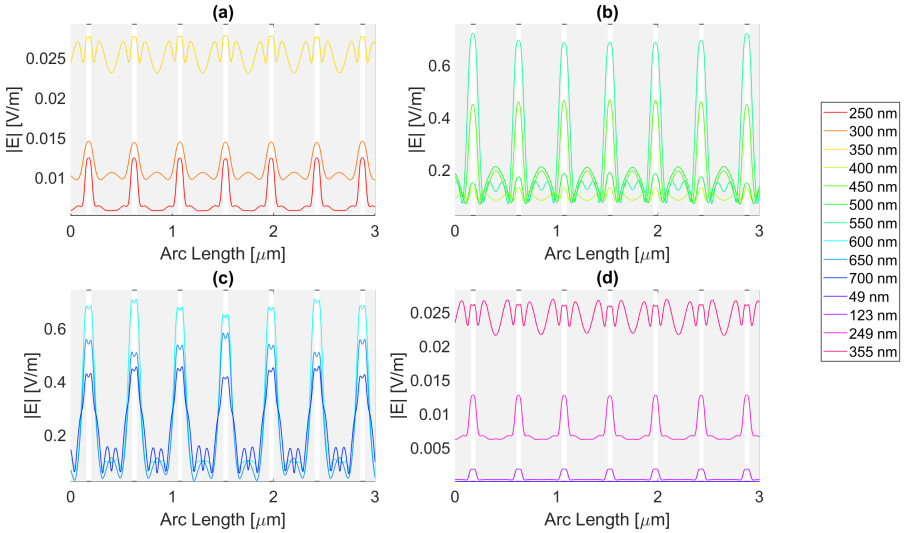

Figure 4.6: Electric Field for Silver 50 nm thick rectangular nanostructure - Probe 1.

Figure 4.6 shows that in (a) in the UV region that the radiation pattern follows the typical pattern for the Shadow zone, except at 350 nm, which again is near the resonance wavelength, and it has an analogous shape to the resonance wavelength, 355 nm, in (d). Whereas, in (c), in the slit there are two peaks in the slit region, and for 700 nm there are also two peaks in the antenna region. The results for all wavelengths studied can be found in tables 4.1, 4.2, and 4.3, for probe 1, 2, and 3, respectively. The electric field intensity norm decreases from probe 1 to 2, and form probe 2 to 3. On the other hand, the field integral for wavelengths from 550 to 650 nm increases from probe 1 to 2, this means that electric field from additional optical paths can propagate into the plane of the probe, not indicating a necessary increase in the peak electric field obtained for that frequency. For the Aluminium antenna, there is an evident greater field concentration in the slit area at 500 nm, in figure 4.7 (b), where the $|E_{max}|$ is 7.95E-01 V/m. However, similarly to Silver, the $\int E$ is lower than $\int E^{Si}$, it is 7.74E-07 at 600 nm. Unlike the 20 nm structure, the peaks in the antenna region start appearing earlier, not as pronounced, at around 500 nm, remaining below 2E-01 V/m. In figure 4.7 (c), the peaks are more pronounced with an approximate value of 3E-01 V/m at 650 nm. The results for all wavelengths studied can be found in tables 4.4, 4.5, and 4.6, for probe 1, 2, and 3, respectively. From probe 1 to 2, and from probe to 2 to 3, both the electric field and integral decrease, as the Silicon absorbs the electric field.

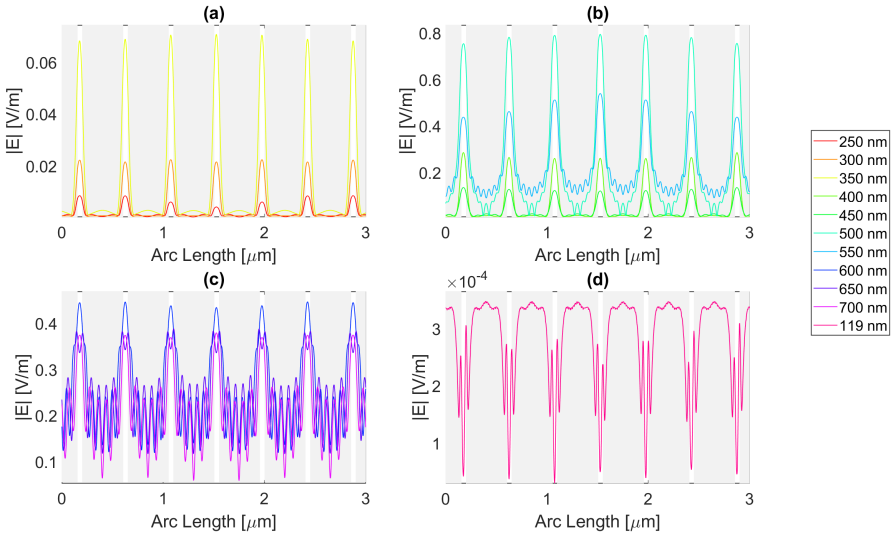

Figure 4.7: Electric Field for Aluminium 50 nm thick rectangular nanostructure - Probe 1.

It is noticeable in figure 4.8 (c), double peaks in the slit that seem to also appear for the Gold nanoantenna, at 650 and 700 nm, similar to Silver, leading to an $|E_{max}|$ of 5.94E-01 V/m at 650 nm, and a maximum $\int E$ of 8.02E-07 at 600 nm. Even though Gold has a resonance at 536 nm and around that wavelength, it is evident that the transmission through the metal is more significant, it is still insufficient to produce a greater electric field or electric field integral in the slit. The results for all wavelengths studied can be found in tables 4.7, 4.8, and 4.9, for probe 1, 2, and 3, respectively. In comparison, probe 2 has

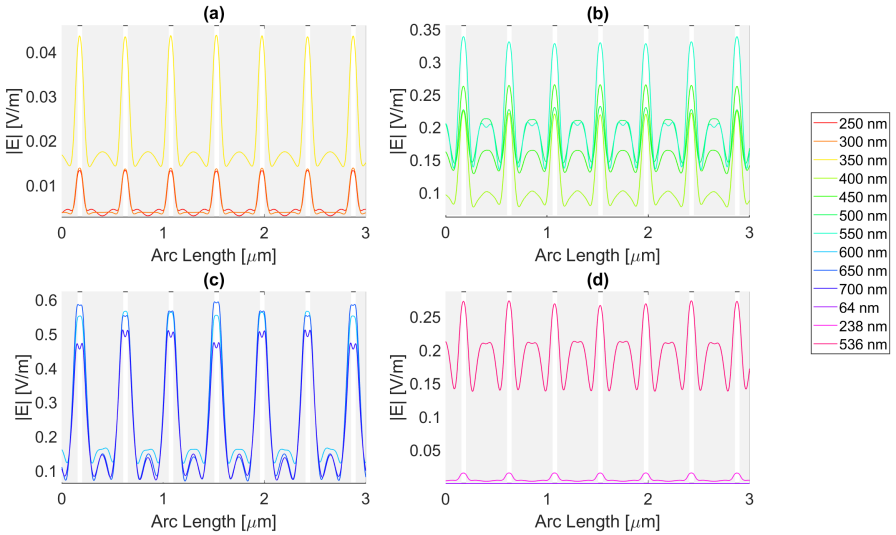

Figure 4.8: Electric Field for Gold 50 nm thick rectangular nanostructure - Probe 1.

smaller values of electric field and integral than probe 1, except for the wavelengths of 650 nm and 700 nm for which the field integral increases, meaning that for the equivalent frequencies the electric field propagates inside the semiconductor through additional optical paths into the probes' plane, and not result in a necessary increase in the maximum electric field. From probe 2 to 3, both the electric field intensity and integral decrease, as the Silicon absorbs the electric field.

Finally, for Copper the $|E_{max}|$ is 6.09E-01 V/m, and the maximum $\int E$ 7.65E-07, at 600 nm. As with Silver and Gold, in figure 4.9, Copper shows two peaks for wavelengths between 600 and 700 nm at the slit. Since the design is thicker, there is more antenna side area, which results in more reflected radiation. More so, for wavelengths near the resonance at 526 nm, the maximum electric field remains

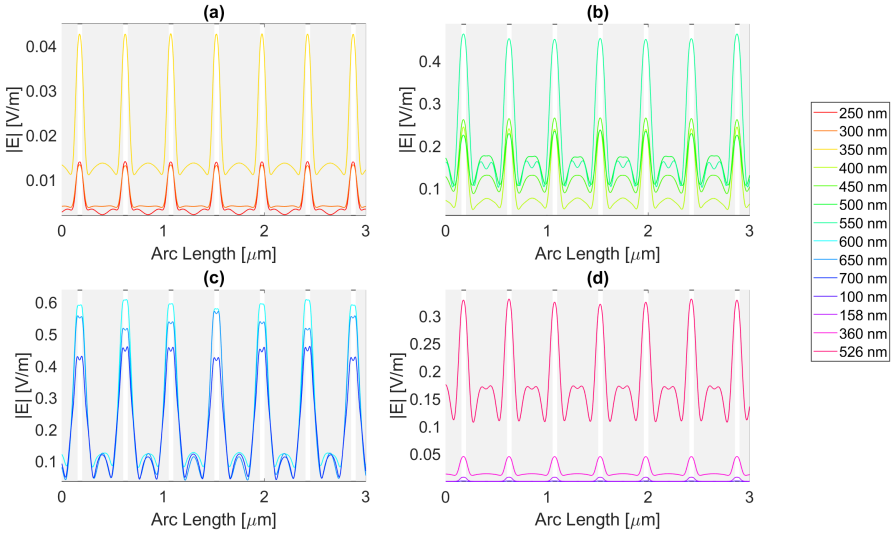

Figure 4.9: Electric Field for Copper 50 nm thick rectangular nanostructure - Probe 1.

relatively unchanged and is even lower in some cases due to the thicker sheet of metal decreasing the transmission through it. The results for all wavelengths studied can be found in tables 4.10, 4.11, and 4.12, for probe 1, 2, and 3, respectively. From probe 1 to 2 both the electric field and integral decrease, except at wavelengths of 600 nm and 650 nm, where the field integral increases. In contrast, from probe 2 to 3 for all wavelengths the electric field intensity and integral both decrease.

In an effort to increase transmission through the metal structures combining two metals were created.

4.2.2 Two-Metal Nanostructure

The two-metal nanostructure follows the design from figure 3.2a, where the two different metal arrays alternate. All possible combinations of the previously characterized metals are created, resulting in six separate structures. Combining Gold and Alumnium results in figure 4.10, where the first shaded area corresponds to Gold, the second to Aluminium, and so on, ending with Aluminium. Comparing figure 4.10, with the previous electric field figures for Gold and Aluminium (4.4 and 4.3), in the antenna region, the electric field roughly maintains the shape it originally had for that metal. The maximum electric field for this structure emerges at 550 nm as 3.393E-01, the maximum field integral comes up at 700 nm as 7.990E-07. While these are not improvements comparing to the one-metal gold antenna, they are improvements for aluminium antena. The results for the full wavelength range can be found in table B.2.

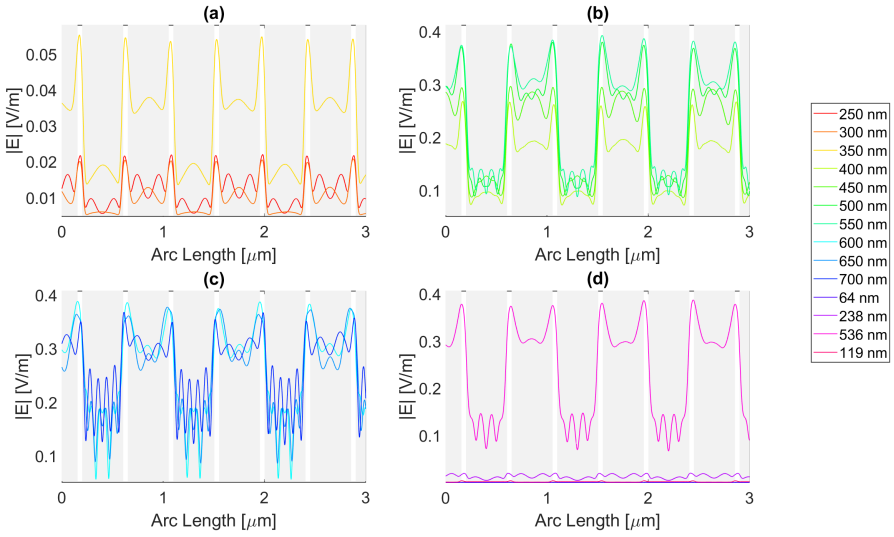

Figure 4.10: Electric Field for Gold and Aluminium 20 nm thick rectangular nanostructures - Probe 1.

Substituting the Aluminium for Copper gives origin to a Gold and Copper structure that follows the same sequence as the previous one, which results in the electric field curves in figure 4.11. If we compare figure 4.11, with figures 4.4 and 4.5, it is barely noticeable any difference between the threee figures in terms of shape and in terms of values as well. Due to the fact that the two metals have close

resonances meaning both metals transmit in the same wavelengths. This structure reaches an electric field maximum and integral at 600 nm of 3.99E-01 V/m and 9.606E-07, respectively. The wavelength complete range results can be found in table B.3.

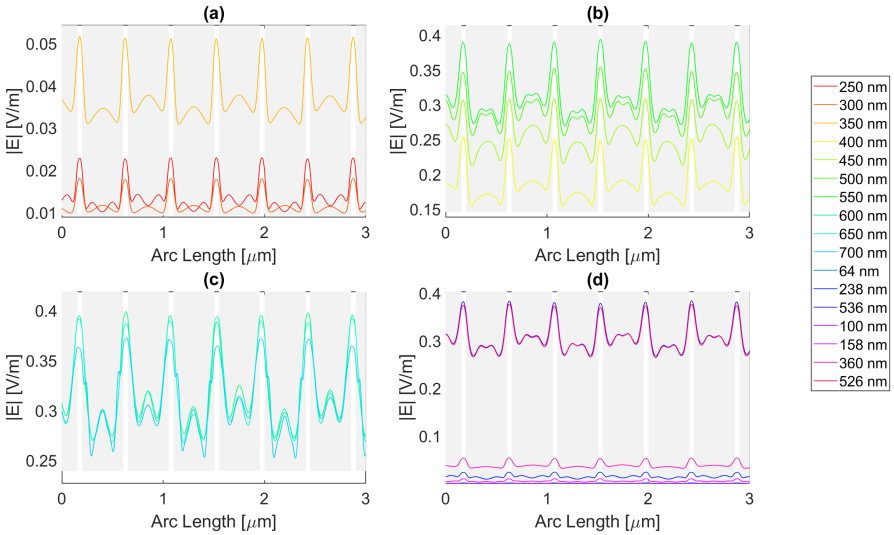

Figure 4.11: Electric Field for Gold and Copper 20 nm thick rectangular nanostructures - Probe 1.

Replacing the Copper for Silver originates a Gold and Silver structure that follows the same sequence as the previous one, which results in the electric field curves in figure 4.15. Once again, the shape of the electric field remains similar in each metal to the original one-metal array, for example, at 700 nm, under the antenna region, there are once again visible peaks for Silver, comparing with figure 4.2. Whereas for gold, under the antenna region, there is only one peak at 700 nm, just as in figure 4.3. This structure yields a maximum electric field of 4.03E-01 V/m at 600 nm, and a maximum field integral of 9.588E-07. The results for the set of wavelengths tested can be found in B.4.

This next design combines Copper and Silver, resulting in the electric field curves illustrated in figure 4.12, where the first shaded area corresponds to Copper, the second to Silver, and so on, ending with Silver. As seen in figure 4.12, for regions underneath the Silver array, the radiation pattern follows the same shape as the one-metal Silver structure present in figure 4.2. For the Copper array, the same is verified, where the original electric field curves are in figure 4.5. The maximum electric field achieved is 4.05E-01 V/m at 550 nm, which is an improvement for Copper but not for Silver. The most significant field integral reached is 9.310E-07 at 600 nm, which is an improvement for Silver but not for Copper. The results for all wavelengths studied can be found in table B.5.

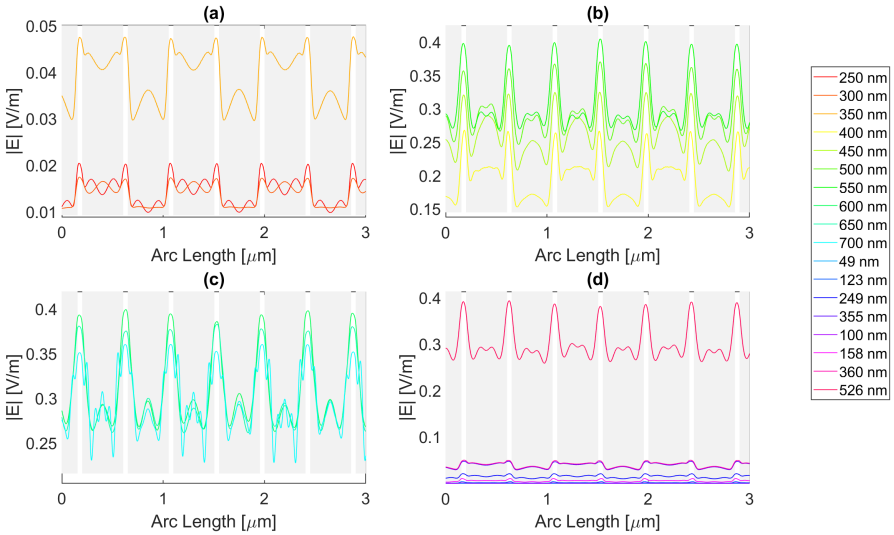

Figure 4.12: Electric Field for Copper and Silver 20 nm thick rectangular nanostructures - Probe 1.

Trading Copper for Aluminium originates an Aluminium and Silver structure that follows the same sequence as the previous one, which results in the electric field curves in figure 4.13. The $|E_{max}|$ is 4.06E-01 achieved at 500 nm, and the maximum $\int E$ is 7.628E-07. These values are an improvement for Aluminium since they are superior to its equivalent one-metal antenna. On the other hand, these values are diminished for Silver when compared with its one-metal counterpart.

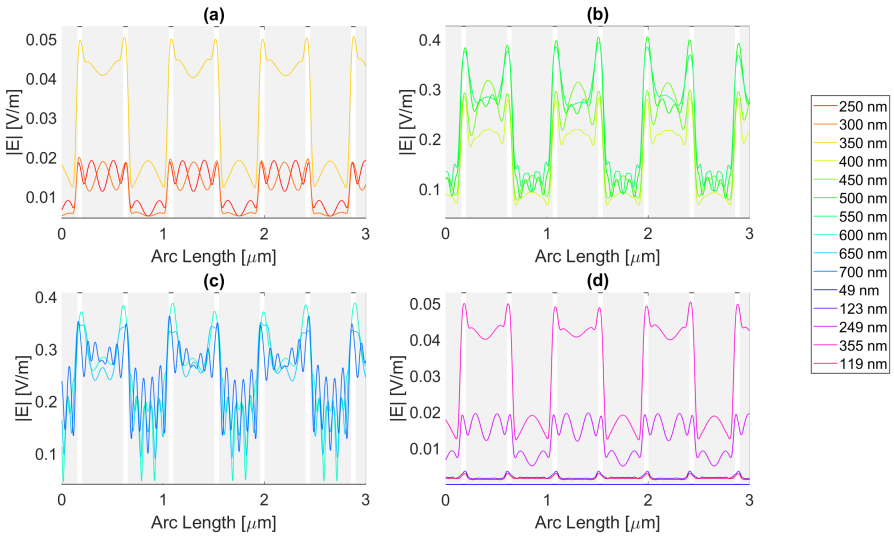

Figure 4.13: Electric Field for Aluminium and Silver 20 nm thick rectangular nanostructures - Probe 1.

Replacing Silver with Copper, an Aluminium and Copper design is developed, yielding electric fields for the various frequencies as seen in figure 4.14. This structure reaches a maximum electric field of 3.87E-01 V/m at 550 nm and a maximum electric field integral of 7.595E-01 at 600 nm. These an improvement for Aluminium, compared with the on-metal but not for Copper. The main difference might

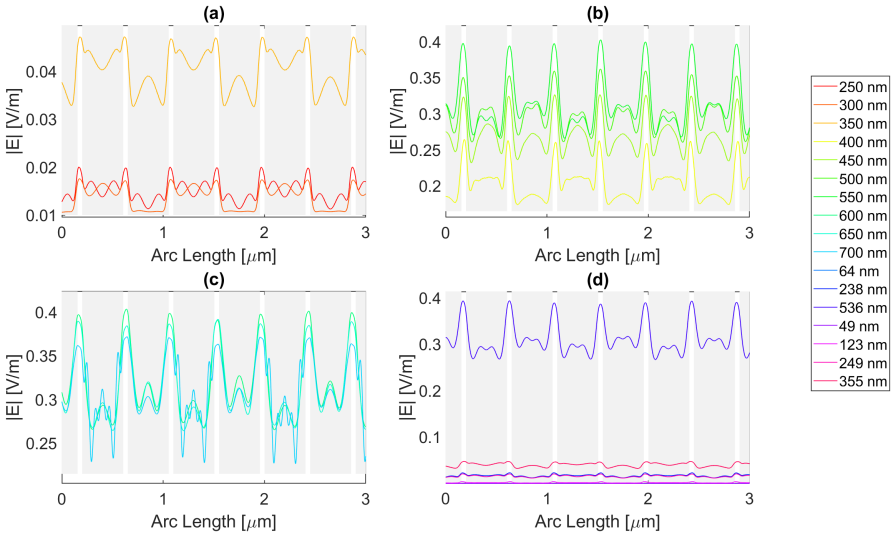

Figure 4.15: Electric Field for Gold and Silver 20 nm thick rectangular nanostructures - Probe 1.

be due to the fact that at the Copper resonance wavelength of 526 nm, in figure 4.14 (d), while the Copper array transmits relatively high electric field the Aluminium array does not, since it does not a have resonance near that wavelength, resulting in overall less transmitted field, when compared with the one-metal Copper antenna.

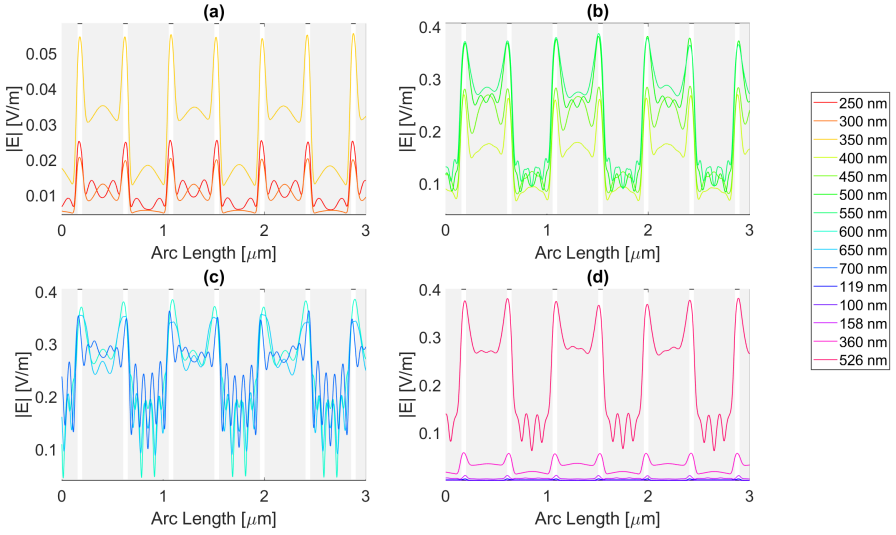

Figure 4.14: Electric Field for Aluminium and Copper 20 nm thick rectangular nanostructures - Probe 1.

Since this type of structure did not introduce a clear improvement over the electric field value of the original Silicon cell, it is necessary to study other types of geometries that can introduce improvements in field concentration, such as a circular or triangular geometry.

4.3 Circular Nanostructure

The circular design is introduced in order to try to improve both the electric field concentration and also the value of the field integral. The type of simulated structures are present in figure 3.2c and 3.2d. The slit consists of the outline of two consecutive circles, resembling a triangular shape with rounded sides. This arrangement may lead to more field reflection from the side of the antennas since the circles are only tangent to the semiconductor, in contrast to the rectangular antennas, which were entirely in contact with the top of the semiconductor.

Starting by the antenna with a 100 nm radius, it is evident that for certain frequencies the electric field present in the Silicon perfectly replicates the aperture described above, just as in the figure 4.16 for a wavelength of 123 nm, although there is a small electric field, at this wavelength, it perfectly illustrates the shadow zone because the triangular shape with rounded sides is evident. The other frequencies generally have a similar pattern. Besides, in the visible zone, the slits interfere with each other's field, sometimes creating "shadows" where the field has local minimums whereas at other wavelengths it has maximums, for example, the 600 nm vs. 300 nm curve. In fact, for the visible wavelengths 4.16 (b) and (c) the electric field maximum peaks are achieved under the antennas, while for UV it is in the slit region, (c) and (d).

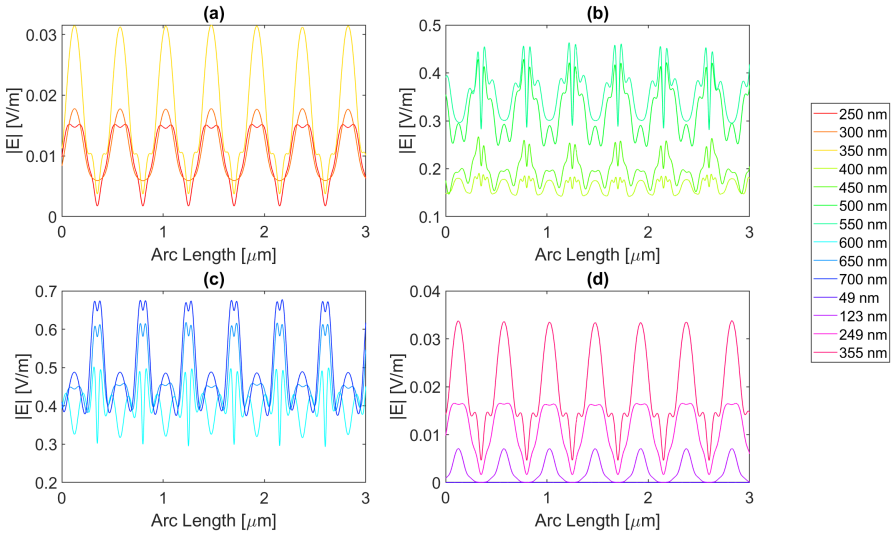

Figure 4.16: Electric Field for the Silver circular nanostructure with 100 nm radius - Probe 1.

In addition, the electric field intensity at the second probe can be found in the Appendix A in figure A.9. In the figure it is evident that some of the electric field was already absorbed by the Silicon, since the values decreased. Additionally, there is less of an interference pattern. In the third probe, figure A.9, it is apparent that for the wavelengths between 400 nm and 600 nm most of the field has been absorbed, and in this region, where there is still electric field present, in the visible wavelengths, its pattern is in line with

the pattern for Fraunhofer zone illustrated in figure 2.14. This type of pattern behaviour for this structure is common to all the metals, despite happening at sightly different wavelengths. For the circular antenna with 100 nm radius the maximum electric field achieved for Silver is 6.77E-01 V/m, with an integral of the field 1.48E-06 at 700 nm. Both of these are greater than the values for the Silicon cell without a nanostructure. The results for all frequencies studied can be found in table 4.1 for probe 1, table 4.2 for the second probe, and table 4.3 for probe 3. From probe 1 to probe 2, there is an increase in the electric field intensity for 600 nm and 650 nm wavelengths and a decrease in its integral. From probe 2 to probe 3, there is an increase in the electric field intensity at 700 nm wavelength reaching a value as high as 6.82E-01 V/m, even higher than in probe 1, while it decreases for the remaining wavelengths. This might indicate that this geometry and material are capable of inducing a long-distance field concentration on the Silicon.

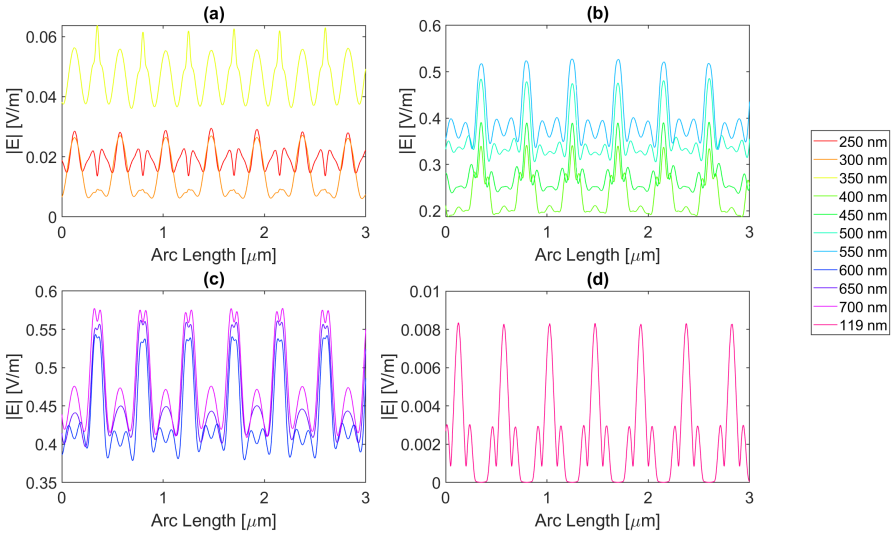

Figure 4.17: Electric Field for the Aluminium circular nanostructure with 100 nm radius - Probe 1.

In the case o The figure 4.17 represents the electric field intensity along probe 1 for Aluminium. The highest electric field attained is 5.78E-01 V/m and an integral of 1.43E-06 at 700 nm, representing an improvement from the basic cell. The results of the studied wavelengths can be found in tables 4.4, 4.5, and 4.6 for probes 1, 2, and 3, respectively. From probes 1 to 2, for wavelengths between 600 nm and 700 nm the electric field intensity increases, and it keeps increasing for 700 nm in probe 3, reaching 6.18E-01 V/m in the third probe. As for the electric field integral, it decreases from probe to probe. f Gold, where the electric field intensity is illustrated in figure 4.18, the best electric field achieved is 6.17E-01 V/m at 700 nm with a field integral of 1.42E-06, once again showing improvement in terms of both quantities. For the studied wavelengths, the results studied can be found in table 4.7 for probe 1, table 4.8 for probe 2, and table 4.9 for probe 3. From probes 1 to 2, the electric field intensity increases for wavelengths between 500 nm and 650 nm, while the field integral decreases. Whereas, from probes

2 to 3, both quantities decrease except for a wavelength of 700 nm the intensity increases reaching 6.45E-01 V/m.

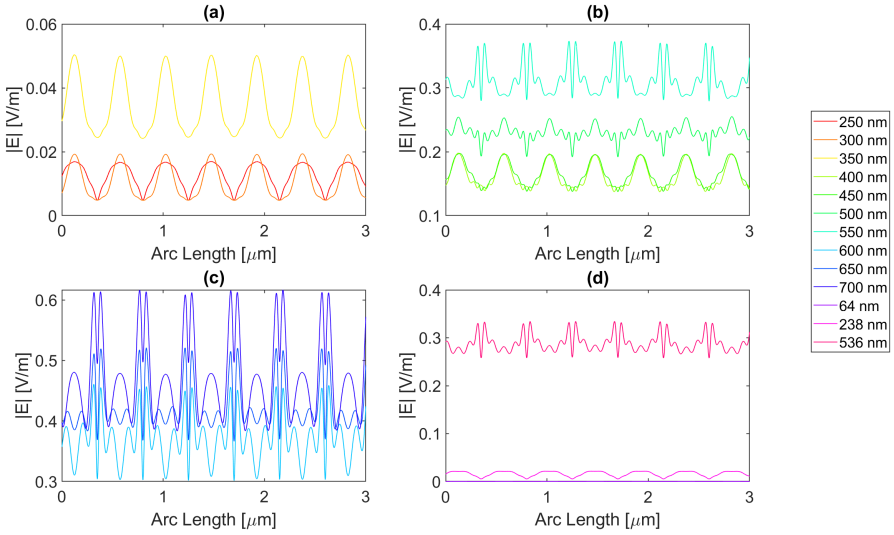

Figure 4.18: Electric Field for the Gold circular nanostructure with 100 nm radius - Probe 1.

Lastly, Copper yields an electric field curve illustrated in figure 4.19, achieving an intensity as high as 6.49E-01 V/m and integral of 1.45E-06 at 700 nm, making it the second highest intensity reached with the circular structure with 100 nm radius. For the studied wavelengths, the results studied can be found in table 4.10 for probe 1, table 4.11 for probe 2, and table 4.12 for probe 3. The electric field intensity increases for wavelengths ranging from 500 nm to 650 nm, from probe 1 to 2, while the integral decreases. At 700 nm from probe 2 to 3 the intensity increases, yet for the remaining wavelengths, it decreases and so does the integral.

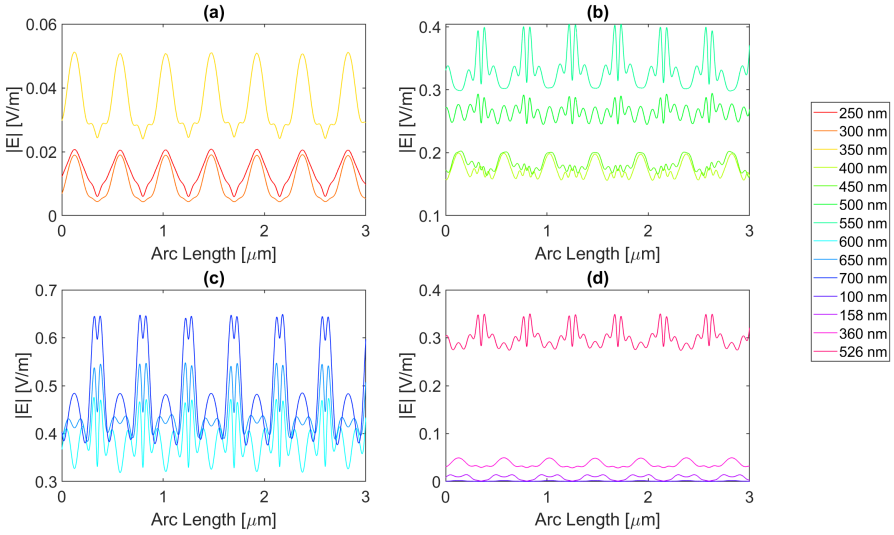

Figure 4.19: Electric Field for the Copper circular nanostructure with 100 nm radius - Probe 1.

Now, moving on to the circular nanoantenna with a 200 nm radius, the electric field intensity characteristics at probe 1 is in figures 4.20, 4.23, 4.21 and 4.22. Even though the radius increased, the displacement between the center of the circles is maintained, which leads to an overall smaller aperture. For this structure, the all metals showed improvements for electric field intensity over the simple Silicon cell. For Silver, the maximum electric field strength achieved is about 5.78E-01 V/m for a wavelength of 700 nm, with a field integral of 1.40E-06, the highest value achieved for this geometry. The results of the studied wavelengths can be found in tables 4.1, 4.2, and 4.3 for probes 1, 2, and 3, respectively. The electric field intensity increases from probe 1 to probe 2 for particular wavelengths, such as 500 nm, 600 nm, and 700 nm, despite the field integral decreasing for all wavelengths. As for probe 3, both the electric field intensity and integral have decreased, alluding to the absorption of the electric field by the semiconductor material.

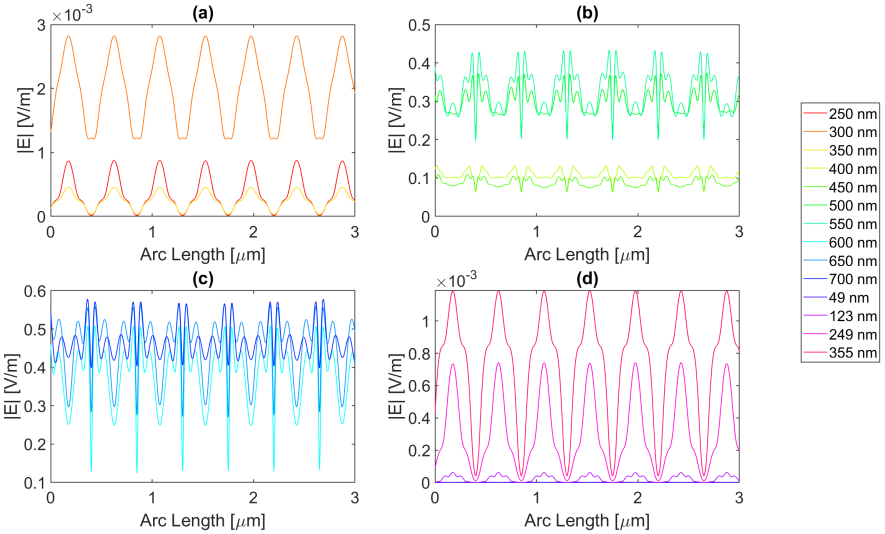

Figure 4.20: Electric Field for the Silver circular nanostructure with 200 nm radius - Probe 1.

Now for Gold, the highest field attained is approximately 5.46E-01 V/m, with a 1.29E-06 integral, for a wavelength of 700nm. The results of the studied wavelengths can be found in tables 4.7, 4.8, and 4.9 for probes 1, 2, and 3, respectively. For the range of wavelengths between 500 nm and 650 nm the electric field intensity increases from probe 1 to probe 2, yet the field integral always decreases. At 700 nm the intensity also increases for the third probe, while the integral decreases for all wavelengths.

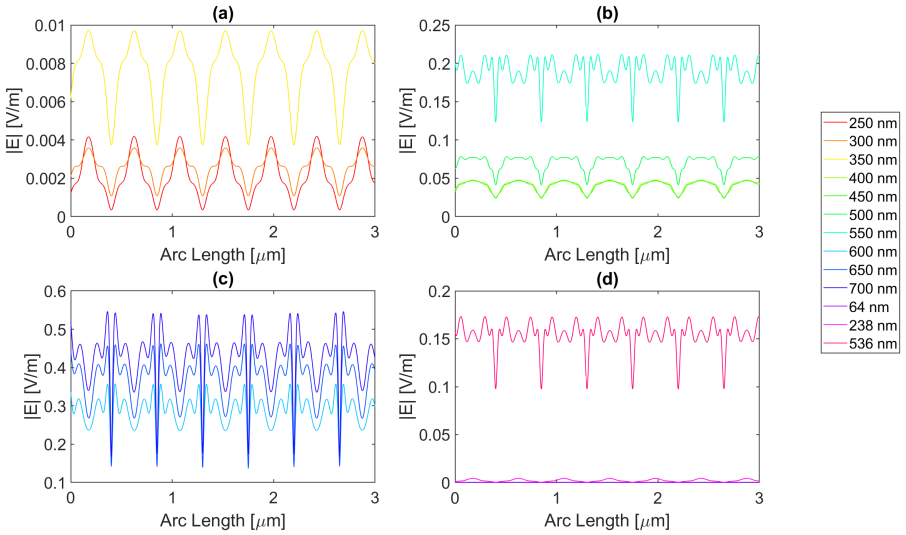

Figure 4.21: Electric Field for the Gold circular nanostructure with 200 nm radius - Probe 1.

For Copper, the electric field peak is similar to Gold, even happening at the same wavelength, it is 5.45E-01 V/m, with a 1.33E-06 integral. The results of the studied wavelengths can be found in tables 4.10, 4.11, and 4.12 for probes 1, 2, and 3, respectively. For the range of wavelengths between 500 nm and 700 nm the electric field intensity increases from probe 1 to probe 2, however the field integral always decreases. In the third probe at 700 nm, the intensity also increases, while the integral decreases for all wavelengths.

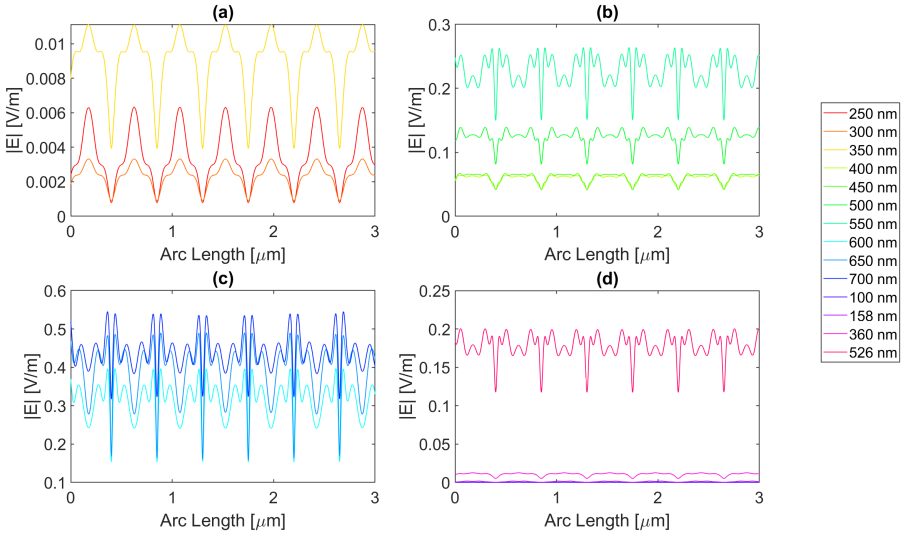

Figure 4.22: Electric Field for the Copper circular nanostructure with 200 nm radius - Probe 1.

Even though Aluminium does show an improvement in the maximum electric field, being 4.49E-01 V/m, the integral does not, as it falls just under the basic Si cell with a value of 1.20E-06, for a 600 nm wavelength. The results of the studied wavelengths can be found in tables 4.4, 4.5, and 4.6 for probes

1, 2, and 3, respectively. For the range of wavelengths between 550 nm and 700 nm the electric field intensity increases from probe 1 to probe 2, contrary to the field integral which always decreases. At 700 nm the intensity also increases for the third probe, while the integral decreases for all wavelengths.

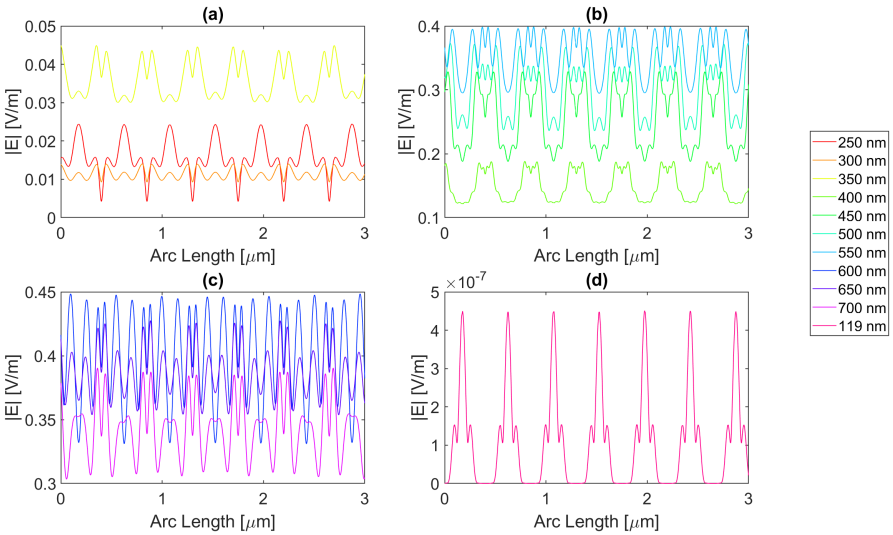

Figure 4.23: Electric Field for the Aluminium circular nanostructure with 200 nm radius - Probe 1.

4.4 Triangular Nanostructure

In this section, the triangular design is introduced, the simulated structures are present in figures 3.2e and 3.2f. Starting with the triangular structure with a base of 100 nm all the distinct metal structures offer an enhancement of electric field values, but none in terms of the field integral. This might be due to the aperture trapezoidal shape, where the smaller base of 250 nm is the top of the semiconductor, and its legs are the contour of the triangular antennas, resulting in the reflection of the electric field into the air instead of the semiconductor. For the 200 nm base structure, the smaller base of the trapezoid is instead 50 nm wide, that is, the slit. In the Silver triangular antenna with a base of 100 nm, with an electric field intensity pattern as seen in figure 4.16, the peak electric field intensity is 4.71E-01 V/m with an integral of 1.09E-06 at 700 nm. The results of the studied wavelengths can be found in tables 4.1, 4.2, and 4.3 for probes 1, 2, and 3, respectively. The electric field intensity increases from probe 1 to probe 2 for a range of wavelengths, from 550 nm to 700 nm, despite the field integral decreasing for all wavelengths. As for probe 3, both the electric field intensity and integral have decreased, indicating the absorption of the electric field by the semiconductor material.

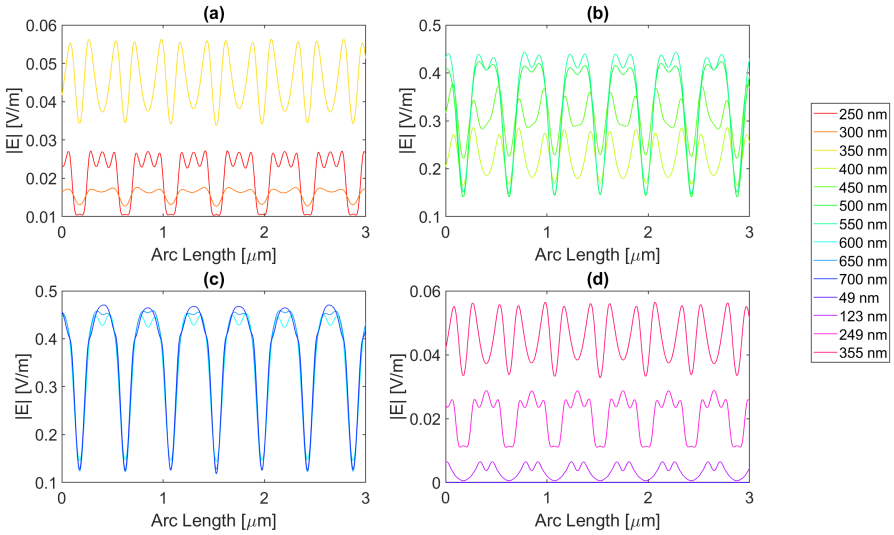

Figure 4.24: Electric Field for the Silver triangular nanostructure with 100 nm base - Probe 1.

As for Aluminium, illustrated in figure 4.17, the achieved field is higher, but the integral is lower, with values of 5.08E-01 V/m at 650 nm and 9.14E-07 at 700 nm, respectively. The results of the studied wavelengths can be found in tables 4.4, 4.5, and 4.6 for probes 1, 2, and 3, respectively. The electric field intensity increases from probe 1 to probe 2 for a range of wavelengths, from 500 nm to 700 nm, despite the field integral decreasing for all wavelengths. As for probe 3, both the electric field intensity and integral have decreased, indicating the absorption of the electric field by the semiconductor material.

Gold and Copper, with electric field intensity curves as seen in figures 4.18 and 4.19, present with

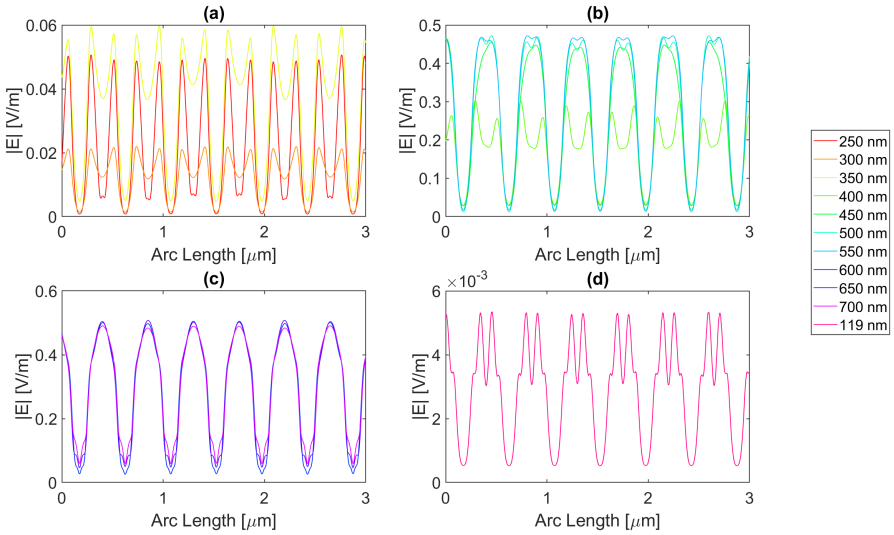

Figure 4.25: Electric Field for the Aluminium triangular nanostructure with 100 nm base - Probe 1.

similar maximum values with 4.58E-01 V/m and 4.66E-01 V/m electric field intensities and 1.11E-06 1.09E-06 field integrals, for Gold and Copper, respectively, at a 700 nm wavelength. The results, for gold, of the studied wavelengths can be found in tables 4.7, 4.8, and 4.9 for probes 1, 2, and 3, respectively.

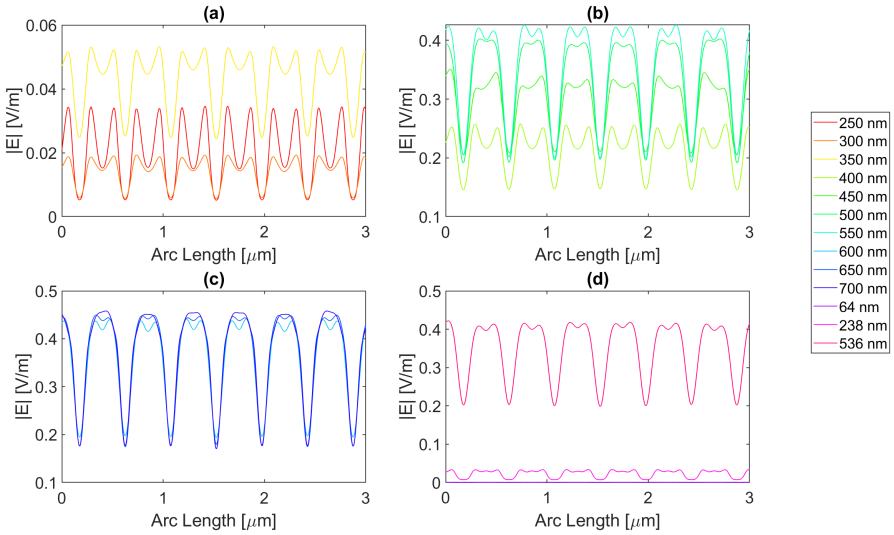

Figure 4.26: Electric Field for the Gold triangular nanostructure with 100 nm base - Probe 1.

The electric field intensity increases from probe 1 to probe 2 for a range of wavelengths, from 550 nm to 700 nm, despite the field integral decreasing for all wavelengths. As for probe 3, both the electric field intensity and integral have decreased, implying the absorption of the electric field by the semiconductor material. While for Copper, the results for the studied wavelengths are in tables 4.10, 4.11, and 4.12 for probes 1, 2, and 3, respectively. The electric field intensity increases from probe 1 to probe 2 for a range of wavelengths, from 550 nm to 700 nm, yet the field integral decreasing for all wavelengths. As

for probe 3, both the electric field intensity and integral have decreased, implying the absorption of the electric field by the semiconductor material.

In conclusion, for the triangular geometry of the 100 nm base, there was an enhancement in terms of the electric field, for all the distinct metals, as they all had wavelengths for which the electric field intensity was higher than that of the Silicon basic cell. In contrast, in terms of field integral, there was no improvement, as none of the different metal nanoantennas provided a larger field integral than the Si original cell, this might mean that, for the triangular geometry of 100 nm base, there are points of electric field concentration, since higher values of electric field intensity are achieved, but this does not necessarily reflect a higher total electric field in the semiconductor.

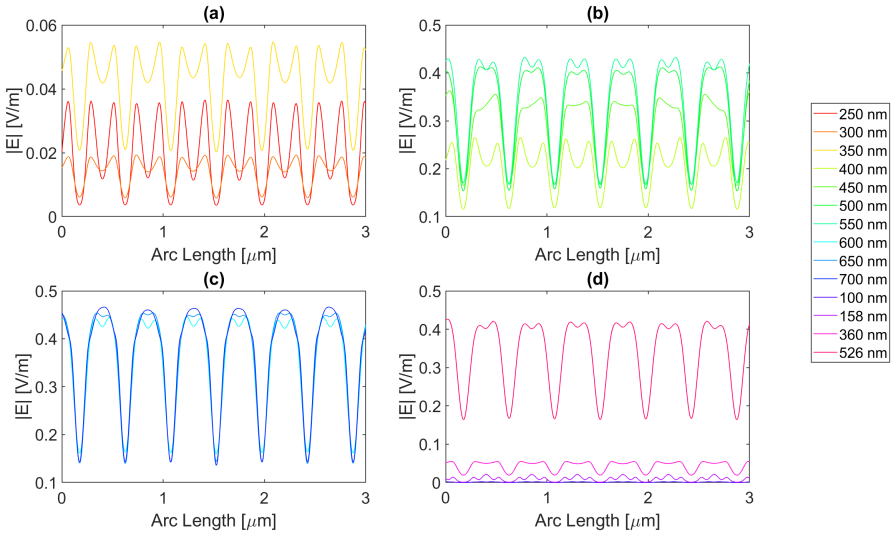

Figure 4.27: Electric Field for the Copper triangular nanostructure with 100 nm base - Probe 1.

As for the simulations with the triangle base of 200 nm, there was electric field enhancement relative to the cell without nanoantennas, for all metals, despite having no enhancement for the field integral. The simulated silver nanoantenna yields the electric field intensity curve seen in figure 4.20. It has the maximum for a 500 nm wavelength of 5.551E-01 V/m, with a field integral of 8.86E-07.The results of the studied wavelengths can be found in tables 4.1, 4.2, and 4.3 for probes 1, 2, and 3, respectively. The electric field intensity increases from probe 1 to probe 2 for a range of wavelengths, from 650 nm to 700 nm, and the field integral increases for wavelengths between 600 nm and 700 nm. As for probe 3, both the electric field intensity and integral have decreased, indicating the absorption of the electric field by the semiconductor material.

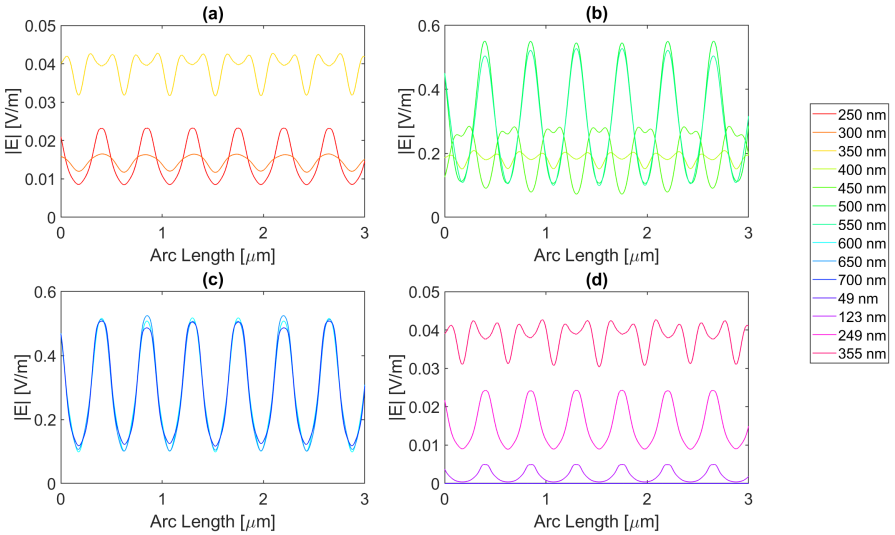

Figure 4.28: Electric Field for the Silver triangular nanostructure with 200 nm base - Probe 1.

Figure 4.23 shows the electric field along probe 1 for the Aluminium antenna, for the distinct wavelengths, it shows that the maximum electric field is 6.36E-01 V/m at 500 nm, with an integral of 5.78E-07. The results of the studied wavelengths can be found in tables 4.4, 4.5, and 4.6 for probes 1, 2, and 3, respectively. The electric field intensity decreases from probe 1 to probe 2 for the whole range of wavelengths. As for the field integral, it increases for wavelengths between 500 nm and 700 nm. In probe 3, both the electric field intensity and integral have decreased, indicating the absorption of the electric field by the semiconductor material.

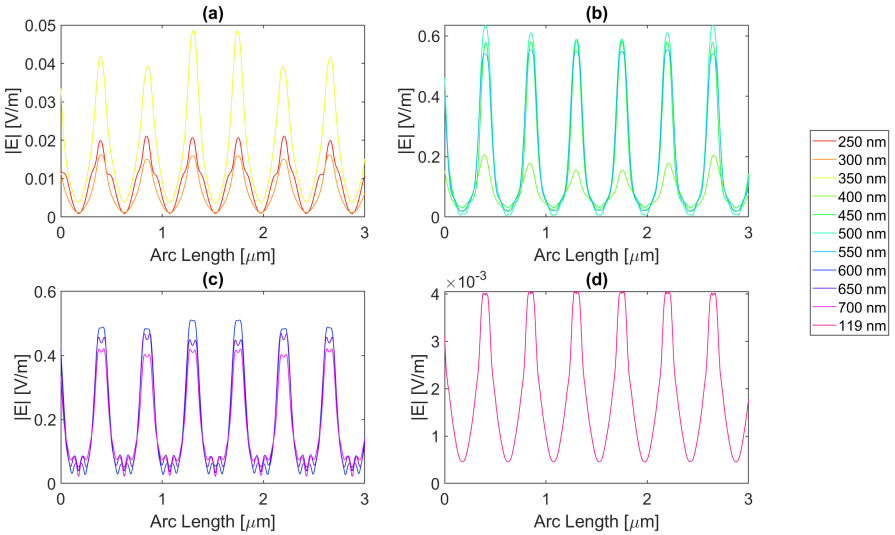

Figure 4.29: Electric Field for the Aluminium triangular nanostructure with 200 nm base - Probe 1.

Regarding figure 4.21 it is evident that the maximum electric field happens for a wavelength of 650 nm, and is, roughly, 5.02E-01 V/m. However, the highest field integral obtained is 9.20E-07 for 600 nm.

The results of the studied wavelengths can be found in tables 4.7, 4.8, and 4.9 for probes 1, 2, and 3, respectively. The electric field intensity increases from probe 1 to probe 2 for the wavelengths between 600 nm and 700 nm. As for the field integral, it increases for wavelengths between 500 nm and 700 nm. In probe 3, both the electric field intensity and integral have decreased, indicating the absorption of the electric field by the semiconductor material.

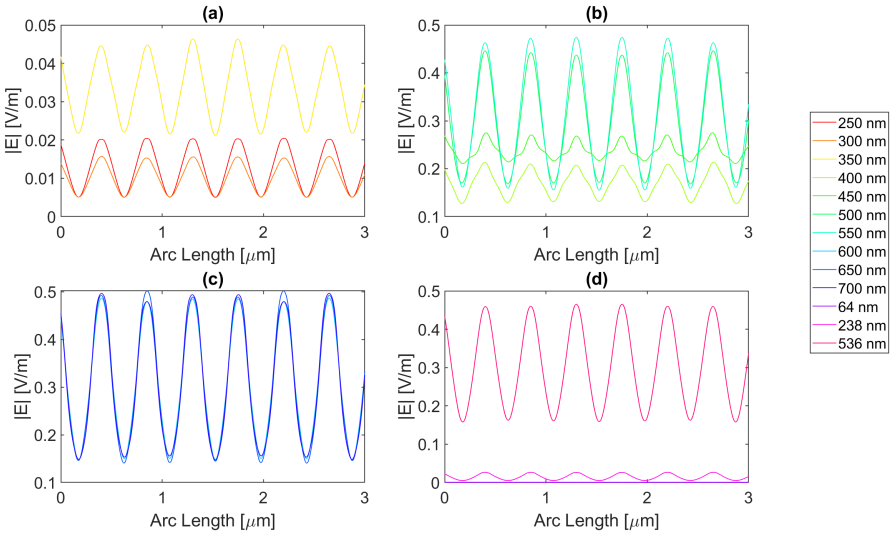

Figure 4.30: Electric Field for the Gold triangular nanostructure with 200 nm base - Probe 1.

Lastly, figure 4.22 illustrates the electric field at the first probe for Copper, which peaks at 5.12E-01 V/m for a wavelength of 650 nm. Whereas, the field integral peaks at 8.72E-07 for a 700 nm wavelength. The results of the studied wavelengths can be found in tables 4.10, 4.11, and 4.12 for probes 1, 2, and 3, respectively. The electric field intensity increases from probe 1 to probe 2 for the wavelengths between 600 nm and 700 nm. As for the field integral, it decreases for all wavelengths. In probe 3, both the electric field intensity and integral have decreased, indicating the absorption of the electric field by the semiconductor material.

While this geometry yielded no improvements for the field integral, there were improvements in the electric field intensity for all combinations, meaning while this structure enhances and concentrates the electric field intensity in certain points, it does not mean it gives rise to a higher total field in the semiconductor.

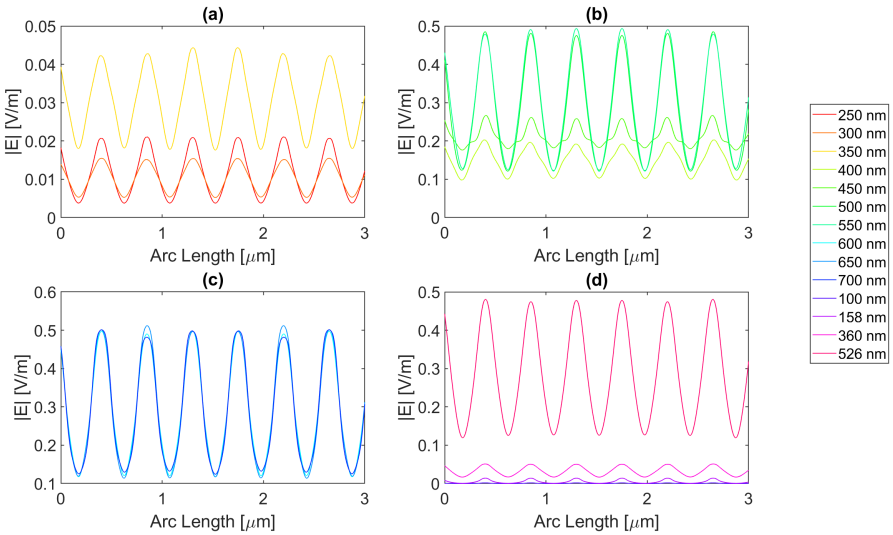

Figure 4.31: Electric Field for the Copper triangular nanostructure with 200 nm base - Probe 1.

4.5 Results Discussion

From the sections above, key findings emerge, for instance in table 4.1, Silver achieves the greatest $|E_{max}|$, 7.22E-01 V/m, at 550 nm for the rectangular structure of 50 nm thickness. Additionally, the highest $\int E$ obtained is 1.48E-06 for a circular structure with a 100 nm radius for a 700 nm wavelength. Overall, the Silver structures in tandem with the Silicon cell yield an electric field intensity greater than that of the Silicon cell alone 24 times.

The table 4.4 contains the results for Aluminium. The highest $|E_{max}|$ achieved is 7.95E-01 V/m for the rectangular structure of 50 nm thickness at 500 nm. Also, it reaches its largest $\int E$ value, 1.43E-06, for the circular structure with a 100 nm radius for 700 nm wavelength. Combining the results for all the Aluminium antennas, the Silicon cell electric field intensity is surpassed a total of 21 times for this metal.

Concerning table 4.7 which illustrates the results for Gold, the antenna design that yields the greatest $|E_{max}|$ and $\int E$ is the circular antenna with a 100 nm radius at 700 nm, with an electric field of 6.17E-01 V/m and an $\int E$ of 1.42E-06 at 700 nm. Now, compiling the results for the gold antenna structures the electric field intensity is greater than the Silicon cell peak field intensity a total of 19 times.

Lastly, the antenna design giving rise to the highest values for Copper, consulting table 4.10, is the circular antenna with a 100 nm radius at a 700 nm wavelength with an electric field of 6.49E-01 V/m and an $\int E$ of 1.45E-06 at 700 nm. Analysing the table results one can observe that the electric field intensity surpasses the $|E_{max}|^{Si}$ 20 times. It can be concluded that the highest field concentration is for Aluminum with a field value of 7.95E-01 V/m at 500 nm. As for the electric field integral the highest value is reached for the Silver circular antenna with 100 nm radius.

For the rectangular nanoantenna, a higher field concentration is obtained for the 50 nm thick metal due to the fact that the added thickness facilitates the reflection of the electric field in the sides of the nanoantenna, compared with the 20 nm thickness. Thus, resulting in a higher concentration of the electric field in the slit area.

Now analyzing from a geometry standpoint, the 20 nm thick rectangular antenna has the best result when using Silver with an electric field of 4.13E-01 V/m at 550 nm, yet is not an improvement compared with $|E_{max}|^{Si}$. In contrast, the 50 nm thick rectangular antenna has field enhancement for all the metals simulated, reaching its highest electric field of 7.95E-01 for Aluminium at 500 nm.

The circular geometry shows the electric field maxima for the same metal for both studied radii and the same wavelength. That is, for Silver at 700 nm the maximum electric field reached is 6.77E-01 V/m and 5.78E-01 V/m for the 100 nm and 200 nm radius, respectively.

Finally, the triangular geometry delivers the electric field maxima for the different base lengths for the same metal, Aluminium, but at distinct wavelengths. With a base length of 100 nm, the peak field is 5.08E-01 V/m at 700nm. As for the 200 nm base, at 500 nm the maximum field achieved is 6.36E-01 V/m. Notably, in a similar way to the circular geometry, the triangular geometries simulated all provide

improvements for all considered metals for at least one of the frequencies when compared to $|E_{max}|^{Si}$. The two-metal rectangular geometry resulted in no improvements, as well as the on-metal rectangular 20 nm thick antenna. As for the triangular antenna it enhanced the electric field intensity for all the combinations, yet the electric field integral never showed improvements, while this structure enhances and concentrates the electric field intensity in certain points, it does not mean it gives rise to a higher total field in the semiconductor.

It should also be noted that the geometry and metal used for the antenna not only influenced the electric field and its integral but also influenced the wavelengths for which it occurs. For example, for the 100 nm radius circular antenna, the maximum electric field intensity and integral all occurred for the same wavelength, at 700 nm, independently of the nanoantenna's metal.

Table 4.1: Summary table of the results obtained for the Silver nanostructures - Probe 1.

		Rectangle thickness = 20 nm		Rectangle thickness = 50 nm		Circle r100		Circle r200		Triangle base = 100 nm		Triangle base = 200 nm	
	λ [nm]	$\|E_{max}\|$ [V/m]	$\int E$	$\|E_{max}\|$ [V/m]	$\int E$	$\|E_{max}\|$ [V/m]	$\int E$	$\|E_{max}\|$ [V/m]	$\int E$	$\|E_{max}\|$ [V/m]	$\int E$	$\|E_{max}\|$ [V/m]	$\int E$
UV	250	1.92E-02	4.86E-08	1.25E-02	2.18E-08	1.52E-02	3.18E-08	8.76E-04	1.10E-09	2.72E-02	6.13E-08	2.32E-02	4.38E-08
	300	1.70E-02	4.68E-08	1.46E-02	3.35E-08	1.78E-02	3.27E-08	2.82E-03	6.02E-09	1.76E-02	4.78E-08	1.65E-02	4.34E-08
	350	4.39E-02	1.28E-07	2.79E-02	7.69E-08	3.16E-02	5.10E-08	4.57E-04	7.40E-10	5.63E-02	1.37E-07	4.28E-02	1.17E-07
Visible Light	400	2.64E-01	6.35E-07	1.34E-01	3.05E-07	1.91E-01	4.93E-07	1.32E-01	3.23E-07	2.86E-01	6.71E-07	2.08E-01	5.53E-07
	450	3.47E-01	8.26E-07	4.68E-01	5.97E-07	2.67E-01	5.91E-07	1.09E-01	2.64E-07	3.77E-01	9.13E-07	2.85E-01	6.18E-07
	500	3.82E-01	8.97E-07	2.13E-01	4.38E-07	4.29E-01	9.65E-07	3.74E-01	8.92E-07	4.24E-01	9.94E-07	**5.51E-01**	**8.86E-07**
	550	**4.13E-01**	9.25E-07	**7.22E-01**	**8.16E-07**	4.63E-01	1.08E-06	4.34E-01	9.81E-07	4.43E-01	1.04E-06	5.27E-01	8.70E-07
	600	4.01E-01	**9.29E-07**	7.09E-01	8.12E-07	5.02E-01	1.20E-06	5.09E-01	1.14E-06	4.53E-01	1.06E-06	5.18E-01	8.66E-07
	650	3.77E-01	9.08E-07	5.83E-01	6.50E-07	6.18E-01	1.41E-06	5.66E-01	1.37E-06	4.59E-01	1.07E-06	5.25E-01	8.64E-07
	700	3.59E-01	8.96E-07	4.58E-01	6.68E-07	**6.77E-01**	**1.48E-06**	**5.78E-01**	**1.40E-06**	**4.71E-01**	**1.09E-06**	5.08E-01	8.67E-07
Resonance wavelengths	49	3.80E-06	1.63E-12	2.32E-06	7.02E-13	5.39E-06	6.13E-12	8.13E-07	5.89E-13	4.28E-06	6.96E-12	4.06E-06	2.54E-12
	123	3.47E-03	5.85E-09	1.85E-03	1.61E-09	7.08E-03	6.82E-09	6.21E-05	6.87E-11	6.51E-03	1.00E-08	4.93E-03	5.95E-09
	249	1.98E-02	5.02E-08	1.28E-02	2.27E-08	1.66E-02	3.31E-08	7.43E-04	9.14E-10	2.88E-02	6.20E-08	2.43E-02	4.54E-08
	355	4.40E-02	1.26E-07	2.69E-02	7.39E-08	3.38E-02	5.85E-08	1.19E-03	2.24E-09	5.65E-02	1.36E-07	4.27E-02	1.15E-07

Table 4.2: Summary table of the results obtained for the Silver nanostructures - Probe 2.

		Rectangle thickness = 20 nm		Rectangle thickness = 50 nm		Circle r100		Circle r200		Triangle base = 100 nm		Triangle base = 200 nm	
	λ [nm]	$\|E_{max}\|$ [V/m]	$\int E$	$\|E_{max}\|$ [V/m]	$\int E$	$\|E_{max}\|$ [V/m]	$\int E$	$\|E_{max}\|$ [V/m]	$\int E$	$\|E_{max}\|$ [V/m]	$\int E$	$\|E_{max}\|$ [V/m]	$\int E$
UV	250	3.78E-09	1.04E-14	2.20E-09	4.58E-15	3.09E-09	5.71E-15	1.47E-10	1.83E-16	5.08E-09	1.22E-14	1.47E-10	1.83E-16
	300	6.83E-09	1.98E-14	5.49E-09	1.41E-14	7.13E-09	1.34E-14	1.05E-09	2.32E-15	7.25E-09	2.01E-14	1.05E-09	2.32E-15
	350	5.21E-06	1.48E-11	3.32E-06	8.84E-12	3.37E-06	5.56E-12	4.15E-08	7.62E-14	6.18E-06	1.58E-11	4.15E-08	7.62E-14
Visible Light	400	9.46E-02	2.27E-07	5.32E-02	1.06E-07	9.19E-02	1.66E-07	5.82E-02	1.06E-07	9.82E-02	2.43E-07	5.82E-02	1.06E-07
	450	2.29E-01	5.83E-07	2.40E-01	4.45E-07	2.17E-01	3.96E-07	9.55E-02	1.74E-07	2.68E-01	6.30E-07	9.55E-02	1.74E-07
	500	3.05E-01	7.71E-07	1.89E-01	3.69E-07	4.27E-01	7.87E-07	4.10E-01	7.10E-07	4.14E-01	8.36E-07	4.10E-01	7.10E-07
	550	3.57E-01	8.55E-07	4.93E-01	8.82E-07	4.32E-01	9.73E-07	4.24E-01	8.70E-07	4.87E-01	9.35E-07	4.24E-01	8.70E-07
	600	3.70E-01	8.8E-07	5.14E-01	8.77E-07	5.28E-01	1.07E-06	5.13E-01	9.88E-07	5.19E-01	9.76E-07	5.13E-01	9.88E-07
	650	3.47E-01	8.8E-07	3.81E-01	7.15E-07	6.25E-01	1.31E-06	5.66E-01	1.22E-06	5.71E-01	1.00E-06	5.66E-01	1.22E-06
	700	3.28E-01	8.59E-07	2.64E-01	5.66E-07	6.55E-01	1.43E-06	6.18E-01	1.28E-06	5.84E-01	1.02E-06	6.18E-01	1.28E-06
Resonance wavelengths	49	1.37E-33	8.47E-40	6.35E-34	3.04E-40	2.60E-33	3.27E-39	3.62E-34	2.74E-40	2.30E-33	3.81E-39	3.62E-34	2.74E-40
	123	4.00E-14	8.12E-20	1.92E-14	2.04E-20	8.30E-14	9.22E-20	5.45E-16	6.92E-22	7.57E-14	1.40E-19	5.45E-16	6.92E-22
	249	4.27E-09	1.17E-14	2.48E-09	5.23E-15	3.69E-09	6.59E-15	1.36E-10	1.68E-16	5.64E-09	1.35E-14	1.36E-10	1.68E-16
	355	5.82E-06	1.61E-11	3.54E-06	9.40E-12	4.00E-06	6.96E-12	1.20E-07	2.52E-13	6.84E-06	1.74E-11	1.20E-07	2.52E-13

Table 4.4: Summary table of the results obtained for the Aluminium nanostructures - Probe 1.

		Rectangle thickness = 20 nm		Rectangle thickness = 50 nm		Circle r100		Circle r200		Triangle base = 100 nm		Triangle base = 200 nm	
	λ [nm]	$\|E_{max}\|$ [V/m]	$\int E$	$\|E_{max}\|$ [V/m]	$\int E$	$\|E_{max}\|$ [V/m]	$\int E$	$\|E_{max}\|$ [V/m]	$\int E$	$\|E_{max}\|$ [V/m]	$\int E$	$\|E_{max}\|$ [V/m]	$\int E$
UV	250	2.55E-02	3.34E-08	8.54E-03	5.76E-09	2.95E-02	5.97E-08	2.44E-02	4.71E-08	5.07E-02	6.47E-08	2.11E-02	2.68E-08
	300	2.36E-02	2.45E-08	2.25E-02	1.28E-08	2.71E-02	4.05E-08	1.41E-02	3.42E-08	2.20E-02	3.78E-08	1.62E-02	1.93E-08
	350	5.86E-02	6.83E-08	7.09E-02	4.05E-08	6.37E-02	1.40E-07	4.49E-02	1.07E-07	5.98E-02	1.07E-07	4.86E-02	5.32E-08
Visible Light	400	2.84E-01	3.47E-07	2.87E-01	1.72E-07	3.41E-01	6.97E-07	1.88E-01	4.47E-07	3.02E-01	5.17E-07	2.06E-01	2.43E-07
	450	2.44E-01	3.95E-07	1.35E-01	1.14E-07	3.91E-01	8.28E-07	3.29E-01	7.64E-07	4.65E-01	8.01E-07	5.84E-01	5.31E-07
	500	**3.47E-01**	4.56E-07	**7.95E-01**	7.22E-07	4.85E-01	1.06E-06	3.73E-01	9.17E-07	4.72E-01	8.51E-07	**6.36E-01**	**5.78E-07**
	550	3.38E-01	4.89E-07	5.40E-01	6.44E-07	5.27E-01	1.20E-06	3.99E-01	1.07E-06	4.72E-01	8.68E-07	5.53E-01	5.55E-07
	600	3.31E-01	5.75E-07	4.47E-01	**7.74E-07**	5.43E-01	1.31E-06	**4.49E-01**	**1.20E-06**	5.05E-01	8.84E-07	5.11E-01	5.65E-07
	650	3.02E-01	**5.97E-07**	3.89E-01	7.42E-07	5.62E-01	1.38E-06	4.28E-01	1.16E-06	**5.08E-01**	8.84E-07	4.69E-01	5.63E-07
	700	3.18E-01	5.58E-07	3.80E-01	6.48E-07	**5.78E-01**	**1.43E-06**	3.90E-01	1.03E-06	4.91E-01	**9.14E-07**	4.21E-01	5.24E-07
Resonance wavelengths	119	2.58E-03	5.48E-09	3.48E-04	8.53E-10	8.35E-03	7.46E-09	4.51E-07	3.27E-13	5.35E-03	8.89E-09	4.05E-03	5.42E-09

Table 4.3: Summary table of the results obtained for the Silver nanostructures - Probe 3.

		Rectangle thickness = 20 nm		Rectangle thickness = 50 nm		Circle r100		Circle r200		Triangle base = 100 nm		Triangle base = 200 nm	
	λ [nm]	$\lvert E_{max}\rvert$ [V/m]	$\int E$	$\lvert E_{max}\rvert$ [V/m]	$\int E$	$\lvert E_{max}\rvert$ [V/m]	$\int E$	$\lvert E_{max}\rvert$ [V/m]	$\int E$	$\lvert E_{max}\rvert$ [V/m]	$\int E$	$\lvert E_{max}\rvert$ [V/m]	$\int E$
UV	250	8.46E-61	1.86E-66	3.86E-61	8.11E-67	4.22E-61	8.19E-67	1.44E-62	2.53E-68	9.95E-61	2.11E-66	7.71E-61	1.73E-66
	300	5.37E-58	1.23E-63	3.55E-58	8.39E-64	3.54E-58	7.41E-64	4.92E-59	1.01E-64	5.43E-58	1.25E-63	4.78E-58	1.12E-63
	350	3.37E-36	8.79E-42	1.91E-36	5.03E-42	1.25E-36	2.63E-42	1.35E-38	2.75E-44	3.41E-36	9.33E-42	3.08E-36	7.83E-42
Visible Light	400	4.19E-05	1.06E-10	2.22E-05	4.74E-11	3.60E-05	6.41E-11	1.73E-05	3.79E-11	4.59E-05	1.12E-10	3.61E-05	9.24E-11
	450	1.68E-02	4.49E-08	1.51E-02	3.32E-08	1.98E-02	2.36E-08	8.87E-03	8.28E-09	2.50E-02	4.56E-08	1.86E-02	3.12E-08
	500	1.01E-01	2.68E-07	6.43E-02	1.23E-07	1.17E-01	2.64E-07	1.31E-01	2.20E-07	1.21E-01	3.11E-07	1.37E-01	2.97E-07
	550	2.05E-01	5.01E-07	2.97E-01	4.45E-07	2.22E-01	5.63E-07	2.08E-01	4.92E-07	2.63E-01	5.79E-07	2.94E-01	4.94E-07
	600	2.47E-01	6.24E-07	2.82E-01	6.10E-07	3.08E-01	7.78E-07	3.29E-01	6.80E-07	3.92E-01	7.23E-07	3.30E-01	6.16E-07
	650	3.09E-01	7.36E-07	3.47E-01	5.42E-07	5.24E-01	1.10E-06	4.32E-01	1.03E-06	4.01E-01	9.01E-07	4.03E-01	7.70E-07
	700	3.10E-01	7.63E-07	2.38E-01	4.95E-07	6.82E-01	1.23E-06	6.15E-01	1.11E-06	4.96E-01	9.87E-07	4.24E-01	8.45E-07
Resonance wavelengths	49	0.00E+00	0	0.00E+00	0.00E+00	0.00E+00	0.00E+00	0.00E+00	0.00E+00	0.00E+00	0.00E+00	0.00E+00	0.00E+00
	123	1.25E-98	1E-104	3.89E-99	2.65E-105	1.04E-98	1.08E-104	8.74E-101	6.12E-107	3.15E-98	1.84E-104	1.46E-98	1.22E-104
	249	1.90E-60	4.2E-66	8.75E-61	1.84E-66	9.86E-61	1.91E-66	2.65E-62	4.69E-68	2.20E-60	4.70E-66	1.73E-60	3.91E-66
	355	8.84E-36	2.29E-41	4.85E-36	1.27E-41	3.52E-36	7.44E-42	1.05E-37	2.12E-43	9.32E-36	2.45E-41	8.20E-36	2.01E-41

Table 4.5: Summary table of the results obtained for the Aluminium nanostructures - Probe 2.

		Rectangle thickness = 20 nm		Rectangle thickness = 50 nm		Circle r100		Circle r200		Triangle base = 100 nm		Triangle base = 200 nm	
	λ [nm]	$\lvert E_{max}\rvert$ [V/m]	$\int E$	$\lvert E_{max}\rvert$ [V/m]	$\int E$	$\lvert E_{max}\rvert$ [V/m]	$\int E$	$\lvert E_{max}\rvert$ [V/m]	$\int E$	$\lvert E_{max}\rvert$ [V/m]	$\int E$	$\lvert E_{max}\rvert$ [V/m]	$\int E$
UV	250	3.05E-09	5.17E-15	1.07E-09	9.33E-16	5.32E-09	9.63E-15	4.16E-09	6.34E-15	7.42E-09	1.29E-14	3.76E-09	5.13E-15
	300	7.25E-09	1.02E-14	6.37E-09	5.44E-15	1.05E-08	1.57E-14	4.71E-09	1.10E-14	7.78E-09	1.58E-14	6.66E-09	7.82E-15
	350	4.77E-06	7.83E-12	5.14E-06	5.04E-12	7.10E-06	1.43E-11	5.16E-06	9.92E-12	5.98E-06	1.22E-11	5.42E-06	5.84E-12
Visible Light	400	7.03E-02	1.28E-07	6.06E-02	8.68E-08	1.37E-01	2.36E-07	8.92E-02	1.47E-07	9.72E-02	1.86E-07	7.84E-02	8.26E-08
	450	1.20E-01	2.80E-07	5.47E-02	9.88E-08	2.87E-01	5.53E-07	2.63E-01	5.10E-07	4.19E-01	5.15E-07	3.65E-01	4.02E-07
	500	1.90E-01	3.80E-07	3.37E-01	7.27E-07	4.28E-01	8.88E-07	3.64E-01	7.53E-07	5.11E-01	7.32E-07	4.56E-01	5.88E-07
	550	1.93E-01	3.98E-07	2.21E-01	4.85E-07	5.13E-01	1.07E-06	4.23E-01	9.61E-07	5.45E-01	8.12E-07	4.18E-01	6.31E-07
	600	2.21E-01	4.21E-07	2.48E-01	5.05E-07	5.96E-01	1.19E-06	5.39E-01	1.06E-06	5.52E-01	8.18E-07	4.07E-01	6.16E-07
	650	1.76E-01	3.86E-07	1.36E-01	3.16E-07	6.13E-01	1.31E-06	5.17E-01	1.07E-06	5.46E-01	8.46E-07	3.57E-01	6.02E-07
	700	1.67E-01	3.92E-07	1.62E-01	4.04E-07	6.15E-01	1.38E-06	4.44E-01	9.74E-07	5.37E-01	8.90E-07	3.10E-01	5.67E-07
Resonance wavelengths	119	1.32E-14	3.23E-20	2.08E-15	4.80E-21	3.78E-14	3.81E-20	1.71E-18	1.50E-24	2.73E-14	5.28E-20	2.30E-14	3.16E-20

Table 4.6: Summary table of the results obtained for the Aluminium nanostructures - Probe 3.

		Rectangle thickness = 20 nm		Rectangle thickness = 50 nm		Circle r100		Circle r200		Triangle base = 100 nm		Triangle base = 200 nm	
	λ [nm]	$\lvert E_{max}\rvert$ [V/m]	$\int E$	$\lvert E_{max}\rvert$ [V/m]	$\int E$	$\lvert E_{max}\rvert$ [V/m]	$\int E$	$\lvert E_{max}\rvert$ [V/m]	$\int E$	$\lvert E_{max}\rvert$ [V/m]	$\int E$	$\lvert E_{max}\rvert$ [V/m]	$\int E$
UV	250	3.02E-61	6.51E-67	7.53E-62	8.97E-68	7.09E-61	1.52E-66	3.97E-61	6.62E-67	1.06E-60	2.26E-66	4.43E-61	8.60E-67
	300	3.22E-58	6.21E-64	1.73E-58	2.84E-64	4.70E-58	7.76E-64	1.82E-58	3.29E-64	5.12E-58	9.57E-64	2.86E-58	4.80E-64
	350	2.02E-36	4.58E-42	1.31E-36	2.63E-42	3.18E-36	5.69E-42	1.97E-36	3.25E-42	3.22E-36	7.02E-42	1.82E-36	3.52E-42
Visible Light	400	2.76E-05	5.75E-11	1.93E-05	3.36E-11	5.74E-05	9.13E-11	3.05E-05	5.60E-11	3.98E-05	8.80E-11	2.41E-05	4.38E-11
	450	9.26E-03	2.08E-08	3.05E-03	6.58E-09	2.59E-02	3.49E-08	2.47E-02	2.78E-08	2.04E-02	4.75E-08	1.57E-02	3.73E-08
	500	6.18E-02	1.29E-07	1.38E-01	1.86E-07	1.33E-01	2.94E-07	1.16E-01	2.26E-07	1.32E-01	2.87E-07	1.48E-01	2.24E-07
	550	1.14E-01	2.15E-07	1.37E-01	2.24E-07	2.71E-01	6.33E-07	2.09E-01	5.39E-07	3.07E-01	4.97E-07	2.58E-01	3.57E-07
	600	1.35E-01	2.84E-07	1.43E-01	3.24E-07	3.41E-01	8.81E-07	3.61E-01	7.57E-07	3.78E-01	6.23E-07	2.25E-01	4.87E-07
	650	1.66E-01	3.02E-07	1.36E-01	2.25E-07	5.29E-01	1.11E-06	3.94E-01	9.18E-07	3.88E-01	8.12E-07	3.00E-01	5.36E-07
	700	1.69E-01	3.21E-07	1.43E-01	3.40E-07	6.18E-01	1.22E-06	4.84E-01	8.35E-07	4.22E-01	9.04E-07	2.50E-01	5.59E-07
Resonance wavelengths	119	5.68E-102	4.00E-108	1.42E-102	7.57E-109	4.55E-102	3.80E-108	1.88E-106	1.21E-112	1.52E-101	7.21E-108	6.25E-102	4.40E-108

Table 4.7: Summary table of the results obtained for the Gold nanostructures - Probe 1.

		Rectangle, height 20 nm		Rectangle, height 50 nm		Circle, radius 100 nm		Circle, radius 200 nm		Triangle, base 100 nm		Triangle, base 200 nm	
	λ [nm]	$\lvert E_{max}\rvert$ [V/m]	$\int E$	$\lvert E_{max}\rvert$ [V/m]	$\int E$	$\lvert E_{max}\rvert$ [V/m]	$\int E$	$\lvert E_{max}\rvert$ [V/m]	$\int E$	$\lvert E_{max}\rvert$ [V/m]	$\int E$	$\lvert E_{max}\rvert$ [V/m]	$\int E$
UV	250	2.17E-02	4.33E-08	1.33E-02	1.72E-08	1.70E-02	3.80E-08	4.19E-03	6.47E-09	3.46E-02	6.12E-08	2.04E-02	3.76E-08
	300	1.81E-02	3.55E-08	1.39E-02	1.71E-08	1.94E-02	3.17E-08	3.59E-03	7.76E-09	1.93E-02	4.25E-08	1.57E-02	3.02E-08
	350	5.11E-02	1.15E-07	4.38E-02	6.40E-08	5.04E-02	1.05E-07	9.73E-03	2.29E-08	5.32E-02	1.29E-07	4.64E-02	9.93E-08
Visible Light	400	2.51E-01	5.85E-07	2.25E-01	3.52E-07	1.98E-01	4.86E-07	4.79E-02	1.24E-07	2.58E-01	6.45E-07	2.14E-01	5.08E-07
	450	3.10E-01	7.96E-07	2.65E-01	5.15E-07	1.97E-01	5.00E-07	4.68E-02	1.20E-07	3.51E-01	8.82E-07	2.75E-01	7.12E-07
	500	3.50E-01	9.10E-07	2.32E-01	5.59E-07	2.55E-01	6.89E-07	7.84E-02	2.12E-07	4.03E-01	1.00E-06	4.46E-01	8.77E-07
	550	3.91E-01	9.67E-07	3.39E-01	6.28E-07	3.73E-01	9.32E-07	2.12E-01	5.67E-07	4.26E-01	1.06E-06	4.74E-01	9.15E-07
	600	**4.00E-01**	**9.87E-07**	5.67E-01	**8.02E-07**	4.61E-01	1.12E-06	3.58E-01	8.59E-07	4.42E-01	1.08E-06	4.87E-01	**9.20E-07**
	650	3.99E-01	9.85E-07	**5.94E-01**	7.69E-07	5.21E-01	1.27E-06	4.62E-01	1.10E-06	4.50E-01	1.10E-06	**5.02E-01**	9.18E-07
	700	3.80E-01	9.67E-07	5.12E-01	6.96E-07	**6.17E-01**	**1.42E-06**	**5.46E-01**	**1.29E-06**	**4.58E-01**	**1.11E-06**	4.97E-01	9.17E-07
Resonance wavelengths	64	5.29E-05	2.93E-11	3.40E-05	1.50E-11	7.02E-05	1.03E-10	5.80E-06	7.13E-12	6.68E-05	1.14E-10	6.19E-05	4.05E-11
	238	2.36E-02	4.78E-08	1.58E-02	1.91E-08	2.15E-02	4.84E-08	4.32E-03	6.22E-09	3.40E-02	6.92E-08	2.65E-02	4.35E-08
	536	3.81E-01	9.54E-07	2.74E-01	5.87E-07	3.34E-01	8.65E-07	1.73E-01	4.62E-07	4.22E-01	1.04E-06	4.65E-01	9.06E-07

Table 4.8: Summary table of the results obtained for the Gold nanostructures - Probe 2.

		Rectangle, height 20 nm		Rectangle, height 50 nm		Circle, radius 100 nm		Circle, radius 200 nm		Triangle, base 100 nm		Triangle, base 200 nm	
	λ [nm]	$\lvert E_{max}\rvert$ [V/m]	$\int E$	$\lvert E_{max}\rvert$ [V/m]	$\int E$	$\lvert E_{max}\rvert$ [V/m]	$\int E$	$\lvert E_{max}\rvert$ [V/m]	$\int E$	$\lvert E_{max}\rvert$ [V/m]	$\int E$	$\lvert E_{max}\rvert$ [V/m]	$\int E$
UV	250	3.86E-09	9.20E-15	2.10E-09	3.64E-15	3.58E-09	7.07E-15	7.25E-10	1.04E-15	5.87E-09	1.27E-14	4.09E-09	8.06E-15
	300	6.37E-09	1.50E-14	4.52E-09	7.20E-15	7.65E-09	1.27E-14	1.29E-09	2.82E-15	7.37E-09	1.79E-14	6.40E-09	1.28E-14
	350	5.05E-06	1.33E-11	3.90E-06	7.42E-12	5.38E-06	1.14E-11	9.54E-07	2.37E-12	5.81E-06	1.49E-11	5.22E-06	1.15E-11
Visible Light	400	7.82E-02	2.12E-07	6.21E-02	1.30E-07	7.66E-02	1.71E-07	1.90E-02	4.35E-08	8.94E-02	2.33E-07	7.77E-02	1.84E-07
	450	2.00E-01	5.63E-07	1.48E-01	3.68E-07	1.49E-01	3.46E-07	3.63E-02	8.35E-08	2.59E-01	6.19E-07	2.04E-01	5.01E-07
	500	2.83E-01	7.85E-07	2.04E-01	4.82E-07	2.72E-01	5.75E-07	8.56E-02	1.76E-07	3.77E-01	8.59E-07	4.06E-01	7.39E-07
	550	3.46E-01	8.96E-07	2.83E-01	5.65E-07	3.91E-01	8.37E-07	2.39E-01	5.05E-07	4.44E-01	9.68E-07	4.68E-01	8.28E-07
	600	3.72E-01	9.38E-07	4.57E-01	7.89E-07	5.05E-01	9.93E-07	4.00E-01	7.50E-07	4.84E-01	1.01E-06	4.98E-01	8.52E-07
	650	3.71E-01	9.58E-07	4.36E-01	8.26E-07	5.63E-01	1.17E-06	5.20E-01	9.93E-07	5.37E-01	1.04E-06	5.22E-01	8.69E-07
	700	3.53E-01	9.46E-07	3.38E-01	7.21E-07	5.98E-01	1.35E-06	5.33E-01	1.17E-06	5.60E-01	1.05E-06	5.08E-01	8.81E-07
Resonance wavelengths	64	5.10E-26	3.83E-32	3.51E-26	1.99E-32	9.73E-26	1.34E-31	6.68E-27	7.25E-33	9.03E-26	1.56E-31	7.76E-26	5.50E-32
	238	6.68E-09	1.62E-14	3.87E-09	6.46E-15	7.29E-09	1.43E-14	1.19E-09	1.63E-15	9.91E-09	2.25E-14	8.22E-09	1.49E-14
	536	3.26E-01	8.65E-07	2.34E-01	5.21E-07	3.57E-01	7.60E-07	1.94E-01	4.00E-07	4.22E-01	9.37E-07	4.48E-01	8.03E-07

Table 4.9: Summary table of the results obtained for the Gold nanostructures - Probe 3.

		Rectangle thickness = 20 nm		Rectangle thickness = 50 nm		Circle r100		Circle r200		Triangle base = 100 nm		Triangle base = 200 nm	
	λ [nm]	$\lvert E_{max}\rvert$ [V/m]	$\int E$	$\lvert E_{max}\rvert$ [V/m]	$\int E$	$\lvert E_{max}\rvert$ [V/m]	$\int E$	$\lvert E_{max}\rvert$ [V/m]	$\int E$	$\lvert E_{max}\rvert$ [V/m]	$\int E$	$\lvert E_{max}\rvert$ [V/m]	$\int E$
UV	250	7.50E-61	1.65E-66	3.11E-61	6.50E-67	5.28E-61	1.09E-66	7.23E-62	1.27E-67	1.06E-60	2.24E-66	6.64E-61	1.49E-66
	300	4.17E-58	9.27E-64	1.94E-58	4.26E-64	3.67E-58	6.80E-64	5.40E-59	1.09E-64	5.00E-58	1.11E-63	3.73E-58	7.98E-64
	350	3.00E-36	7.87E-42	1.56E-36	4.19E-42	2.51E-36	5.34E-42	4.88E-37	9.41E-43	3.28E-36	8.84E-42	2.62E-36	6.78E-42
Visible Light	400	3.67E-05	9.87E-11	2.65E-05	6.04E-11	4.05E-05	6.60E-11	8.00E-06	1.69E-11	4.12E-05	1.10E-10	3.23E-05	8.72E-11
	450	1.57E-02	4.32E-08	1.11E-02	2.81E-08	1.62E-02	2.07E-08	4.04E-03	4.27E-09	1.91E-02	4.82E-08	1.46E-02	3.87E-08
	500	9.67E-02	2.73E-07	6.49E-02	1.70E-07	9.56E-02	1.82E-07	3.41E-02	5.05E-08	1.18E-01	3.09E-07	1.18E-01	2.77E-07
	550	2.02E-01	5.28E-07	1.53E-01	3.29E-07	1.99E-01	4.90E-07	1.14E-01	2.86E-07	2.48E-01	5.91E-07	2.65E-01	5.18E-07
	600	2.55E-01	6.69E-07	2.56E-01	5.55E-07	2.90E-01	7.28E-07	2.48E-01	5.20E-07	3.68E-01	7.46E-07	3.29E-01	6.47E-07
	650	3.31E-01	8.03E-07	3.99E-01	6.17E-07	4.41E-01	1.00E-06	3.52E-01	8.57E-07	3.94E-01	9.20E-07	3.97E-01	7.95E-07
	700	3.27E-01	8.44E-07	2.91E-01	6.38E-07	6.45E-01	1.17E-06	5.72E-01	1.01E-06	4.81E-01	1.00E-06	4.25E-01	8.69E-07
Resonance wavelengths	64	7.44E-151	1.24E-157	5.64E-153	7.49E-160	2.87E-150	6.99E-157	3.63E-152	1.17E-158	2.12E-151	5.64E-158	2.85E-151	3.52E-158
	238	4.81E-59	1.05E-64	2.00E-59	4.17E-65	3.76E-59	7.81E-65	4.36E-60	7.70E-66	6.67E-59	1.42E-64	4.43E-59	1.00E-64
	536	1.65E-01	4.34E-07	1.13E-01	2.61E-07	1.39E-01	3.76E-07	7.38E-02	1.92E-07	1.93E-01	4.86E-07	2.14E-01	4.30E-07

Table 4.10: Summary table of the results obtained for the Copper nanostructures - Probe 1.

		Rectangle thickness = 20 nm		Rectangle thickness = 50 nm		Circle r100		Circle r200		Triangle base = 100 nm		Triangle base = 200 nm	
	λ [nm]	$\lvert E_{max}\rvert$ [V/m]	$\int E$	$\lvert E_{max}\rvert$ [V/m]	$\int E$	$\lvert E_{max}\rvert$ [V/m]	$\int E$	$\lvert E_{max}\rvert$ [V/m]	$\int E$	$\lvert E_{max}\rvert$ [V/m]	$\int E$	$\lvert E_{max}\rvert$ [V/m]	$\int E$
UV	250	2.46E-02	4.03E-08	1.41E-02	1.49E-08	2.08E-02	4.13E-08	6.33E-03	1.06E-08	3.65E-02	6.02E-08	2.11E-02	3.41E-08
	300	1.80E-02	3.60E-08	1.34E-02	1.73E-08	1.91E-02	3.09E-08	3.33E-03	7.05E-09	1.93E-02	4.27E-08	1.55E-02	3.07E-08
	350	5.21E-02	1.08E-07	4.28E-02	5.45E-08	5.13E-02	1.07E-07	1.11E-02	2.70E-08	5.47E-02	1.26E-07	4.44E-02	9.10E-08
Visible Light	400	2.58E-01	5.40E-07	2.45E-01	2.98E-07	2.00E-01	5.20E-07	6.40E-02	1.79E-07	2.66E-01	6.16E-07	2.03E-01	4.45E-07
	450	3.07E-01	7.34E-07	2.66E-01	4.26E-07	2.03E-01	5.47E-07	6.69E-02	1.85E-07	3.63E-01	8.60E-07	2.67E-01	6.33E-07
	500	3.60E-01	8.58E-07	2.37E-01	4.76E-07	2.95E-01	7.95E-07	1.39E-01	3.73E-07	4.13E-01	9.78E-07	4.85E-01	8.32E-07
	550	**3.97E-01**	9.16E-07	4.63E-01	6.45E-07	4.04E-01	9.94E-07	2.64E-01	6.81E-07	4.32E-01	1.03E-06	4.93E-01	8.65E-07
	600	3.96E-01	**9.33E-07**	**6.09E-01**	**7.65E-07**	4.76E-01	1.16E-06	3.97E-01	9.42E-07	4.46E-01	1.06E-06	4.98E-01	8.72E-07
	650	3.87E-01	9.24E-07	5.72E-01	6.81E-07	5.48E-01	1.32E-06	4.90E-01	1.18E-06	4.54E-01	1.07E-06	**5.12E-01**	8.71E-07
	700	3.61E-01	8.99E-07	4.62E-01	6.05E-07	**6.49E-01**	**1.45E-06**	**5.45E-01**	**1.33E-06**	**4.66E-01**	**1.09E-06**	5.01E-01	**8.72E-07**
Resonance wavelengths	100	1.15E-03	9.58E-10	1.01E-03	5.07E-10	1.85E-03	2.75E-09	2.24E-04	2.86E-10	2.23E-03	3.08E-09	1.65E-03	1.27E-09
	158	9.41E-03	1.33E-08	7.84E-03	5.07E-09	1.44E-02	2.52E-08	1.83E-03	3.28E-09	2.11E-02	2.77E-08	1.40E-02	1.42E-08
	360	5.43E-02	1.11E-07	4.55E-02	5.64E-08	4.97E-02	1.10E-07	1.26E-02	3.21E-08	5.53E-02	1.31E-07	5.11E-02	9.70E-08
	526	3.82E-01	8.93E-07	3.31E-01	5.49E-07	3.50E-01	8.99E-07	2.00E-01	5.34E-07	4.27E-01	1.01E-06	4.81E-01	8.50E-07

Table 4.11: Summary table of the results obtained for the Copper nanostructures - Probe 2.

		Retangle thickness = 20 nm		Retangle thickness = 50 nm		Circle r100		Circle r200		Triangle base = 100 nm		Triangle base = 200 nm	
	λ [nm]	$\lvert E_{max}\rvert$ [V/m]	$\int E$	$\lvert E_{max}\rvert$ [V/m]	$\int E$	$\lvert E_{max}\rvert$ [V/m]	$\int E$	$\lvert E_{max}\rvert$ [V/m]	$\int E$	$\lvert E_{max}\rvert$ [V/m]	$\int E$	$\lvert E_{max}\rvert$ [V/m]	$\int E$
UV	250	4.02E-09	8.52E-15	2.05E-09	3.15E-15	4.20E-09	7.76E-15	1.10E-09	1.65E-15	5.97E-09	1.26E-14	4.08E-09	7.31E-15
	300	6.41E-09	1.52E-14	4.44E-09	7.27E-15	7.55E-09	1.25E-14	1.20E-09	2.57E-15	7.38E-09	1.80E-14	6.37E-09	1.30E-14
	350	5.11E-06	1.25E-11	3.86E-06	6.26E-12	5.44E-06	1.14E-11	1.08E-06	2.74E-12	5.82E-06	1.45E-11	5.08E-06	1.05E-11
Visible Light	400	7.73E-02	1.96E-07	6.45E-02	1.13E-07	8.82E-02	1.81E-07	2.97E-02	6.15E-08	9.07E-02	2.24E-07	7.56E-02	1.61E-07
	450	1.92E-01	5.20E-07	1.36E-01	3.09E-07	1.74E-01	3.74E-07	5.92E-02	1.26E-07	2.80E-01	5.99E-07	2.04E-01	4.41E-07
	500	2.80E-01	7.40E-07	1.80E-01	4.08E-07	3.23E-01	6.60E-07	1.56E-01	3.05E-07	3.96E-01	8.38E-07	4.33E-01	6.98E-07
	550	3.40E-01	8.49E-07	3.43E-01	6.14E-07	4.13E-01	8.93E-07	2.88E-01	6.07E-07	4.63E-01	9.45E-07	4.77E-01	7.81E-07
	600	3.61E-01	8.85E-07	4.59E-01	7.90E-07	5.19E-01	1.03E-06	4.34E-01	8.23E-07	5.00E-01	9.87E-07	5.03E-01	8.06E-07
	650	3.52E-01	8.97E-07	3.90E-01	7.44E-07	5.81E-01	1.22E-06	5.33E-01	1.07E-06	5.54E-01	1.01E-06	5.23E-01	8.27E-07
	700	3.29E-01	8.73E-07	2.79E-01	6.00E-07	6.34E-01	1.40E-06	5.72E-01	1.20E-06	5.73E-01	1.03E-06	5.03E-01	8.44E-07
Resonance wavelengths	100	3.78E-17	4.22E-23	3.21E-17	2.20E-23	7.90E-17	1.13E-22	7.24E-18	9.18E-24	8.17E-17	1.36E-22	6.44E-17	5.70E-23
	158	2.54E-11	4.72E-17	1.82E-11	1.75E-17	4.18E-11	7.89E-17	5.69E-12	8.73E-18	5.85E-11	9.75E-17	4.17E-11	5.08E-17
	360	9.27E-06	2.22E-11	7.16E-06	1.12E-11	9.18E-06	2.05E-11	2.14E-06	5.70E-12	1.08E-05	2.61E-11	1.02E-05	1.93E-11
	526	3.10E-01	8.00E-07	2.42E-01	4.85E-07	3.69E-01	7.80E-07	2.26E-01	4.54E-07	4.25E-01	8.95E-07	4.47E-01	7.43E-07

Table 4.12: Summary table of the results obtained for the Copper nanostructures - Probe 3.

		Retangle thickness = 20 nm		Retangle thickness = 50 nm		Circle r100		Circle r200		Triangle base = 100 nm		Triangle base = 200 nm	
	λ [nm]	$\lvert E_{max}$ [V/m]	$\int E$	$\lvert E_{max}$ [V/m]	$\int E$	$\lvert E_{max}$ [V/m]	$\int E$	$\lvert E_{max}$ [V/m]	$\int E$	$\lvert E_{max}$ [V/m]	$\int E$	$\lvert E_{max}$ [V/m]	$\int E$
UV	250	6.93E-61	1.53E-66	2.66E-61	5.57E-67	5.97E-61	1.23E-66	1.09E-61	1.91E-67	1.04E-60	2.21E-66	5.97E-61	1.35E-66
	300	4.24E-58	9.41E-64	1.98E-58	4.32E-64	3.64E-58	6.73E-64	4.99E-59	9.97E-65	5.02E-58	1.11E-63	3.80E-58	8.11E-64
	350	2.87E-36	7.40E-42	1.45E-36	3.55E-42	2.47E-36	5.18E-42	5.45E-37	1.03E-42	3.32E-36	8.60E-42	2.52E-36	6.22E-42
Visible Light	400	3.45E-05	9.11E-11	2.41E-05	5.19E-11	4.29E-05	6.90E-11	1.11E-05	2.35E-11	4.12E-05	1.05E-10	2.86E-05	7.72E-11
	450	1.49E-02	3.98E-08	9.81E-03	2.32E-08	1.79E-02	2.22E-08	6.20E-03	6.35E-09	1.97E-02	4.72E-08	1.42E-02	3.41E-08
	500	9.04E-02	2.57E-07	5.72E-02	1.43E-07	1.04E-01	2.13E-07	5.75E-02	9.01E-08	1.21E-01	3.05E-07	1.27E-01	2.71E-07
	550	1.98E-01	4.99E-07	1.98E-01	3.37E-07	2.12E-01	5.23E-07	1.39E-01	3.44E-07	2.56E-01	5.79E-07	2.72E-01	4.93E-07
	600	2.45E-01	6.29E-07	2.58E-01	5.50E-07	2.99E-01	7.55E-07	2.70E-01	5.72E-07	3.77E-01	7.30E-07	3.22E-01	6.18E-07
	650	3.15E-01	7.50E-07	3.60E-01	5.62E-07	4.69E-01	1.04E-06	3.76E-01	9.15E-07	3.95E-01	9.05E-07	3.95E-01	7.70E-07
	700	3.09E-01	7.77E-07	2.45E-01	5.30E-07	6.67E-01	1.20E-06	5.83E-01	1.04E-06	4.86E-01	9.89E-07	4.17E-01	8.45E-07
Resonance wavelengths	100	1.95E-117	3.78E-124	3.07E-118	1.21E-124	5.04E-117	1.22E-123	4.30E-118	1.08E-124	2.48E-117	1.23E-123	3.10E-117	8.48E-124
	158	6.49E-77	1.22E-82	2.70E-77	4.46E-83	1.05E-76	1.85E-82	1.30E-77	1.95E-83	1.40E-76	2.52E-82	8.10E-77	1.39E-82
	360	4.79E-34	1.19E-39	2.47E-34	5.62E-40	4.29E-34	8.49E-40	1.12E-34	1.99E-40	5.77E-34	1.40E-39	4.62E-34	1.03E-39
	526	1.42E-01	3.66E-07	1.08E-01	2.18E-07	1.32E-01	3.51E-07	8.14E-02	1.96E-07	1.73E-01	4.27E-07	1.94E-01	3.70E-07

5

Conclusion

Contents

5.1 Conclusions

At the beginning of this work, the Photovoltaic (PV) technologies were under analysis, providing an overview of their evolution. It clearly shows that these devices are improving in different ways. One way that it can evolve is through the application of nanotechnology, namely nanoantennas. These devices give rise to phenomenons that enhance several photophysical events. The nanoantennas can be used to enhance or improve the absorption of light into a given system, in this case, a semiconductor. The studies conducted in this work have the objective of analyzing and characterizing the behaviour of a solar cell coupled with nanoantennas. Three geometries of aperture nanoantennas were developed and then simulated, for four different metals Silver, Aluminium, Gold and Copper. The structure that showed the highest electric field intensity is not the same structure that delivered the highest field integral. Through the developed simulations, it was achieved electric field enhancement in the semiconductors' plane several times and for different geometries. It was also concluded that light trapping and field enhancement was not only possible in the near region of the antenna, but also the far field (probe 3), for the 100 nm radius nanoantenna. There were several geometries that resulted in field intensity improvement for the four metals, such as the rectangular antenna of 50 nm thickness, both circular antennas and both triangular antennas. As for the field integral, only one geometry displayed improvements in all for metals which was the circular antenna of 100 nm radius. For the rectangular antenna of 20 nm, there were no improvements. As well as for the field integral of the rectangular antenna of 50 nm, the circular antenna of 200 nm radius, and both of the triangular geometries. In addition, the circular antenna of 200 nm radius resulted in improvements in the field integral for Silver, Aluminium and Copper. Even though, the highest electric field intensity is achieved for the rectangular 50 nm structure, the best structure to be used n conjunction with a Si solar cell, from the studied geometries, is the circular antenna with the 100 nm radius. Since, it showcases the most number of overall achieved enhancements, and it enhances for a wider range of wavelengths, not only in terms of the electric field intensity peak, but also for the total electric field. Not excluding, that the other structures might be useful for another applications, such as ones, that require a high electric field concentrated in a point, as a purpose of decreasing the area of the solar cell. It was also possible, in some cases, to influence at which wavelength the maximum electric field occurred, moving it around in the visible spectrum, through the combination of the metal used and geometry applied. Meaning the absorption of the Silicon can be adapted through the use of nanoantennas, depending on which wavelength is relevant to the application in question.

5.2 Future Work

In this work we were able to achieve electric field enhancement and concentration, however this improvement was not characterized in terms of actual energy production. The next step will probably start by achieving such characterization, for example, obtaining the I-V and P-V curves for the already studied geometries. Another possible improvement would be to test other structures that might be able even further the field enhancement and light trapping. Not only by parameter fitting of the already characterized structures in this work, but also completely new structures. In terms of the nanoantenna, not only can the geometry be improved, but also the used materials. The semiconductor can also be changed, such as GaAs, Ge and so on.

Bibliography

[1] R. W. Miles, K. M. Hynes, and I. Forbes, "Photovoltaic solar cells: An overview of state-of-the-art cell development and environmental issues," *Progress in Crystal Growth and Characterization of Materials*, vol. 51, pp. 1–42, 2005.

[2] Best research-cell efficiency chart — photovoltaic research — nrel. [Online]. Available: https://www.nrel.gov/pv/cell-efficiency.html

[3] W. C. Sinke, "Development of photovoltaic technologies for global impact," *Renewable Energy*, vol. 138, pp. 911–914, 8 2019.

[4] S. Chakrabarti, H. N. Saha, IEEE-USA, I. of Electrical, E. E. N. Y. Section, I. of Electrical, E. E. R. 1, I. of Electrical, E. Engineers, and C. University, *2016 IEEE 7th Annual Ubiquitous Computing, Electronics Mobile Communication Conference (UEMCON) : 20-22 October, 2016, Columbia University, New York, USA*.

[5] V. Sethi, M. Pandey, and P. Shukla, "Use of nanotechnology in solar pv cell," *International Journal of Chemical Engineering and Applications*, pp. 77–80, 01 2011.

[6] I. Caetano, J. P. Torres, and R. Lameirinhas, "Simulation of solar cells with integration of optical nanoantennas," *Nanomaterials*, 10 2021.

[7] J. M. T. Pereira, "Fundamentos de electrónica teoria cap.2-díodo de junção p-n," 2010.

[8] J. M. T. P. , "Fundamentos de electrónica teoria cap.7 - dispositivos optoelectrónicos," 2010.

[9] Iv curve — pveducation. [Online]. Available: https://www.pveducation.org/pvcdrom/solar-cell-operation/iv-curve

[10] M. Azzouzi, D. Popescu, and M. Bouchahdane, "Modeling of electrical characteristics of photovoltaic cell considering single-diode model," *Journal of Clean Energy Technologies*, vol. 4, pp. 414–420, 2016. [Online]. Available: http://www.jocet.org/index.php?m=content&c=index&a=show&catid=51&id=634

[11] S. Silvestre, “Strategies for fault detection and diagnosis of pv systems 7 chapter outline,” pp. 10–12, 2018. [Online]. Available: https://doi.org/10.1016/B978-0-12-812959-3.00007-1

[12] F. Rasool, M. Drieberg, N. Badruddin, B. Singh, and M. Singh, “Modeling of pv panels performance based on datasheet values for solar micro energy harvesting.” Institute of Electrical and Electronics Engineers Inc., 1 2017.

[13] “RefractiveIndex.INFO - Refractive index database,” https://refractiveindex.info//, 2022, [Online; accessed 21-May-2022].

[14] A. Alu and N. Engheta, “Theory, modeling and features of optical nanoantennas,” *IEEE Transactions on Antennas and Propagation*, vol. 61, no. 4, pp. 1508–1517, 2013.

[15] R. D. F. R. Gomes, M. J. Martins, A. Baptista, and J. P. N. Torres, “Study of a nano optical antenna for intersatellite communications,” *Optical and Quantum Electronics*, vol. 49, 4 2017.

[16] C. Di Garbo, P. Livreri, and G. Vitale, “Solar nanoantennas energy based characterization,” 05 2016.

[17] A. M. A. Sabaawi, C. C. Tsimenidis, and B. S. Sharif, *Overview of Nanoantennas for Solar Rectennas*. New York, NY: Springer New York, 2013, pp. 231–256.

[18] F. Duarte, J. P. N. Torres, A. Baptista, and R. A. Marques Lameirinhas, “Optical nanoantennas for photovoltaic applications,” *Nanomaterials*, vol. 11, no. 2, 2021. [Online]. Available: https://www.mdpi.com/2079-4991/11/2/422

[19] S. A. M. A., T. C. C., and S. B. S., “Analysis and modeling of infrared solar rectennas,” *IEEE Journal of Selected Topics in Quantum Electronics*, vol. 19, no. 3, pp. 9 000 208–9 000 208, 2013.

[20] A. E. Krasnok, I. S. Maksymov, A. I. Denisyuk, P. A. Belov, A. E. Miroshnichenko, C. R. Simovski, and Y. S. Kivshar, “Optical nanoantennas,” *Physics-Uspekhi*, vol. 56, no. 6, pp. 539–564, jun 2013. [Online]. Available: https://doi.org/10.3367/ufne.0183.201306a.0561

[21] P. Livreri and G. Raimondi, “A novel plasmonic nanoantenna for high efficiency energy harvesting applications,” pp. 193–196, 2020.

[22] A. Chekini, S. Sheikhaei, and M. Neshat, “A novel plasmonic nanoantenna structure for solar energy harvesting,” in *2016 Fourth International Conference on Millimeter-Wave and Terahertz Technologies (MMWaTT)*, 2016, pp. 20–24.

[23] M. Gallo, L. Mescia, O. Losito, M. Bozzetti, and F. Prudenzano, “Design of optical antenna for solar energy collection,” *Energy*, vol. 39, no. 1, pp. 27–32, 2012, sustainable Energy and Environmental Protection 2010. [Online]. Available: https://www.sciencedirect.com/science/article/pii/S0360544211001046

[24] A. E. Krasnok, A. E. Miroshnichenko, P. A. Belov, and Y. S. Kivshar, "All-dielectric optical nanoantennas," *Opt. Express*, vol. 20, no. 18, pp. 20 599–20 604, Aug 2012. [Online]. Available: http://www.osapublishing.org/oe/abstract.cfm?URI=oe-20-18-20599

[25] E. Briones, J. Briones, A. Cuadrado, J. C. Martinez-Anton, S. McMurtry, M. Hehn, F. Montaigne, J. Alda, and F. J. Gonzalez, "Seebeck nanoantennas for solar energy harvesting," *Applied Physics Letters*, vol. 105, no. 9, p. 093108, 2014.

[26] B. Mora-Ventura, R. D. de León, G. García-Torales, J. L. F. Nuñez, J. Alda, and F. J. González, "Responsivity and resonant properties of dipole, bowtie, and spiral Seebeck nanoantennas," *Journal of Photonics for Energy*, vol. 6, no. 2, pp. 1 – 8, 2016. [Online]. Available: https://doi.org/10.1117/1.JPE.6.024501

[27] J. Wenger, "Aperture optical antennas," 2014.

[28] R. A. Marques Lameirinhas, J. P. N. Torres, and A. Baptista, "A sensor based on nanoantennas," *Applied Sciences*, vol. 10, no. 19, 2020. [Online]. Available: https://www.mdpi.com/2076-3417/10/19/6837

[29] B. Kapralos, M. Jenkin, and E. Milios, "Acoustical diffraction modeling utilizing the huygens-fresnel principle," vol. 2005, 11 2005, p. 6 pp.

[30] Diffraction — boundless physics. [Online]. Available: https://courses.lumenlearning.com/boundless-physics/chapter/diffraction/

[31] J. A. Stratton and L. J. Chu, "Diffraction theory of electromagnetic waves," 1939.

[32] R. A. M. Lameirinhas, J. P. N. Torres, A. Baptista, and M. J. M. Martins, "A new method to analyse the role of surface plasmon polaritons on dielectric-metal interfaces," *IEEE Photonics Journal*, vol. 14, no. 4, pp. 1–9, 2022.

[33] N. Sharma, A. Joy, A. K. Mishra, and R. K. Verma, "Fuchs sondheimer–drude lorentz model and drude model in the study of spr based optical sensors: A theoretical study," *Optics Communications*, vol. 357, pp. 120–126, 2015. [Online]. Available: https://www.sciencedirect.com/science/article/pii/S0030401815300857

[34] A. D. Rakić, A. B. Djurišić, J. M. Elazar, and M. L. Majewski, "Optical properties of metallic films for vertical-cavity optoelectronic devices," *Appl. Opt.*, vol. 37, no. 22, pp. 5271–5283, Aug 1998. [Online]. Available: https://opg.optica.org/ao/abstract.cfm?URI=ao-37-22-5271

[35] T. W. Ebbesen, H. J. Lezec, H. F. Ghaemi, T. Thio, and P. A. Wolff, "Extraordinary optical transmission through sub-wavelength hole arrays," *NATURE —*, vol. 391, 1998.

[36] H. Mekawey, Y. Ismail, and M. Swillam, “Extraordinary optical transmission in silicon nanoholes,” *Scientific Reports 2021 11:1*, vol. 11, pp. 1–13, 11 2021. [Online]. Available: https://www.nature.com/articles/s41598-021-01068-x

[37] R. Singh and A. K. Azad, “9 resonant field enhancement of terahertz waves in subwavelength plasmonic structures,” 2013.

Appendix A

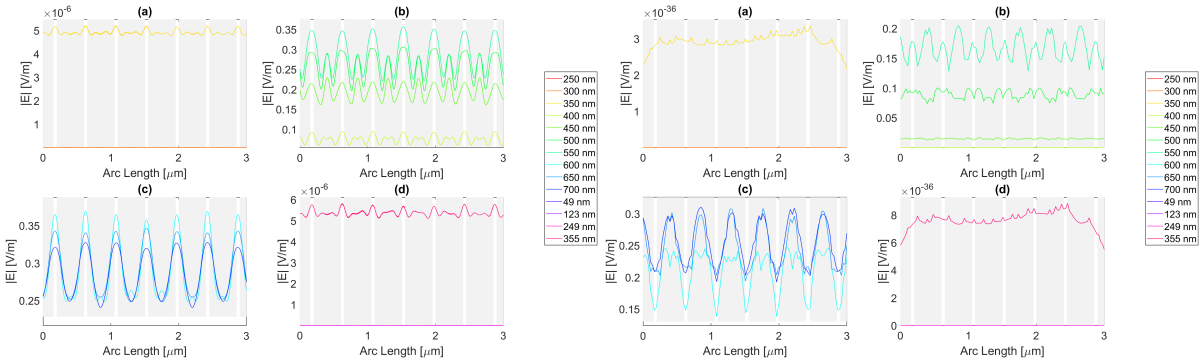

Figure A.1: Electric Field for Silver 20 nm thick rectangular nanostructure - Probe 2 and 3, respectively.

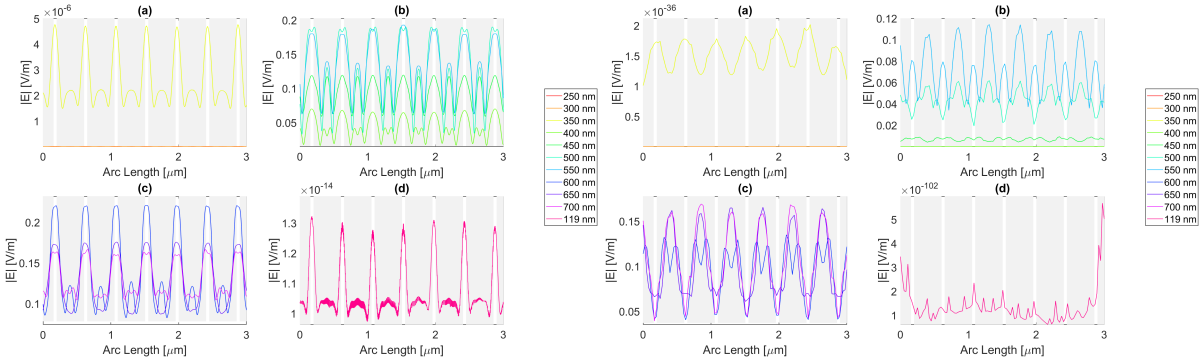

Figure A.2: Electric Field for Aluminium 20 nm thick rectangular nanostructure- Probe 2 and 3, respectively.

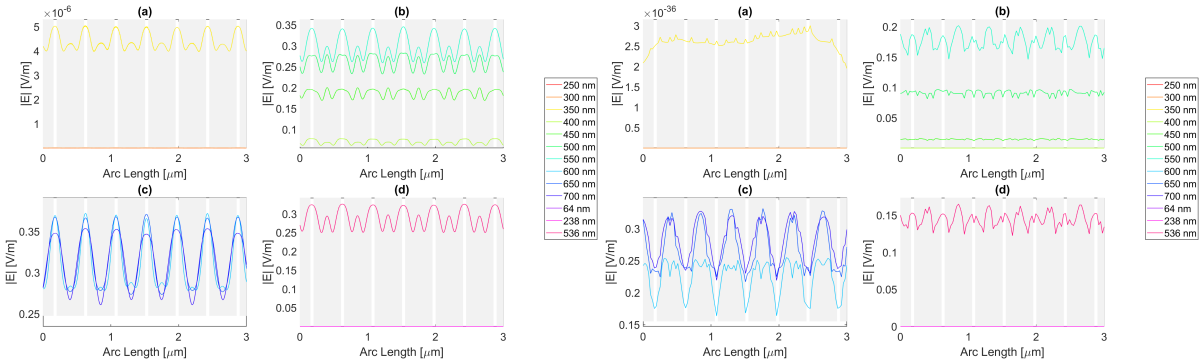

Figure A.3: Electric Field for Gold 20 nm thick rectangular nanostructure - Probe 2 and 3, respectively.

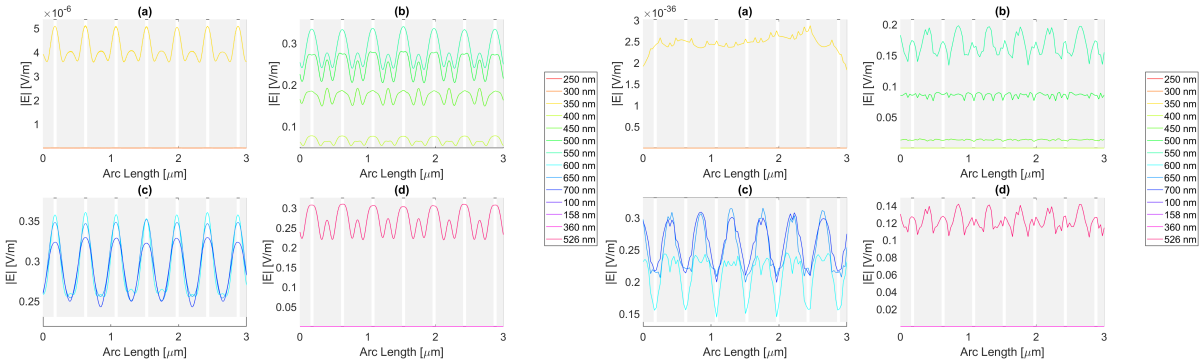

Figure A.4: Electric Field for Copper 20 nm thick rectangular nanostructure - Probe 2 and 3, respectively.

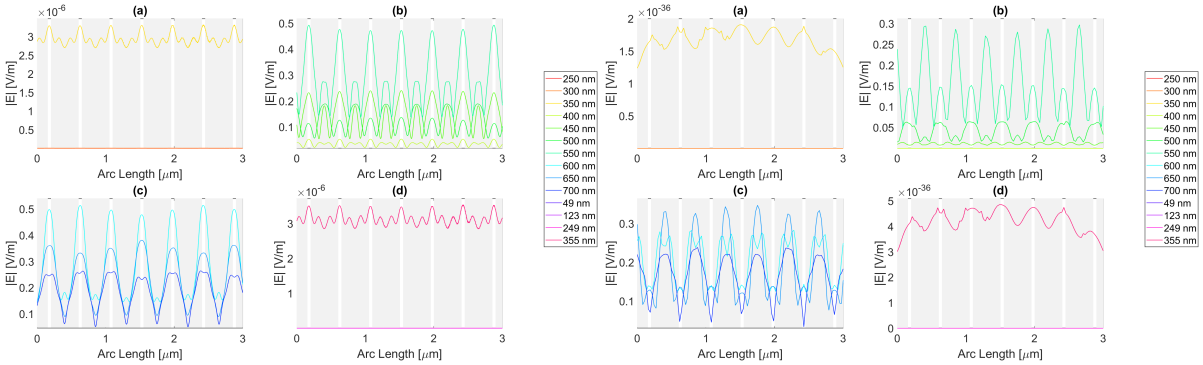

Figure A.5: Electric Field for Silver 50 nm thick rectangular nanostructure - Probe 2 and 3, respectively.

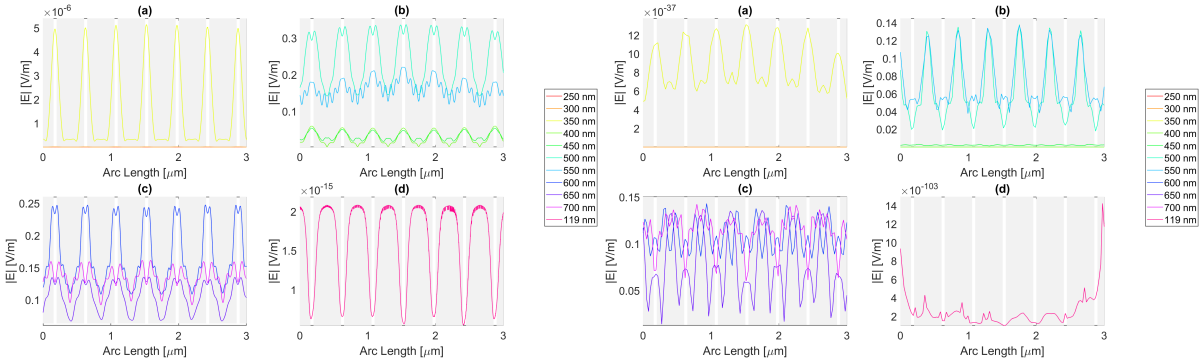

Figure A.6: Electric Field for Aluminium 50 nm thick rectangular nanostructure - Probe 2 and 3, respectively.

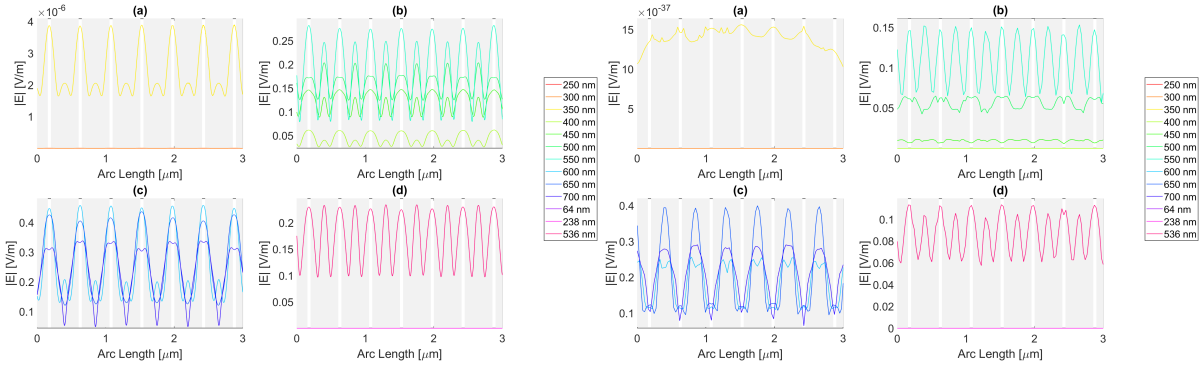

Figure A.7: Electric Field for Gold 50 nm thick rectangular nanostructure - Probe 2 and 3, respectively.

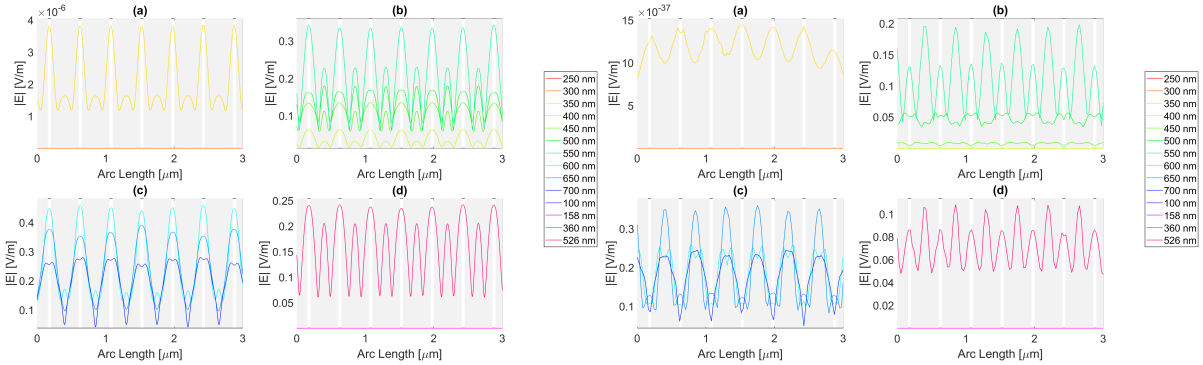

Figure A.8: Electric Field for Copper 50 nm thick rectangular nanostructure - Probe 2 and 3, respectively.

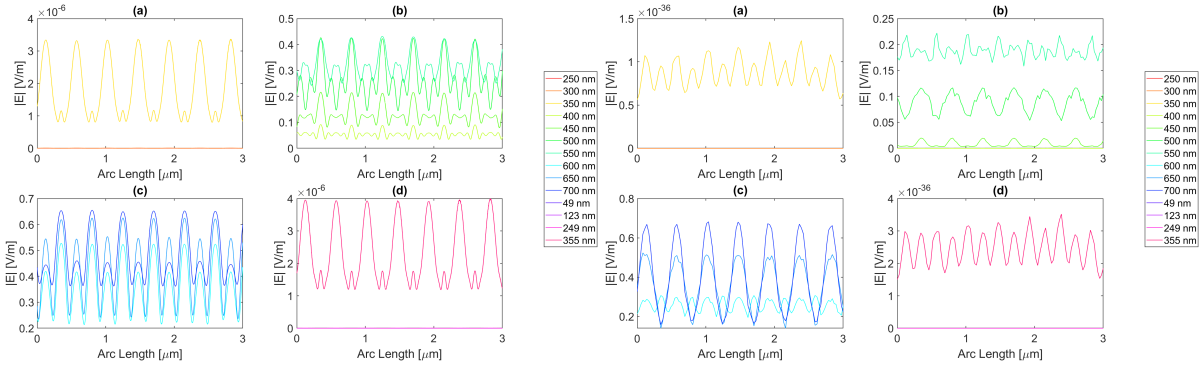

Figure A.9: Electric Field for Silver circular nanostructure with 100 nm radius - Probe 2 and 3, respectively.

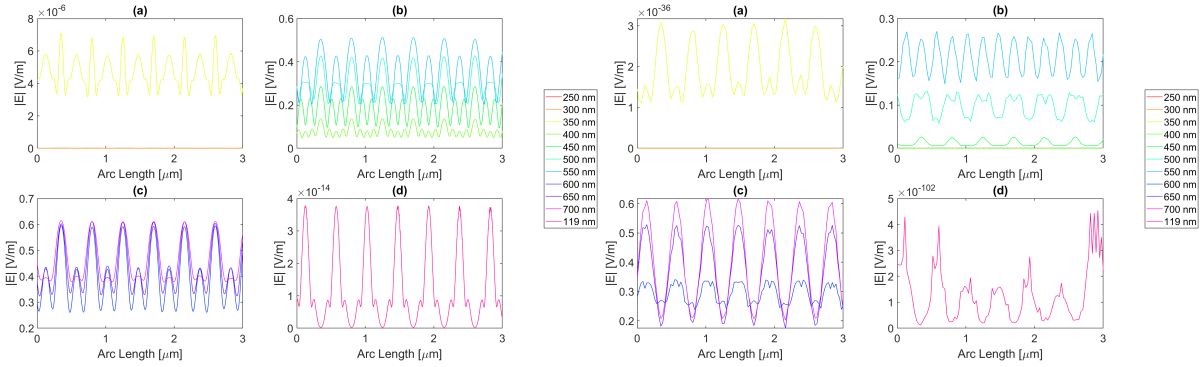

Figure A.10: Electric Field for Aluminium circular nanostructure with 100 nm radius - Probe 2 and 3, respectively.

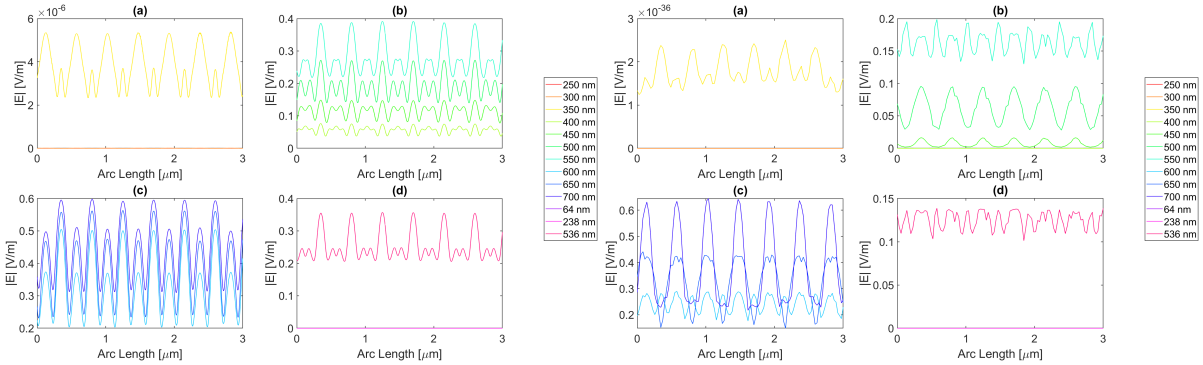

Figure A.11: Electric Field for Gold circular nanostructure with 100 nm radius - Probe 2 and 3, respectively.

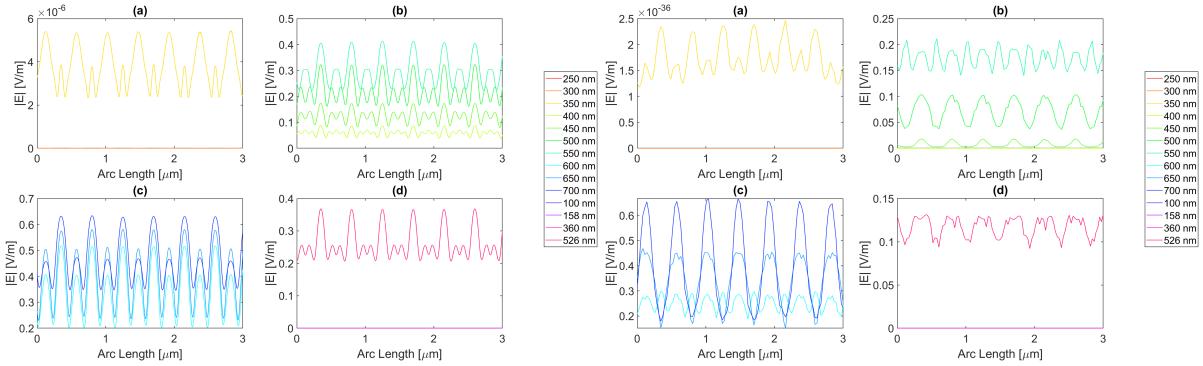

Figure A.12: Electric Field for Copper circular nanostructure with 100 nm radius - Probe 2 and 3, respectively.

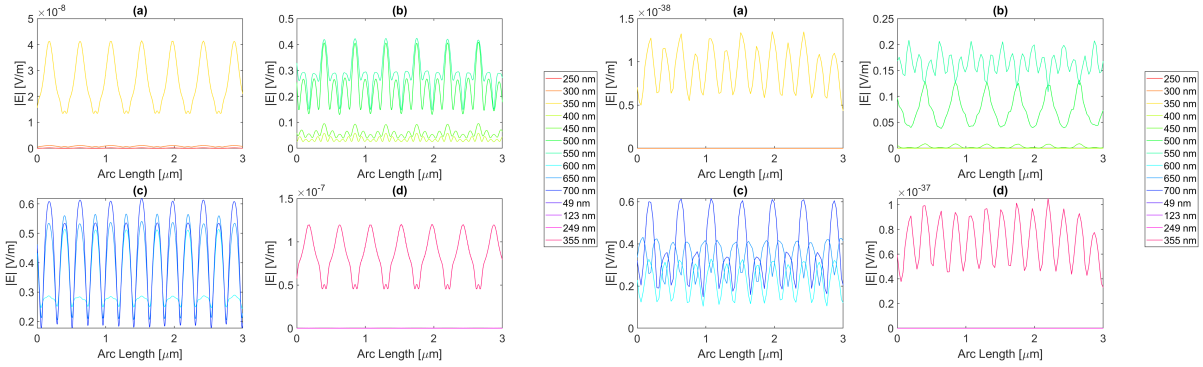

Figure A.13: Electric Field for Silver circular nanostructure with 200 nm radius - Probe 2 and 3, respectively.

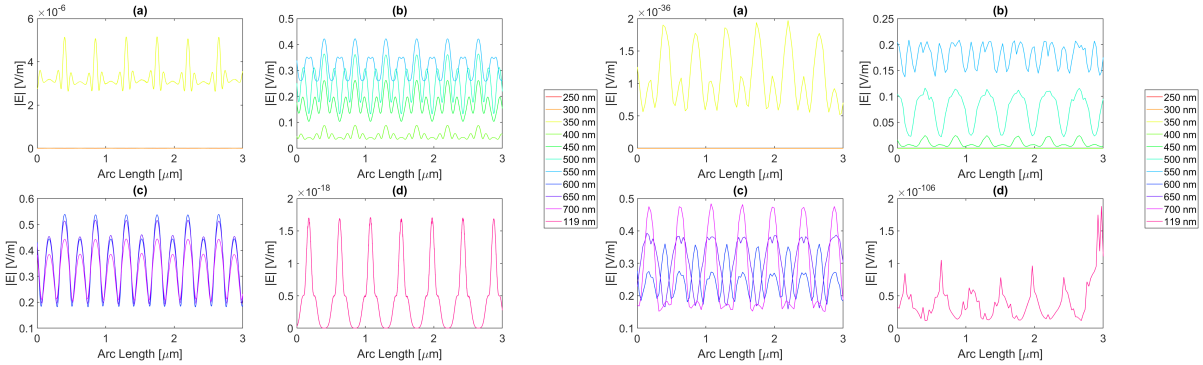

Figure A.14: Electric Field for Aluminium circular nanostructure with 200 nm radius - Probe 2 and 3, respectively.

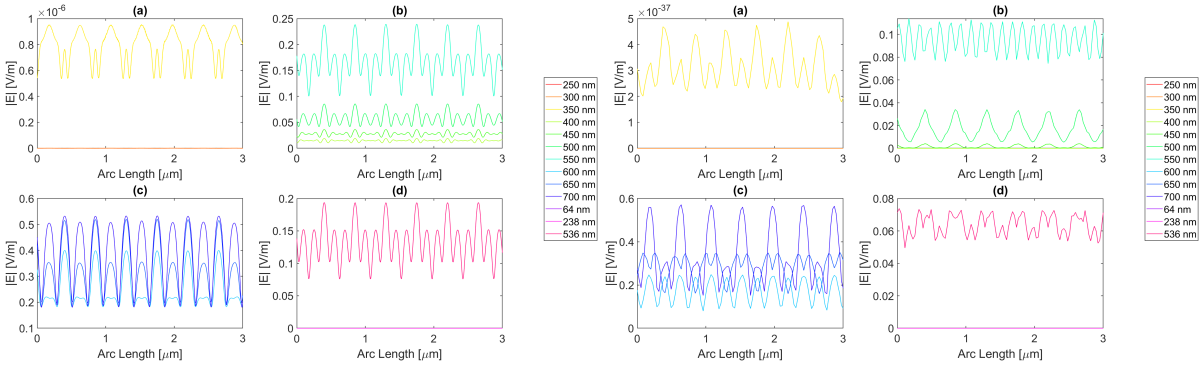

Figure A.15: Electric Field for Gold circular nanostructure with 200 nm radius - Probe 2 and 3, respectively.

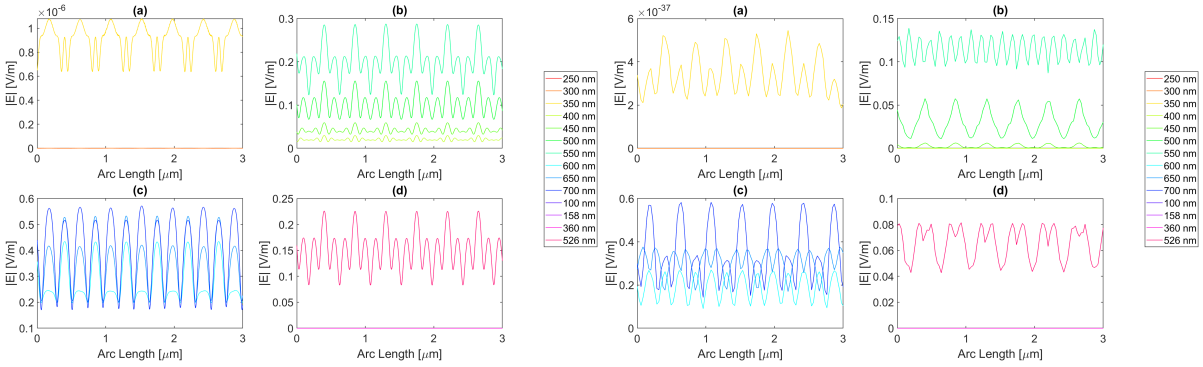

Figure A.16: Electric Field for Copper circular nanostructure with 200 nm radius - Probe 2 and 3, respectively.

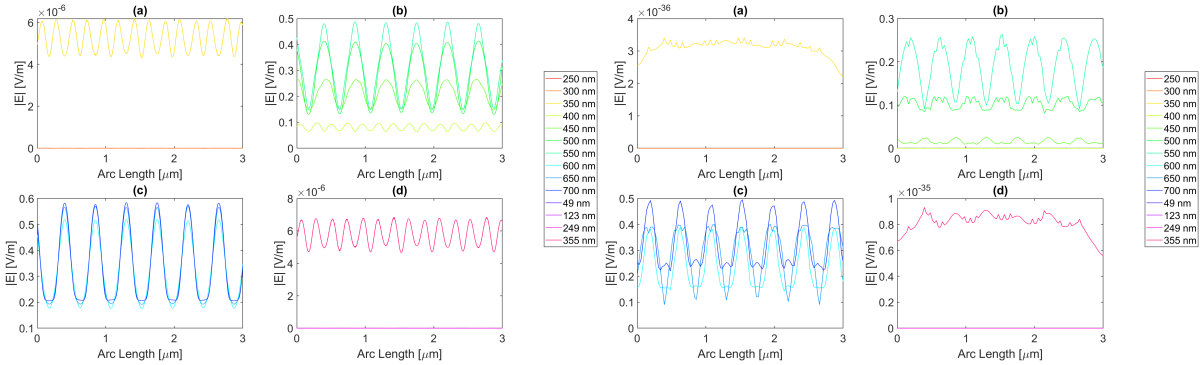

Figure A.17: Electric Field for Silver triangular nanostructure with 100 nm base - Probe 2 and 3, respectively.

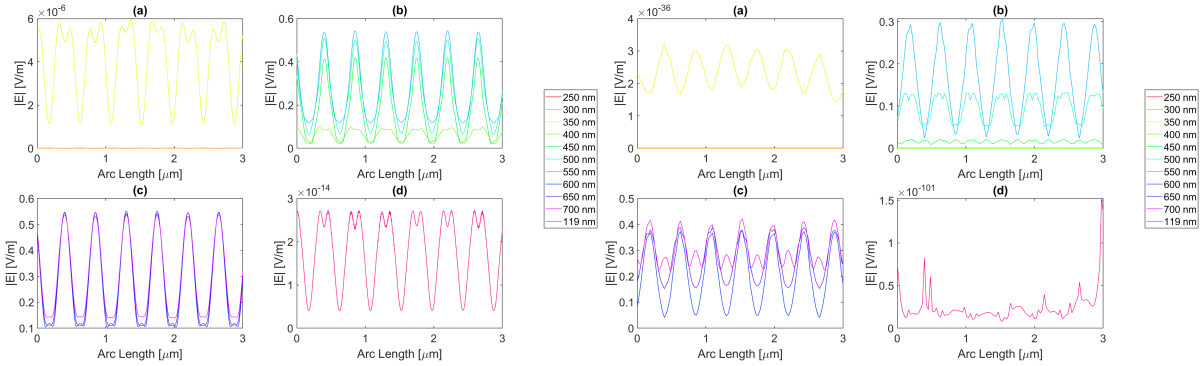

Figure A.18: Electric Field for Aluminium triangular nanostructure with 100 nm base - Probe 2 and 3, respectively.

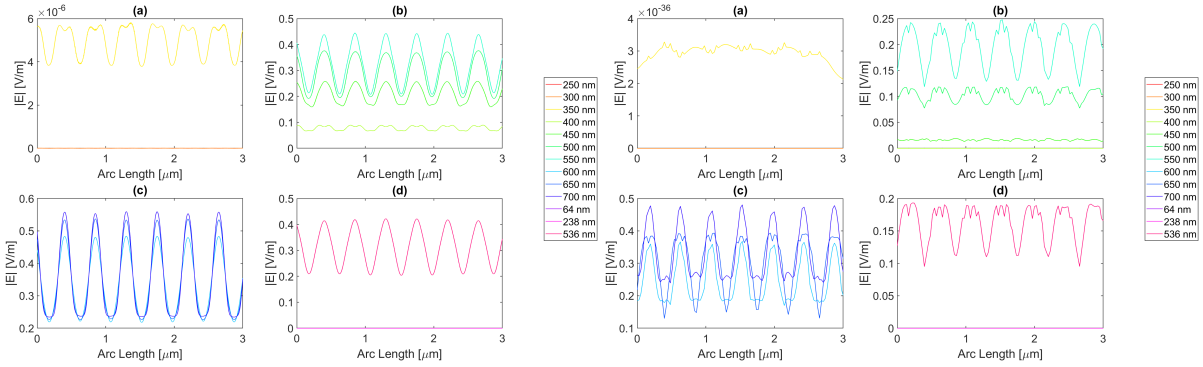

Figure A.19: Electric Field for Gold triangular nanostructure with 100 nm base - Probe 2 and 3, respectively.

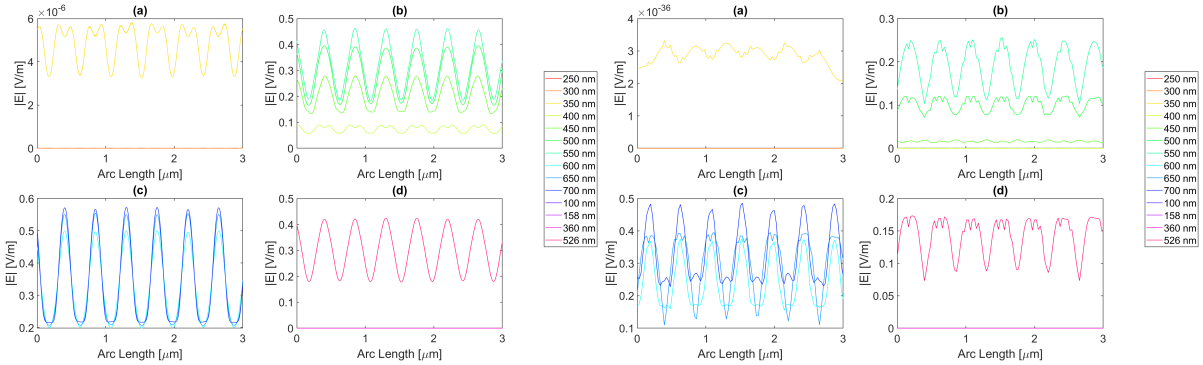

Figure A.20: Electric Field for Copper triangular nanostructure with 100 nm base - Probe 2 and 3, respectively.

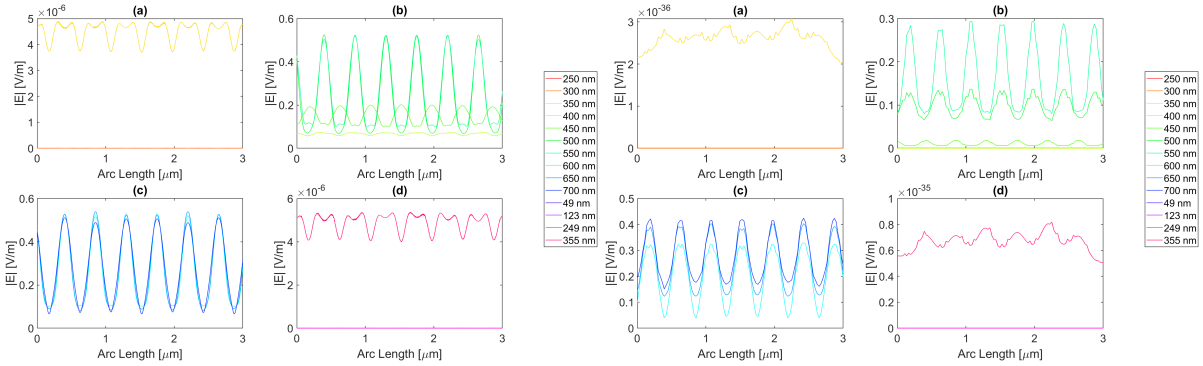

Figure A.21: Electric Field for Silver triangular nanostructure with 200 nm base - Probe 2 and 3, respectively.

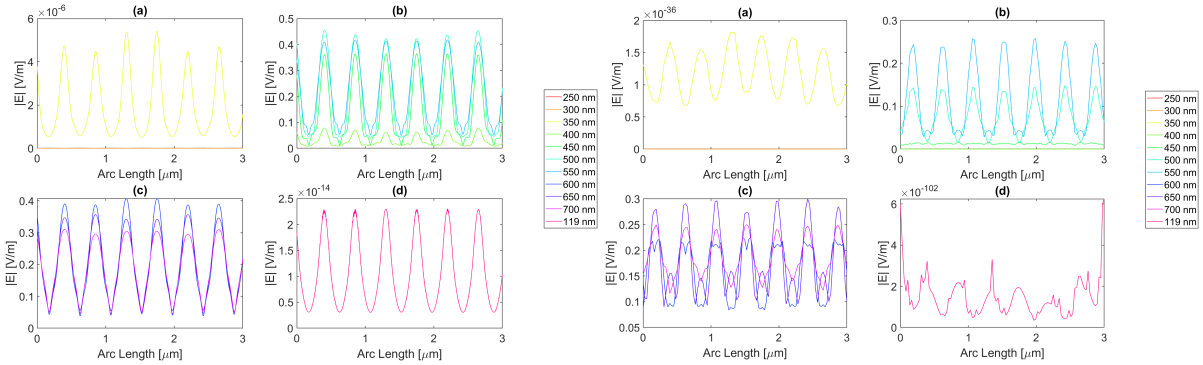

Figure A.22: Electric Field for Aluminium triangular nanostructure with 200 nm base - Probe 2 and 3, respectively.

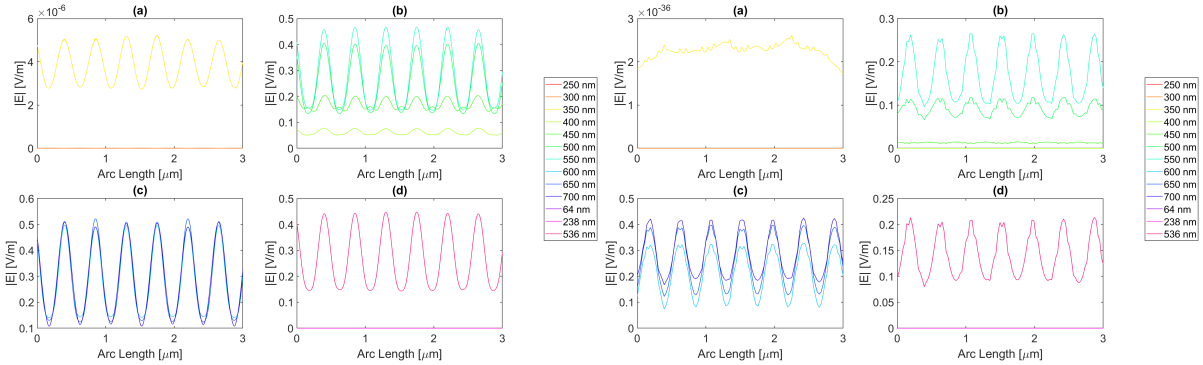

Figure A.23: Electric Field for Gold triangular nanostructure with 200 nm base - Probe 2 and 3, respectively.

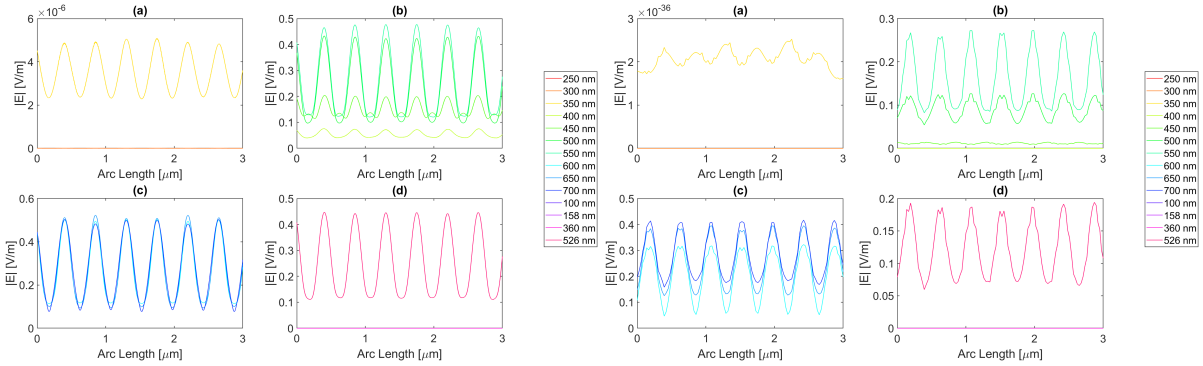

Figure A.24: Electric Field for Copper triangular nanostructure with 200 nm base - Probe 2 and 3, respectively.

B

Appendix B

Table B.1: Results for the stand-alone Silicon cell

	Probe 1		Probe 2		Probe 3	
λ [nm]	$\lvert E_{max}\rvert$ [V/m]	$\int E$	$\lvert E_{max}\rvert$ [V/m]	$\int E$	$\lvert E_{max}\rvert$ [V/m]	$\int E$
250	2.49E-02	7.358E-08	5.32E-09	1.57E-14	1.31E-60	3.04E-66
300	1.74E-02	5.103E-08	7.36E-09	2.16E-14	5.90E-58	1.46E-63
350	5.16E-02	1.518E-07	6.00E-06	1.75E-11	4.02E-36	1.08E-41
400	2.57E-01	7.528E-07	9.28E-02	2.72E-07	4.50E-05	1.19E-10
450	3.36E-01	9.909E-07	2.38E-01	7.01E-07	1.88E-02	5.11E-08
500	3.71E-01	1.101E-06	3.20E-01	9.50E-07	1.14E-01	3.18E-07
550	3.93E-01	1.164E-06	3.66E-01	1.08E-06	2.19E-01	6.21E-07
600	4.06E-01	1.202E-06	3.87E-01	1.14E-06	2.81E-01	8.05E-07
650	4.16E-01	1.230E-06	4.07E-01	1.20E-06	3.48E-01	1.00E-06
700	**4.22E-01**	**1.250E-06**	4.16E-01	1.23E-06	3.79E-01	1.09E-06
64	6.42E-05	1.905E-10	9.01E-26	2.58E-31	2.44E-147	3.94E-154
238	2.87E-02	8.456E-08	9.74E-09	2.88E-14	8.76E-59	2.00E-64
536	3.86E-01	1.147E-06	3.50E-01	1.04E-06	1.82E-01	5.08E-07
100	1.69E-03	5.039E-09	7.59E-17	2.24E-22	1.62E-116	5.05E-123
158	1.44E-02	4.268E-08	5.10E-11	1.51E-16	2.13E-76	4.33E-82
360	5.26E-02	1.550E-07	1.06E-05	3.09E-11	6.73E-34	1.74E-39
526	3.85E-01	1.135E-06	3.45E-01	1.02E-06	1.62E-01	4.53E-07
119	4.30E-03	1.276E-08	2.60E-14	7.69E-20	1.89E-101	1.08E-107
49	4.03E-06	1.170E-11	2.31E-33	6.39E-39	0.00E+00	0.00E+00
123	5.05E-03	1.496E-08	7.05E-14	2.09E-19	4.11E-98	2.97E-104
249	2.54E-02	7.536E-08	5.93E-09	1.76E-14	2.91E-60	6.77E-66
355	5.13E-02	1.506E-07	6.62E-06	1.93E-11	1.07E-35	2.84E-41

Table B.2: Results obtained for the Gold and Aluminium nanostructure.

	λ [nm]	$\lvert E_{max}\rvert$ [V/m]	$\int E$
UV	250	2.20E-02	3.673E-08
	300	2.08E-02	2.980E-08
	350	5.53E-02	9.201E-08
Visible Light	400	2.68E-01	4.683E-07
	450	2.97E-01	6.015E-07
	500	3.80E-01	6.853E-07
	550	**3.93E-01**	7.372E-07
	600	3.89E-01	7.873E-07
	650	3.78E-01	7.754E-07
	700	3.68E-01	**7.990E-07**
Resonance wavelengths	64	6.82E-05	8.215E-11
	238	2.00E-02	3.920E-08
	536	3.87E-01	7.237E-07
	119	3.75E-03	4.692E-09

Table B.3: Results obtained for the Gold and Copper nanostructure.

	λ [nm]	$\lvert E_{max}\rvert$ [V/m]	$\int E$
UV	250	2.30E-02	4.174E-08
	300	1.80E-02	3.574E-08
	350	5.17E-02	1.112E-07
Visible Light	400	2.54E-01	5.627E-07
	450	3.09E-01	7.657E-07
	500	3.55E-01	8.840E-07
	550	3.94E-01	9.423E-07
	600	**3.99E-01**	**9.606E-07**
	650	3.94E-01	9.551E-07
	700	3.72E-01	9.336E-07
Resonance wavelengths	64	5.08E-05	2.736E-11
	238	2.39E-02	4.485E-08
	536	3.84E-01	9.295E-07
	100	1.18E-03	1.075E-09
	158	9.85E-03	1.482E-08
	360	5.37E-02	1.153E-07
	526	3.78E-01	9.191E-07

Table B.4: Results obtained for the Gold and Silver nanostructure.

	λ [nm]	$\lvert E_{max}\rvert$ [V/m]	$\int E$
UV	250	2.00E-02	4.564E-08
	300	1.76E-02	4.091E-08
	350	4.72E-02	1.210E-07
Visible Light	400	2.64E-01	6.112E-07
	450	3.26E-01	8.098E-07
	500	3.62E-01	9.016E-07
	550	4.02E-01	9.467E-07
	600	**4.03E-01**	**9.588E-07**
	650	3.92E-01	9.478E-07
	700	3.72E-01	9.320E-07
Resonance wavelengths	64	6.08E-05	3.333E-11
	238	2.30E-02	5.148E-08
	536	3.93E-01	9.370E-07
	49	3.95E-06	1.576E-12
	123	3.89E-03	5.149E-09
	249	2.06E-02	4.697E-08
	355	4.74E-02	1.202E-07

Table B.5: Results obtained for the Copper and Silver nanostructure.

	λ [nm]	$\lvert E_{max}\rvert$ [V/m]	$\int E$
UV	250	2.05E-02	4.366E-08
	300	1.75E-02	4.117E-08
	350	4.77E-02	1.175E-07
Visible Light	400	2.68E-01	5.884E-07
	450	3.25E-01	7.784E-07
	500	3.70E-01	8.764E-07
	550	**4.05E-01**	9.206E-07
	600	3.99E-01	**9.310E-07**
	650	3.83E-01	9.163E-07
	700	3.60E-01	8.970E-07
Resonance wavelengths	49	3.97E-06	1.535E-12
	123	3.95E-03	4.744E-09
	249	2.11E-02	4.481E-08
	355	4.77E-02	1.163E-07
	100	1.27E-03	1.288E-09
	158	1.08E-02	1.706E-08
	360	5.02E-02	1.202E-07
	526	3.93E-01	9.040E-07

Table B.6: Results obtained for the Aluminium and Silver nanostructure.

	λ [nm]	$\lvert E_{max}\rvert$ [V/m]	$\int E$
UV	250	1.93E-02	3.725E-08
	300	2.00E-02	3.401E-08
	350	5.07E-02	9.648E-08
Visible Light	400	2.85E-01	4.865E-07
	450	3.18E-01	5.974E-07
	500	**4.06E-01**	6.731E-07
	550	3.94E-01	7.090E-07
	600	3.88E-01	**7.628E-07**
	650	3.51E-01	7.302E-07
	700	3.63E-01	7.552E-07
Resonance wavelengths	49	4.30E-06	6.133E-12
	123	3.72E-03	6.122E-09
	249	1.98E-02	3.835E-08
	355	5.05E-02	9.528E-08
	119	3.11E-03	5.168E-09

Table B.7: Results obtained for the Aluminium and Copper nanostructure.

	λ [nm]	$\lvert E_{max}\rvert$ [V/m]	$\int E$
UV	250	2.56E-02	3.572E-08
	300	2.07E-02	2.945E-08
	350	5.57E-02	8.663E-08
Visible Light	400	2.71E-01	4.357E-07
	450	2.87E-01	5.545E-07
	500	3.82E-01	6.478E-07
	550	**3.87E-01**	7.015E-07
	600	3.86E-01	**7.595E-07**
	650	3.57E-01	7.355E-07
	700	3.64E-01	7.566E-07
Resonance wavelengths	119	3.78E-03	4.390E-09
	100	1.27E-03	1.684E-09
	158	1.08E-02	1.424E-08
	360	5.84E-02	8.958E-08
	526	3.82E-01	6.768E-07